Low-dose, high-throughput scanning small-angle X-ray scattering of adherent mouse embryonic fibroblasts

Dissertation
for the award of the degree
"Doctor rerum naturalium" (Dr. rer. nat.)
of the Georg-August-Universität Göttingen

within the doctoral program in Physics
of the Georg-August University School of Science (GAUSS)

submitted by
Chiara Cassini
from Arezzo (Italy)

Göttingen, 2021

Thesis Committee

Prof. Dr. Sarah Köster
Institut für Röntgenphysik
Georg-August-Universität Göttingen

Prof. Dr. Alexander Egner
Laser-Laboratorium Göttingen

Prof. Dr. Tim Salditt
Institut für Röntgenphysik
Georg-August-Universität Göttingen

Members of the Examination Board

Reviewer: Prof. Dr. Sarah Köster
Institut für Röntgenphysik
Georg-August-Universität Göttingen

Second Reviewer: Prof. Dr. Tim Salditt
Institut für Röntgenphysik
Georg-August-Universität Göttingen

Further members of the Examination Board:

Prof. Dr. Alexander Egner
Laser-Laboratorium Göttingen

Prof. Dr. Timo Betz
Drittes Physikalisches Institut - Biophysik
Georg-August-Universität Göttingen

Prof. Dr. Stefan Klumpp
Institut für Dynamik komplexer Systeme
Georg-August-Universität Göttingen

Prof. Dr. Simone Techert
Institut für Röntgenphysik
Georg-August-Universität Göttingen

Date of the oral examination: 26.03.2021

To every kind – be it sisterly, mature, friendly,
adult, romantic, youthful, brotherly, childish,
platonic or familial – of long distance affection.
And to the people willing to make it long lasting.

Contents

Introduction **vii**

1 Theoretical background and state of the art **1**
1.1 Basic interaction of X-rays and matter . . . 1
1.1.1 Scattering of X-rays . . . 2
1.1.2 Small-angle X-ray scattering . . . 4
1.1.3 Scanning SAXS of adherent mammalian cells . . . 6
1.2 Image processing and segmentation tools . . . 7
1.2.1 Intensity thresholding . . . 8
1.2.2 Morphological operations . . . 8

2 Materials and methods **11**
2.1 Cell culture . . . 11
2.1.1 NIH-3T3 fibroblasts . . . 11
2.1.2 Vimentin knockout fibroblasts . . . 11
2.2 Sample preparation . . . 12
2.2.1 Cell fixation . . . 12
2.2.2 Freeze-drying . . . 13
2.2.3 Sample chamber for wet samples . . . 13
2.3 Sample characterization . . . 18
2.3.1 Fluorescence microscopy . . . 18
2.3.2 Scanning SAXS: fast scanning at ID13 . . . 18

3 Results and discussion **21**
3.1 Dark field segmentation . . . 22
3.1.1 Large field-of-view scanning small-angle X-ray scattering of mammalian cells . . . 22
3.1.2 Detection of cell bodies . . . 45
3.1.3 Background definition . . . 48
3.1.4 Detection of nuclei . . . 49
3.2 Comparison of different cell lines . . . 51
3.2.1 Biological system . . . 51
3.2.2 Cell area and scattered intensity . . . 53
3.2.3 Radial intensity profiles . . . 56
3.2.4 Local anisotropy and orientation . . . 60
3.2.5 Discussion . . . 67
3.3 EBS upgrade . . . 69
3.3.1 Comparison of scanning SAXS of freeze-dried cells before and after the EBS upgrade . . . 69
3.3.2 Scanning SAXS on fixed-hydrated cells . . . 72
3.3.3 Discussion and outlook . . . 74

4 Summary, outlook and conclusion **77**

A Measurements of cell thickness **81**

Bibliography **83**

Acknowledgements **93**

List of publications **95**

Introduction

Biological systems are famously complex [1–3]. The interplay of different hierarchical levels at different length scales renders the investigation of multiple scales in the same experiment highly desirable and often necessary. Moreover, the variability that comes with complexity imposes caution in the generalization of experimental results: for example, a property displayed by a single organism is not necessarily possessed by all members of its species. The characterization of a highly variable statistical population calls for high-throughput experimental methods, that is, a large number of members of the population needs to be assessed in order to discern individual properties from properties of the population as a whole. For instance, biological cells are highly variable: differences in e. g. gene expression emerge even among monoclonal, thus genetically identical, cells in the same culture dish [4, 5]. Therefore, the importance of high-throughput single cell assays is on the rise [6–10]. In cell imaging, a way to achieve high-throughput, which in this context means acquiring images of a large number of cells, consists in imaging a large field-of-view. At the same time, high spatial resolution is desirable, so that subcellular details can be captured. Large field-of-view and high spatial resolution have been combined in super-resolution fluorescence microscopy [11, 12] and electron microscopy [13, 14]. Despite the material differences between these two kinds of microscopy, the challenges presented by collecting high spatial resolution, large field-of-view images are similar: they include long acquisition times that need to be reduced and large amounts of data that need to be properly stored and analyzed. Similarly, large field-of-view small-angle X-ray scattering (SAXS) scans are possible [15]. With this particular scanning X-ray technique, the resolution associated to the scan position is not as impressive as with electron microscopy or super-resolution fluorescence microscopy. However, the scattering data contain structural information stemming from nanometer-sized structures, so the requirement of high resolution is satisfied.

In this work, we transfer this high-throughput scanning SAXS approach, that has been demonstrated on cardiac tissue, to the single cell level. In order to speed up the acquisition process, short exposure times are employed, with potentially negative consequences on the signal quality but positive consequences on radiation damage. The theory underlying scanning SAXS is presented in Chapter 1, along with elements of image processing necessary to pre-process the vast amount of data that large field-of-view scanning SAXS provides. Chapter 2 introduces the samples and the experimental techniques employed to study them. Chapter 3 describes and discusses the results of the experiments: in particular, Section 3.1 focuses on the image segmentation strategies adopted to sort the scattering data and on the data analysis possibilities they unlock; Section 3.2 applies such analysis to the comparison of different cell populations; Section 3.3 offers some preliminary results of measurements obtained after the recent "Extremely Brilliant Source" upgrade of the European Synchrotron Radiation Facility. The results are summarized and further commented in Chapter 4, with some suggestions of future developments.

Chapter 1

Theoretical background and state of the art

The theoretical groundwork necessary to analyze and interpret the results of the current work is laid in this chapter. The fundamentals of X-ray-matter interaction, with a focus on coherent scattering, are introduced in Section 1.1, along with the state of the art for scanning small-angle X-ray scattering of adherent mammalian cells. Elements of image segmentation and morphological operations are presented in Section 1.2.

1.1 Basic interaction of X-rays and matter

The X-ray region of the electromagnetic spectrum, located between ultraviolet radiation and gamma-rays, spans energies between about 250 eV and 100 keV, corresponding to wavelengths from several nanometers down to angstroms [16]. This energy range is further divided into "soft" X-rays, for energies lower than about 5 keV, and "hard" X-rays for higher energies. Since the transition energies of core electrons to valence states fall into the soft X-ray range for most light atoms (such as hydrogen, carbon, nitrogen and oxygen), soft X-rays offer insights into chemical composition and bonding states [16–18] and are employed in several microscopy and spectroscopy techniques [18–21]. Hard X-rays have a much higher penetration power through light materials than soft X-rays [16, 22]. Like many other applications of hard X-rays (including, but not limited to, fluorescence microscopy and tomography [23], photoelectron spectroscopy [24, 25] and phase-contrast microscopy and tomography [26]), diffraction and scattering techniques take advantage of their high penetration depth. Because of their high energies, the interaction of hard X-rays with matter is unlikely, thus it is reasonable to assume that a single photon travelling through a sample interacts at most once, disregarding multiple interactions (Born approximation). Macroscopically, the interaction between an incident X-ray beam of intensity I_0 and a material of thickness x and mass density ρ_m can be quantified by measuring the transmitted intensity I, *i. e.* the intensity that passes unperturbed through the sample. It is found that the transmitted intensity decreases exponentially as the thickness x increases:

$$\frac{I}{I_0} = e^{-\mu x}, \tag{1.1}$$

where μ is called the linear absorption coefficient. The linear absorption coefficient depends on the composition of the material and on the energy of the incident radiation. Since the linear absorption coefficient is directly proportional to the mass density of the material, it is customary to express equation (1.1) in the form

$$\frac{I}{I_0} = \exp\left[-(\mu/\rho_m)(\rho_m x)\right] \tag{1.2}$$

and to use the quantity μ/ρ_m instead, called the mass absorption coefficient.

Microscopically, the decrease of the transmitted intensity can be caused by four kinds of interactions: coherent scattering, incoherent scattering, photoelectric absorption and pair production. Scattering is the process in which an electron is accelerated by an incoming electromagnetic radiation, thus becoming a secondary source of electromagnetic radiation. In particular, coherent scattering is elastic and is treated in more detail below, while incoherent scattering is inelastic. Photoelectric absorption occurs when a strongly-bound electron absorbs the energy of an incoming photon. Pair production is a relativistic process that results in the formation of an electron-positron pair. It is only possible when the energy of the incoming electromagnetic radiation is at least equal to the rest mass energy of the pair, that is, twice the rest mass of an electron, namely 1022 keV.

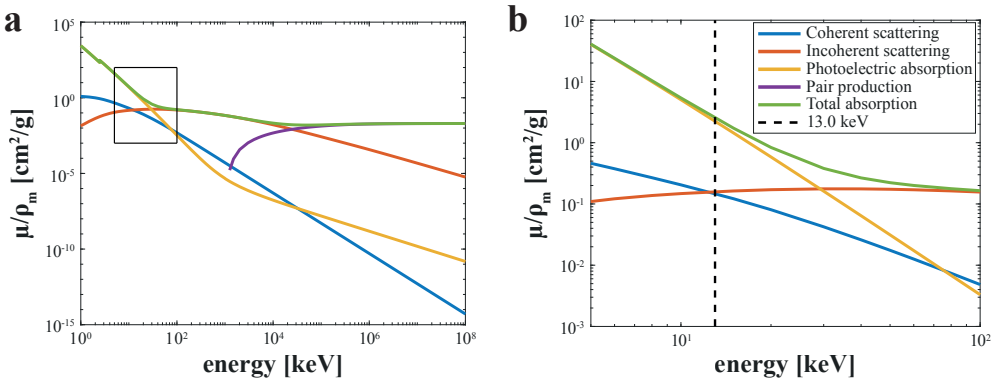

Figure 1.1: Mass absorption coefficients for an average protein of empirical formula $H_{50}C_{30}N_9O_{10}S$, representing the average cellular composition [27], in the hard X-ray and gamma-ray regions of the electromagnetic spectrum. a) Mass absorption coefficient for energies between 1 keV and 100 GeV. The black box indicates the hard X-ray region shown in panel b. b) Mass absorption coefficient for energies between 5 keV and 100 keV (hard X-rays). The black dashed line corresponds to an energy of 13.0 keV. All values were obtained using the XCOM: Photon Cross Sections Database [28] of the National Institute for Standards and Technology.

The mass absorption coefficients for the four kinds of interactions listed above can be calculated for substances of known composition [29], and the total mass absorption coefficient used in equation (1.2) is their sum. As shown in Figure 1.1, photoelectric absorption dominates at lower energies and in most of the hard X-ray range. For high-energy X-rays and low-energy gamma-rays, incoherent scattering becomes dominant, while pair production is the most important contribution to the mass absorption coefficient for extremely high energies. The black dashed line in Figure 1.1b marks an energy of 13.0 keV, that is the value used in all the experiments presented in this work. At this energy value, incoherent scattering occurs slightly more frequently than coherent scattering. However, incoherent scattering is negligible for small scattering angles [22, 30, 31] and it appears in typical small-angle X-ray scattering data as a background contribution only emerging at large angles [32, 33].

1.1.1 Scattering of X-rays

The scattering of X-rays by one or more electrons can be satisfactorily described with a semi-classical model, in which X-rays are treated as waves and bound electrons are treated as harmonic oscillators characterized by different resonance frequencies. Such a description can be found, for instance, in Reference [16]. The simplest case of X-ray scattering is the scattering

by a free electron. As a consequence of Maxwell's equations and Newton's second law, a free electron subjected to an incident electromagnetic wave of electric field $\vec{E}_i$ becomes a source of secondary spherical electromagnetic waves. At a distance $\vec{r}$ from the electron and at time t from the generation of the secondary wave, the magnitude of the secondary electric field $\vec{E}_{\text{Thomson}}(\vec{r},t)$ is given by:

$$E_{\text{Thomson}}(\vec{r},t) = -\frac{r_e E_{i,T}}{r} e^{-i\omega(t-r/c)}, \tag{1.3}$$

where $E_{i,T}$ is the transverse component of the incident electric field (that is, perpendicular to the direction of propagation of the incident radiation), ω is the angular frequency of the wave, c is the speed of light in vacuum and r_e is the classical electron radius,

$$r_e = \frac{e^2}{4\pi\varepsilon_0 m_e c^2}, \tag{1.4}$$

with e the charge of the electron, ε_0 the dielectric constant of vacuum and m_e the mass of the electron. This kind of scattering is called Thomson scattering. The scattering from one or more bound electrons can be compared to Thomson scattering and the magnitude of the scattered electric field can be expressed as a multiple of $E_{\text{Thomson}}(\vec{r},t)$, thus using the results obtained for Thomson scattering as a sort of unit of measurement. In practice, an expression for the intensity of the scattered radiation is more useful than the scattered electric field, as the intensity is the physical quantity measured in scattering experiments. The intensity of an electromagnetic wave is retrievable as the magnitude I of the Poynting vector $\vec{S}(\vec{r},t) = \vec{E}(\vec{r},t) \times \vec{H}(\vec{r},t)$, averaged in time ($\vec{H}$ is the magnetic field of the wave). As a consequence of this definition and of Maxwell's equations, it can be shown that

$$I = \frac{1}{2}\sqrt{\frac{\varepsilon_0}{\mu_0}}|\vec{E}|^2, \tag{1.5}$$

where μ_0 is the magnetic permeability of vacuum. Therefore, for Thomson scattering the scattered intensity I_{Thomson} at position $\vec{r}$ from the free electron is given by

$$I_{\text{Thomson}} = \frac{1}{2}\sqrt{\frac{\varepsilon_0}{\mu_0}} E_{i,T}^2 \frac{r_e^2}{r^2} = I_0 \frac{r_e^2}{r^2} \frac{1+\cos^2(2\theta)}{2}, \tag{1.6}$$

with I_0 the incident intensity and 2θ the angle between the direction of propagation of the incident wave and $\vec{r}$. The term $\dfrac{1+\cos^2(2\theta)}{2}$ is called the polarization factor and it is due to the fact that only the transverse component of the incident electric field contributes to the scattered wave. Importantly, for small scattering angles θ, the polarization factor is practically equal to 1.

When the incident electromagnetic wave is scattered by a multi-electron atom, the electrons are no longer free, and the s-th electron behaves in our semi-classical model as a harmonic oscillator of characteristic angular frequency ω_s. Additionally, each electron is a secondary source of electromagnetic waves, thus the waves emitted by different electrons can interfere with each other. Using once more Maxwell's equations and Newton's second equation of motion, it is possible to obtain the magnitude of the scattered electric field $\vec{E}(\vec{r},t)$ far from the scattering atom (*i. e.* r is much larger than the dimensions of the atom):

$$E(\vec{r},t) = E_{\text{Thomson}}(\vec{r},t) f(\vec{q},\omega), \tag{1.7}$$

where $\vec{q}$ is the scattering vector, defined as the difference between the incident wave vector and the scattered wave vector. $f(\vec{q},\omega)$ is the atomic scattering factor. For an atom with Z electrons,

$$f(\vec{q},\omega) = \sum_{s=1}^{Z} \frac{\omega^2 e^{-i\vec{q}\cdot\vec{x}_s}}{\omega^2 - \omega_s^2 + i\zeta\omega}, \tag{1.8}$$

with $\vec{x}_s$ describing the position of the s-th electron within the atom and ζ accounting for energy dissipation.

1.1.2 Small-angle X-ray scattering

Equations (1.7, 1.8) describe a very generic case of scattering, in which the effects of binding energies are taken into account (presence of the characteristic angular frequencies ω_s) and energy loss is possible (presence of the factor ζ). Small-angle X-ray scattering (SAXS), in contrast, deals with a very special case of scattering: several assumptions are made that simplify equation (1.8) greatly. This process is coherent, elastic and each single scattering electron is considered free. Indeed, at small angles (up to 10°) between the incident wave vector and the scattered wave vector, incoherent scattering is negligible [22, 30, 31]. As the energy of X-rays, and hard X-rays in particular, is large compared to the binding energy of electrons, it is possible to treat all electrons as they were free. With these considerations, each electron simply deviates the incident X-rays, without modifying the energy. Therefore, the incident wave vector and the scattered wave vector have the same magnitude $2\pi/\lambda$, thus the scattering vector $\vec{q}$ has magnitude

$$q = \frac{4\pi}{\lambda}\sin(\theta). \tag{1.9}$$

In this case, the atomic scattering factor of equation (1.8) simplifies to

$$f(\vec{q},\omega) = \sum_{s=1}^{Z} e^{-i\vec{q}\cdot\vec{x}_s} : \tag{1.10}$$

all of the differences between this kind of scattering and the scattering from one electron (Thomson) are due to interference of waves originating from electrons located at different positions in the atom. $f(\vec{q},\omega)$ can be modified to describe a generic scatterer, for example a molecule or a macromolecule, characterized by a continuous electron density $\rho(\vec{x})$: the continuous scattering factor is then the Fourier transform of the electron density. Thus, the magnitude of the scattered electric field is

$$E(\vec{r},t) = E_{\text{Thomson}}(\vec{r},t)\int d\vec{x}e^{-i\vec{q}\cdot\vec{x}}. \tag{1.11}$$

Equation (1.11) is the starting point for the theoretical treatment of SAXS thoroughly presented in References [30, 31].

SAXS is commonly applied to the study of proteins or other polymers in solution, as an alternative to crystallography when crystallization of the sample is impractical or impossible. In this case, the sample solution ideally contains many identical copies of the studied polymer; the scattered intensity measured by the detector is a result of all polymers present in the irradiated volume, thus it comes from an orientational average. The effects of the orientational average need to be taken into account in order to retrieve the structure of the sample, that is, its electron density $\rho(\vec{r})$, from the scattered intensity. In the current work, however, SAXS is employed in a different way: the SAXS signal is recorded by scanning the sample (an adherent murine cell) through an X-ray beam much smaller than the sample itself. Thus, the beam no longer encounters many identical copies of the same scatterer in different orientations, but rather a heterogeneous set of scatterers. The electron density within the irradiated volume can still be described by a function $\rho(\vec{x})$ of the position $\vec{x}$ within the irradiated volume V, so that the SAXS intensity originating from the irradiated volume is given by the very generic expression

$$I(\vec{q}) = I_{\text{Thomson}}\left[\int_V \rho(\vec{x})e^{-i\vec{q}\cdot\vec{x}}d^3x\right]^2. \tag{1.12}$$

Not much can be said in general about $I(\vec{q})$ unless some kind of model for $\rho(\vec{x})$ is known. Nevertheless, a few very useful observations can be made about the behaviour of the SAXS intensity at large q values. In the treatment of Debye and Bueche [30, 34], $\rho(\vec{x}) = \rho_0 + \eta(\vec{x})$, where ρ_0 is the average density and $\eta(\vec{x})$ accounts for density fluctuations from the average value (and therefore, by definition, $\int \eta(\vec{x}) d^3x = 0$).

By substituting this expression for $\rho(\vec{x})$ into equation (1.12) and after a few approximations, the scattered intensity can be rewritten as:

$$I(\vec{q}) \approx I_{\text{Thomson}} \int_V d^3r e^{i\vec{q}\cdot\vec{r}} \int_V d^3x \eta(\vec{x})\eta(\vec{x}+\vec{r}). \tag{1.13}$$

Note that the second integral only depends on $\vec{r}$, and it is proportional to the mean value of the square of the density fluctuations $\bar{\eta^2}$ when $r = 0$, so we can define

$$\int_V d^3x \eta(\vec{x})\eta(\vec{x}+\vec{r}) \equiv \bar{\eta^2} V \gamma(\vec{r}). \tag{1.14}$$

By this definition, γ is a function that describes the density fluctuation correlation. Consequently,

$$I(\vec{q}) = I_{\text{Thomson}} \bar{\eta^2} V \int_V \gamma(\vec{r}) e^{i\vec{q}\cdot\vec{r}} d^3r. \tag{1.15}$$

It is reasonable to assume that there is no long-range density fluctuation correlation, that is, $\gamma(\vec{r}) \xrightarrow[r\to+\infty]{} 0$. Thus, we can extend the integral to all space instead of just the irradiated volume V. Additionally, for an isotropic system, $\gamma(\vec{r})$ depends only on r; therefore,

$$I(\vec{q}) = I_{\text{Thomson}} \bar{\eta^2} V \int_0^{+\infty} \gamma(r) \frac{\sin qr}{qr} 4\pi r^2 dr. \tag{1.16}$$

A particular case, treated by Porod [35], is the case of a random distribution of matter of constant density. This means that, inside the irradiated volume V,

$$\rho(\vec{x}) = \begin{cases} \rho, & \vec{x} \text{ occupied}, \\ 0, & \vec{x} \text{ empty}, \end{cases} \tag{1.17}$$

where ρ is no longer a function, but a constant (the value of the density). Let c be the fraction of the volume occupied by matter: then, the average density of the sample is $\rho_0 = \rho c$, so

$$\eta(\vec{x}) = \begin{cases} \rho(1-c), & \vec{x} \text{ occupied}, \\ -\rho c, & \vec{x} \text{ empty}, \end{cases} \tag{1.18}$$

and $\bar{\eta^2} = \rho^2 c(1-c)$. With these hypotheses and definitions,

$$I(\vec{q}) = I_{\text{Thomson}} V \rho^2 c(1-c) \int_0^{+\infty} \gamma(r) \frac{\sin(qr)}{qr} 4\pi r^2 dr. \tag{1.19}$$

The asymptotic properties of $\gamma(r)$ for large values of q, or equivalently, large values of r, determine the asymptotic behavior of $I(\vec{q})$. In particular, it can be shown [30, 35, 36] that

$$\left.\frac{d\gamma}{dr}\right|_{r=0} = -\frac{1}{4c(1-c)} \frac{S}{V}, \tag{1.20}$$

with S total surface area of the matter in the irradiated volume V. From this property we can conclude that, for large angles,

$$I_{\text{Porod}}(\vec{q}) \approx I_{\text{Thomson}} \frac{2\pi\rho^2 S}{q^4}, \tag{1.21}$$

which is known as Porod's law. This kind of asymptotic behavior, where the scattered intensity decreases with q^{-4}, with a proportionality constant dependent on the squared electron density ρ^2 and on the surface area of the scattering matter S is also valid in the case of numerous, distinct and different scatterers, with the k-th scatterer characterized by a constant electron density ρ_k, a surface area S_k and present in the irradiated volume with probability p_k. In this case, Porod's law holds in the form [30]:

$$I_{\text{Porod}}(\vec{q}) \approx I_{\text{Thomson}} \bar{N} \left(\sum_k p_k \rho_k^2 S_k \right) \frac{2\pi}{q^4}, \tag{1.22}$$

where $\bar{N}$ is the average number of scatterers. In all of the above, the scatterers have implicitly been assumed to be in vacuum: more rigorously, the electron density ρ should be substituted by the electron density contrast $\Delta\rho$, that is, the difference between the electron density of the scatterers and that of the medium in which the scatterers are immersed, such as air or water. In a typical SAXS experiment, the intensity $I(\vec{q})$ scattered at small angles is collected by an area detector, thus one individual SAXS measurement consists in a two-dimensional intensity image, the so-called scattering pattern. As equations (1.16, 1.21, 1.22) only depend on the magnitude q of the scattering vector, they predict point-symmetric scattering patterns (this is rigorously true only when the irradiated volume is perfectly isotropic). Therefore, it is customary to azimuthally integrate the two-dimensional scattering patterns, obtaining radial intensity profiles that only depend on q and follow Porod's law in their terminal part (large q values).

1.1.3 Scanning SAXS of adherent mammalian cells

When studying a heterogeneous sample, the structure of which is different at different positions, it is very useful to collect the SAXS signal generated from different positions of the sample. This is the reason why scanning SAXS, or position-resolved SAXS, was first developed and applied to bone and wood in 1997 [37]. Ever since, scanning SAXS usage spread widely, with numerous applications not only to bones [38–44], but also to teeth [45–48], tendons [49, 50], plastics [51], rocks [52], amyloid fibrils and wormlike micelles in microfluidic flow [53], corneas [54], cardiac tissue [15, 55–57], calcifications in breast tissue [58] and artery aneurism tissue [59], decellularized pericardium tissue [60] and lipid vescicles in a free-standing gel [61]. In all these cases, the sample is raster-scanned through an X-ray beam; at each position, a two-dimensional scattering pattern is recorded by an area detector located far from the sample, so that the small angle condition is met. Since the majority of the high-energy beam travels undisturbed through the sample, the detector is shielded from the unscattered beam intensity by a beam stop. As evident from the examples above, scanning SAXS is mostly used on relatively strongly scattering samples (in the context of biological and soft matter), thanks to either their mineral content or their ordered structure. However, in the last decade scanning SAXS has been successfully applied to single mammalian cells. The low electron density contrast of cellular material in its natural aqueous environment can be improved by freeze-drying the cells [56, 62–69], so that the cellular material is immersed in air instead of water. Scanning SAXS was also demonstrated on chemically fixed, hydrated samples [70, 71] and on (initially) living, hydrated cells [56, 71]. Freeze-dried samples not only scatter more, but they are also less subject to radiation damage, as the aqueous environment contributes to the formation and spreading of radical species that are responsible for secondary radiation damage [72, 73]. Nevertheless, the development of effective ways to apply scanning SAXS to hydrated cells is highly advisable, in order to gain information on systems closer to physiological conditions. Because of the problems caused by aqueous environments to the quality of the signal and to radiation damage, any satisfactory sample environment for hydrated cells should contain as little water as possible.

Another challenge in the study of mammalian cells, actually pervasive in all biological contexts, is the necessity of collecting a large pool of data: cells are highly variable, thus the properties of one cell do not necessarily translate to the population to which it belongs. In imaging techniques, this translates into a contraposition between the need for a large field-of-view and that for high spatial resolution. Several solutions to the problem have been presented for different imaging techniques, such as simultaneous scanning of different regions of a sample thanks to multiple electron beams in scanning electron microscopy [13] or changes in the illumination strategy in super-resolution fluorescence microscopy [11, 12]. In scanning SAXS, a large field-of-view can be achieved by speeding up the scanning as much as possible: this was realized by a continuous movement of the sample and by careful synchronization of the detector acquisition [15]. Once a large field-of-view dataset is obtained, it needs to be analyzed; a useful tool for navigating the scan and relating the position on the sample with its corresponding SAXS scattering pattern is the so-called dark field contrast image of the scan [50]. Each pixel of a dark field contrast image corresponds to a different scan position; the intensity value of a pixel is the sum of all the intensity values that make up the scattering pattern acquired at the corresponding position. In other words, the two-dimensional scattering pattern is integrated over the detector area. This operation yields a pseudo-real space image of the sample, thus it can be used to associate different points within the sample with their corresponding scattering pattern.

1.2 Image processing and segmentation tools

The large field-of-view dark field contrast images obtained by scanning SAXS can be segmented to define different regions of interest to be used in the analysis of scattering patterns. To this end, a few fundamental image processing concepts, particularly concerning image segmentation strategies and morphological operations on binary images are presented. Image segmentation is a vast field, and a complete review of the methods used in digital image processing and computer vision to recognize objects in an automated way is far beyond the scope of the current work. Reference [74] defines image segmentation as "a process of partitioning the image into some non-intersecting regions such that each region is homogeneous and the union of no two adjacent regions is homogeneous". The paper reviews numerous image segmentation techniques, including histogram thresholding, iterative pixel classification, surface based segmentation, edge detection and methods based on fuzzy set theory. A key concept in this context is that there is no universal answer for the image segmentation problem: different approaches are suitable to different kinds of images. A segmentation method can be adapted to a given kind of image by using a model of the way the image is formed, or exploiting a particular property of the objects to be segmented. Alternatively, neural network- and deep learning-based segmentation techniques can be used, the advantage being that they require no model: in principle, the segmentation will be good if the training data set is representative of the images to be analyzed. Therefore, these type of techniques has been widely developed and used in recent years. As an example, a review of deep learning segmentation techniques for the particular case of medical images that focuses on the difficulty to have perfect training data sets and how to address the issue can be found in Reference [75]. As will be shown in Section 3.1, a segmentation based on intensity thresholds is effective in the case of our dark field contrast images of adherent cells: thus, this relatively straightforward kind of strategy is presented below. The concrete result of image segmentation is a set of binary images, or "masks", that indicate which pixels of the original image belong to a given region of interest. The quality of a mask can be improved by a suitable use of morphological operations, that can for instance smooth out the contours of an object or remove undesired noise or holes from the mask.

1.2.1 Intensity thresholding

Image thresholding techniques aim to divide the pixels of a given gray scale image into two classes: foreground pixels, that constitute the objects of interest in the image, and background pixels, *i. e.* all the pixels that do not belong to an object of interest. The division is based on a threshold value: the pixels with intensity above the threshold belong to one class, the ones with intensity below the threshold to the other class (which class is the foreground and which is the background depends on the kind of image). This kind of operation is also called "binarization" of the image, as its result is expressed as a binary image of the same size as the original image, customarily having ones marking the foreground positions and zeros marking the background positions. While the concept of binarization itself is simple enough, the choice of a threshold value can be a challenging operation. An extensive survey of image thresholding techniques can be found in Reference [76], where 40 different methods are classified into different categories and their performances are evaluated and ranked based on five quantitative criteria.

A very popular threshold selection method is Otsu's method [77]. Otsu's method is a histogram shape-based, clustering thresholding method [76]. An intensity threshold is viewed as an intensity value that divides the gray-level histogram of a given image into two classes, the foreground and the background. Each intensity value t can be considered a candidate threshold. Any given candidate threshold t defines two classes of intensity and their variances $\sigma_1^2(t)$ and $\sigma_2^2(t)$ can be calculated for every possible t. Additionally, class weights $w_1(t)$ and $w_2(t)$ can be associated to each class, defined as the probability that a pixel belongs to the class. Otsu's threshold is the intensity value t^* that minimizes the weighted sum of variances

$$\sigma_{\mathrm{w}}^2 = w_1(t)\sigma_1^2(t) + w_2(t)\sigma_2^2(t). \tag{1.23}$$

Otsu's method works best when the intensity values have a bimodal distribution and when background and foreground contain a similar number of pixels, and it is by no means perfect [76, 78]. Nevertheless, it is comparatively effective, easy to implement and the underlying theory is easy to extend to multithresholding: therefore, it is a very popular thresholding technique, available in most image analysis software packages.

Otsu's method is an example of global thresholding: a single threshold value is chosen and applied to all pixels of the image. Global thresholds tend to fail when the foreground objects are considerably smaller than the background, and when the foreground and background intensity distributions overlap. Local intensity thresholds can help solving this problem, particularly when the foreground and background intensity distributions are still distinct in smaller portions of the image, but not all throughout the full image. In this case, a different threshold is associated to each pixel of the image by computing it within a neighbourhood centered on the pixel itself. The local threshold can be defined in a variety of ways, for instance using the local intensity variance or the local intensity contrast [76]. A very simple case that proved to be very effective on dark field contrast images of adherent mammalian cells (see Section 3.1), consists in calculating the local mean intensity and defining the threshold as a fraction of it (Bradley's method [79]).

1.2.2 Morphological operations

After an image segmentation method such as intensity thresholding has been applied, the resulting binary image is not necessarily a perfect representation of the foreground and background of the original image. For instance, small background regions might have been included into the foreground, especially if the original image is noisy. The foreground region might present unwanted holes or gaps that need to be filled, or there could be objects connected by thin features that we would want to be separated. In these instances of purely morphological defects,

that only depend on the relative positions of the foreground pixels and not by their intensity, morphological operations can vastly improve the binary image. Rigorously, morphological operations are operations defined between two sets of N-dimensional vectors, with $N = 2$ for two-dimensional images [80]. Each set of vectors represents a binary image, with each vector indicating the position of a foreground pixel. In more practical terms, a morphological operation uses a small binary image, called structuring element, to reshape the foreground objects of a given binary image. For example, dilation is a way to expand the foreground [81]. Formally, considering the original binary image and the structuring element as two sets of two-dimensional vectors, in order to dilate the image by the structuring element, all possible pairs of vectors with one vector belonging to the image and the other belonging to the structuring element should be formed. The dilated image is the set of all vectors obtained by summing the two elements of a pair [80]. Effectively, the dilation can be obtained from the original image by adding copies of the structuring element to it: as many copies as the number of pixels forming the perimeter of the objects in the foreground, with each copy centered on one of the pixels of the perimeter [82].

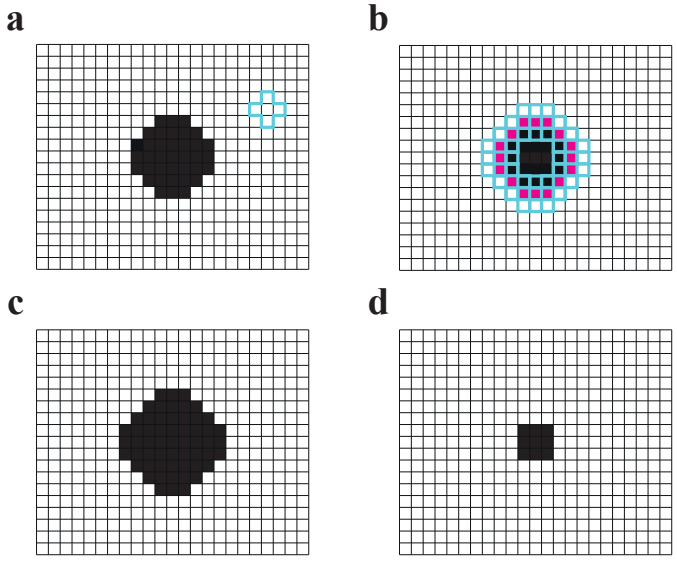

Figure 1.2: Simplified interpretation of dilation and erosion. a) Original object (black) and structural element (outlined in blue). b) Original object (black) with the pixels of its perimeter in red. Each pixel of the perimeter is also the center of a copy of the structural element (outlined in blue). c) Dilation of the original object by the structuring element. d) Erosion of the original object by the structuring element.

An example of binary object is shown in Figure 1.2a in black, along with an example of structuring element outlined in blue. In Figure 1.2b, the same object is shown again, with the pixels of its perimeter depicted in red. Each red pixel is also the center of a copy of the structuring element (blue). The dilation of the object is obtained by adding all of the pixels within blue outlines to it (Figure 1.2c). The dual operation to dilation is called erosion. Erosion is also formally defined using vector subtraction [80], and it amounts to overlapping the center of the structuring element with the perimeter pixels of the foreground objects and subtracting the pixels of the intersection between object and structuring element (Figure 1.2d). In the example, each pixel outlined in blue in Figure 1.2b needs to be subtracted from the object.

Erosion and dilation of a slightly more complex binary image by the same structuring element are shown in Figure 1.3. The original image is shown in Figure 1.3a, the structuring element in Figure 1.3b, the result of dilation in Figure 1.3c and the result of erosion in Figure 1.3d. Erosion and dilation can be applied after one another, and changing the order in which

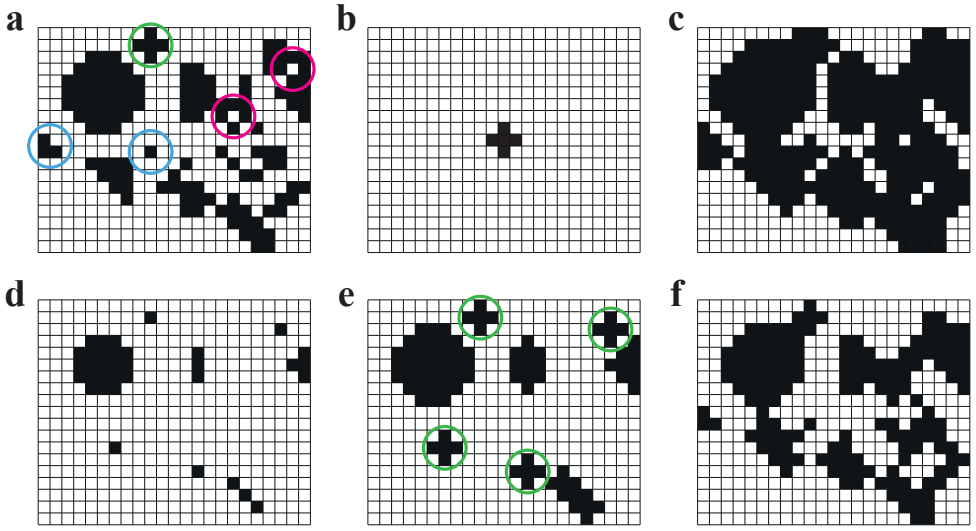

Figure 1.3: Example of application of basic morphological operations. a) Original binary image (foreground in black, background in white). The blue circles mark one-pixel or few-pixels objects. The red circles mark small holes. The green circle marks an object of the same size and shape as the structuring element. b) Structuring element. c) Dilation of the image in panel a by the structuring element in panel b. d) Erosion of the image in panel a by the structuring element in panel b. e) Opening of the image in panel a by the structuring element in panel b. The green circles mark objects of the same size and shape as the structuring element. f) Closing of the image in panel a by the structuring element in panel b.

they are applied changes the outcome. An erosion followed by a dilation is called an opening, because it tends to "open up" small cracks in the foreground objects [80–82]. Morphological opening can be used to separate barely touching objects and to remove objects smaller than the structuring element. For example, the opening of Figure 1.3a by the structuring element shown in Figure 1.3b results in Figure 1.3e, where the small objects marked in Figure 1.3a by blue circles have been removed. Additionally, opening can be used to detect objects of the same size and shape as the structuring element (green circles in the example). Conversely, a dilation followed by an erosion is called a closing, as it tends to "close" small cracks in the foreground objects [80–82]. Morphological closing can fill holes smaller than the structuring element, such as those marked by red circles in Figure 1.3a, that are no longer present in the closed image (Figure 1.3f). This simplified overview of the four fundamental morphological operations is sufficient to put them to good use in the refinement of binarized dark field contrast images, as will be shown in Section 3.1.

Chapter 2

Materials and methods

This chapter is devoted to the description of the materials, instrumentation and methods employed to perform the experiments presented and discussed in this work. Section 2.1 introduces the cell lines measured. Section 2.2 details how the samples are prepared for measurements, and Section 2.3 explains how the measurements take place.

2.1 Cell culture

2.1.1 NIH-3T3 fibroblasts

3T3 mouse embryonic fibroblasts are a widely used adherent cell line, originally developed as a target for transformation by oncogenic viruses [83, 84]. NIH-3T3 fibroblasts, in particular, are currently considered a standard fibroblast cell line, being relatively easy to culture and contact inhibited. The cells we use are purchased through DSMZ (ACC-59-NIH-3T3 fibroblasts [85–87], Leibniz Institute DSMZ – German Collection of Microorganisms and Cell Cultures GmbH, Braunschweig, Germany).

The cells are cultured in high glucose ($4.5\,\mathrm{g\,L^{-1}}$) Dulbecco's Modified Eagle's Medium (DMEM, D6429; Sigma-Aldrich, Merck KGaA, Darmstadt, Germany), supplemented with 1% (v/v) glutaMAX (35050-061; Gibco, Thermo Fisher Scientific, Waltham, MA, USA), 100 units/mL penicilin-streptomycin (pen-strep, 15140-122; Gibco) and 10% (v/v) fetal bovine serum (FBS, F0804; Sigma-Aldrich). The culture vessels are kept in a cell incubator (Heracell 150 or Heracell VIOS 160i, Thermo Electron LED GmbH, Langenselbold, Germany) at 37 °C and 5% CO_2 in a water-saturated atmosphere. Cell passaging is carried out every 3-4 days, when the cells are at least 70% confluent. To this end, the cells are rinsed with 0.02% (w/v) ethylenediamine tetraacetic acid (EDTA, 8040.2; Carl Roth GmbH, Karlsruhe, Germany) in phosphate buffered saline (PBS; either prepared in-house by dissolving 0.137 M NaCl, 2.7 mM KCl, 4.3 mM Na_2HPO_4 and 1.4 mM KH_2PO_4 in ultra pure water to obtain a pH of 7.2 or purchased: Dulbecco's phosphate buffered saline, D8537; Sigma-Aldrich). Trypsin solution (0.02% (w/v) EDTA in PBS, 0.05% (w/v) trypsin, T4799; Sigma-Aldrich) is added and the cells are subsequently incubated at 37 °C and 5% CO_2 for 2.5 min. Cells are then resuspended in medium and plated at a suitable concentration (the usual volume ratio is 1:5 cell suspension to medium).

2.1.2 Vimentin knockout fibroblasts

Three vimentin knockout fibroblast lines are kindly provided by prof. Harald Herrmann (Universitätsklinikum Erlangen, Germany). The first of these cell lines, mouse embryonic fibroblasts lacking vimentin (vim -/- cells), were originally developed in order to investigate the role of

the intermediate filament protein vimentin in cells [88–90]. As their name suggests, they are derived from mice embryos. Once established, vim -/- cells are fairly easy to culture. As they do not express any cytoplasmic intermediate filament proteins, they can be used as a model system to study the structures that different cytoplasmic intermediate filaments form in a minimal cellular environment, e. g. different mutants of the human intermediate filament protein desmin [91–93]. In particular, the other two cell lines considered in this work are vim -/- cells stably expressing human wild-type desmin (vim -/- + hDes WT) and vim -/- cells stably expressing the human R406W mutant desmin (vim -/- + hDes R406W).

These cells are cultured in high glucose ($4.5\,\mathrm{g\,L^{-1}}$) DMEM (41965-039; Gibco, Thermo Fisher Scientific), supplemented with 1% (v/v) glutaMAX, 100 units/mL pen-strep and 10% (v/v) FBS (S0115; Biochrom, Merck KGaA). For the cells expressing desmin, 2% (v/v) geneticin (10131027; Gibco, Thermo Fisher Scientific) is added to the medium. The cells are passaged every 3-4 days, when they are at least 70% confluent. First, they are rinsed with 0.02% (w/v) EDTA in PBS. They are subsequently wetted with trypsin solution (0.25% (w/v) trypsin, 0.02% (w/v) EDTA in PBS), which is removed prior to incubation at 37 °C and 5% CO_2 for 5 min. Finally, the cells are resuspended in medium and plated at a suitable concentration (the usual volume ratio is 1:10 cell suspension to medium for vim -/- cells and 1:4 for vim -/- + hDes cells).

2.2 Sample preparation

In order to obtain samples for X-ray measurements or optical microscopy imaging, cells are grown on appropriate supports: to optimize the quality of the X-ray and optical microscopy images, cells are grown on silicon nitride membranes and glass coverslips, respectively. For the X-ray samples, silicon nitride membranes (frame size 5 mm × 5 mm, membrane size 1.5 mm × 1.5 mm, frame thickness 200 µm, membrane thickness 1000 nm; Silson Ltd, Warwickshire, UK) are plasma-cleaned (Zepto low-pressure plasma cleaner; Diener Electronics GmbH, Ebhausen, Germany) with air plasma at 40 W for about 30 s, so that their flat side becomes hydrophilic. Each silicon nitride membrane is then transferred to an individual cell culture Petri dish filled with medium, with their flat side facing upwards. 8×10^4 to 15×10^4 cells are plated on the dish and they are left to adhere and proliferate on the silicon nitride membrane in the cell incubator as for usual cell culture. The cell growth is regularly monitored by phase contrast imaging (CKX53 Cell Culture Microscope; Olympus Europa SE & CO. KG, Hamburg, Germany). A similar strategy is adopted to culture cells on glass coverslips (no. 1.5H, 18 mm diameter; LH23.1, Carl Roth), although in this case plasma cleaning is not needed; the coverslips are simply placed in ultra pure water and autoclaved in order to sterilize them before use.

2.2.1 Cell fixation

Cells grown on either silicon nitride membranes or glass coverslips are chemically fixed 12 h to 136 h after plating, depending on the cell growth rate, on the cell number at the time point of plating and on the desired final cell concentration. Chemical fixation aims to prevent autolysis and degradation of the cell while preserving its structure and components in time, effectively acting as a snapshot of the cell status at the moment of fixation [94, 95]. As some chemical and/or physical modification is inevitable to ensure cell preservation, no fixed cell is identical to its living form, and different fixatives are prone to different artifacts. Therefore, a fixative is chosen depending on the technique that will be used to investigate the sample.

For X-ray samples 3.7 % formaldehyde, obtained by diluting 37 % formaldehyde solution (stabilized with 10 % methanol; 104002, Merck KGaA) in PBS 1:10 (v/v), is routinely used.

The cells are rinsed twice with PBS, fixed in 3.7 % formaldehyde for 15 min to 20 min, rinsed three times with PBS and finally stored in PBS at 4 °C until further use. After fixation, phase contrast images of each silicon nitride membrane are taken (IX81 Inverted Microscope or IX83 Inverted Microscope, Olympus, equipped with a 20x objective, UCPLFLN20XPH, Olympus, numerical aperture 0.70) and stitched together to obtain an overall view of the complete membrane. For cells intended for actin staining via phalloidin [96], formaldehyde stabilized with methanol cannot be used, as methanol can destroy the native conformation of filamentous actin, thus preventing phalloidin binding [97–100]. In this case, methanol-free formaldehyde (28906; Thermo Fisher Scientific) is used instead, following the same procedure as described above.

2.2.2 Freeze-drying

The majority of the X-ray samples are freeze-dried [62–66, 73, 101, 102] before measurements. Freeze-dried (or lyophilized) samples yield a stronger scattering signal than hydrated ones, as the electron density contrast between cellular constituents and air is larger than that between cellular constituents and an aqueous environment [27, 103]. The first step to freeze-dry a sample is plunge-freezing, that is, freezing the sample as rapidly as possible, such that the formation of ice crystals, which would destroy the cellular structures, is avoided. To this end, a grid plunger (Leica EM GP; Leica Microsystems, Wetzlar, Germany) is used to ensure fast immersion of the sample in a liquid ethane-propane mixture (37 % ethane, 63 % propane, kept at about −196 °C). The sample (chemically fixed cells on a silicon nitride window) is taken out of its storage PBS and briefly dipped in ultra pure water in order to minimize the presence of salt crystals in the sample. The window is then mounted on the forceps of the grid plunger and loaded into the sample chamber, where it is kept in a water saturated environment (99 % humidity) to prevent the cells from drying. Here, the window is further rinsed with ultra pure water and then carefully blotted with filter paper, until only a thin water membrane embeds the cells. At this point, the cells are quickly submerged into the liquid ethane-propane mixture, that is kept at low temperatures by an underlying liquid nitrogen bath. The ethane-propane mixture is preferred over using liquid nitrogen directly: when liquid nitrogen is in contact with a room-temperature object a thin vapor layer will form all around it, thus the cooling of the sample is much less efficient [104].

After plunge-freezing the samples are stored in liquid nitrogen until the second step, drying, is performed. The cells are dried by Jochen Herbst (Institute for X-ray Physics, Göttingen) in a home-built freeze-drier, where a cryostat keeps them at −196 °C while the pressure is reduced under the triple point pressure of water (611.657 Pa [105]). The temperature is then increased such that the aqueous contents of the cells sublimate. Finally, the temperature and pressure are gradually brought back up to room temperature and atmospheric pressure. The complete drying process takes about three days. After the freeze-drying process phase contrast images of each silicon nitride membrane are taken (Olympus IX81 or IX83 Inverted Microscope, Olympus UCPLFLN20XPH 20x objective) and stitched together to obtain an overall view of the complete membrane. To avoid rehydration from ambient humidity, freeze-dried samples are kept in a desiccator until they are needed for measurements.

2.2.3 Sample chamber for wet samples

Freeze-dried cells have many advantages: the drying process improves the scattering signal and renders the cells less prone to radiation damage when compared to hydrated samples [72, 73]. Furthermore, freeze-dried cells can be measured in air and at room temperature without the need for a special sample environment. However, freeze-dried cells are very far

from physiological conditions and undergo shrinkage and, often, fragmentation (Figure 2.1).

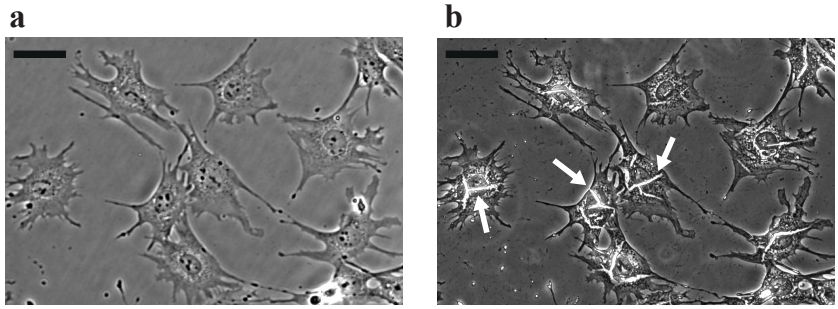

Figure 2.1: Example of cell fragmentation due to freeze-drying. a) Fixed-hydrated cells. b) Same cells as in panel a, freeze-dried. White arrows point out examples of fragmentation. Scale bars: 50 µm.

Fixed-hydrated cells, although still different from living cells, are a step closer to real-life conditions. The need to keep the cells hydrated during measurements comes with a set of challenges which are addressed by designing and implementing a sample chamber for hydrated cells on silicon nitride windows. The challenges are due to the fact that the aqueous environment lowers the electron density contrast and facilitates the spreading of radiation damage. Thus, the water layer in the sample chamber needs to be as thin as possible. Consequently, the cells will dry very easily, unless the chamber is absolutely leak-tight. A previously developed [106] wet sample chamber was manufactured using silicon nitride membranes in a "sandwich" configuration, where the concave side of one silicon nitride window was glued to the flat side of a second window, as shown in Figure 2.2.

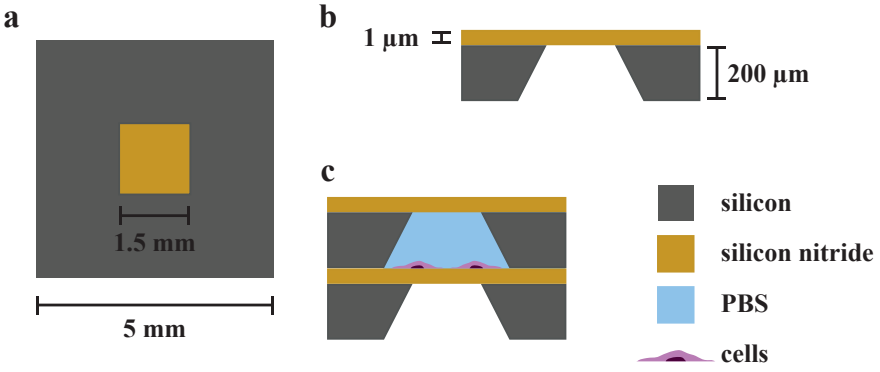

Figure 2.2: Schematic of a simple silicon nitride "sandwich" wet sample chamber (not to scale). a) Silicon nitride window, top view. b) Silicon nitride window, side view. c) Wet sample chamber obtained by sandwiching the cells between the flat membrane they are grown on and a second window with its well side facing the cells.

In this configuration the thickness of the window frame determines the thickness of the water layer, *i. e.* 200 µm. With hard X-rays, this amount of water results in a strong background that disturbs the signal originating from the cell itself. To circumvent this risk, the aforementioned sample chamber design is modified such that the two flat sides of the membranes face each other, as shown in Figure 2.5. Furthermore, there is a considerable risk that the glue enters the chamber. Thus, in our design the silicon nitride window "sandwich" is held together not by glue, but by placing it between two metallic frames that are screwed together. A photograph of two such frames is shown in Figure 2.3. One of the frames (Figure 2.3a) has an indention as deep as twice the thickness of the silicon frame of a window, so that the two windows are

kept as close as possible. This frame hosts a sealing ring outside of the indented area, and four holes around the sealing ring that match the holes in the other frame (Figure 2.3b), where the screws are placed.

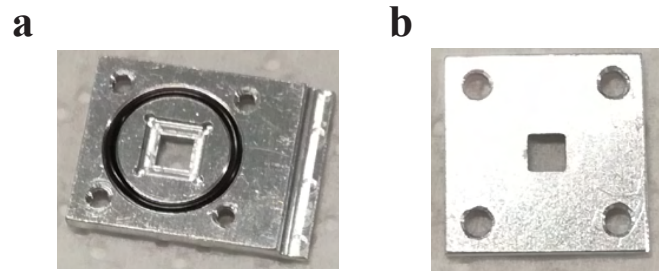

Figure 2.3: Photograph of the metallic frames used to keep the wet sample chamber together. a) Indented frame. b) Flat frame.

Polydimethylsiloxane spacer

A thin polydimethylsiloxane (PDMS, Sylgard 184 Silicone Elastomer Kit; Dow Silicones Corporation, Midland, MI, USA) spacer is placed on the silicon nitride frame to define the thickness of the chamber. The spacer is obtained as a soft lithography replica of a structured master.

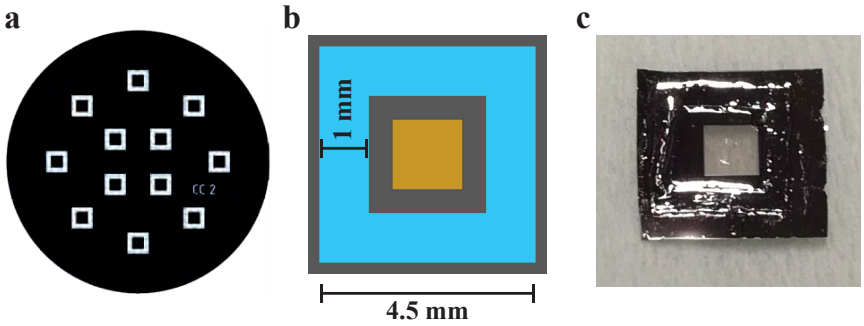

Figure 2.4: PDMS spacer. a) Photomask used to obtain the master. b) Schematic of the PDMS spacer on top of a silicon nitride window (not to scale). c) Photo of a PDMS spacer on top of a silicon nitride window.

The master is fabricated by photolitography in a class 100 cleanroom using SU-8 negative photoresist (SU-8 3025, Kayaku Advanced Materials Inc., Westborough, MA, USA). The photoresist is spin-coated on a 2-inch silicon wafer (MicroChemicals GmbH, Ulm, Germany) at a final velocity of 4000 rpm, resulting in a 17 µm–20 µm thick photoresist layer. The wafer is then soft-baked at 65 °C for 1 min and at 95 °C for 9 min. Next, a film photomask (Figure 2.3a. Designed with AutoCAD 2020, Autodesk Inc., San Rafael, CA, USA and printed by Selba S. A., Versoix, Switzerland) is overlaid and aligned to the wafer (MJB4 Mask-Aligner; Süss MicroTec AG, Garching, Germany). The wafer is exposed to UV light for 5 s, so that the irradiated area of the photoresist is crosslinked. Afterwards, the wafer is baked at 65 °C for 1 min and at 95 °C for 5 min. The wafer is then developed (MR-Dev-600; Micro Resist Technologies GmbH, Berlin, Germany) to remove the non-exposed photoresist and hard-baked at 200 °C for 10 min. Outside the clean room, the wafer is vapor-coated with (heptafluoropropyl)-trimethylsilane (431044; Sigma-Aldrich) overnight. This step facilitates the removal of the PDMS replicas from the master. One master wafer can be used to obtain 12 PDMS spacers (corresponding to the white squares in the photomask shown in Figure 2.3a).

In order to obtain the PDMS spacers, a 10:1 PDMS-to-crosslinker mixture is degassed and spin-coated (G3P-8 Spin Coater; Specialty Coating Systems Inc., Indianapolis, IN, USA) onto the master wafer at 2500 rpm for 30 s yielding spacers of approximately 30 µm thickness, which is slightly thicker than a typical cell. The PDMS is then baked at 65 °C for about 1 h. It should be noted that the spacers are thicker than the photoresist structures of the master. This helps removing the spacers from the wafer: after backing, the PDMS is a thin layer that covers all of the wafer and it is thicker in correspondence of the spacer-shaped holes of the master. Therefore, it is possible to cut all around the holes, to keep some excess PDMS all around the spacer. This excess PDMS margin can be used to peel the spacer away from the master and it helps with handling it. The outer and inner perimeter of the spacer appear like indentions in the thin PDMS layer, which can be used as guidelines when the margin and inner square part are cut out and removed to obtain the actual spacer.

When needed, a spacer is cut out of the mold with a scalpel, gently removed with the help of some tweezers and isopropanol and placed on a flat piece of aluminum foil. The central square part and the excess PDMS margin are removed. The PDMS spacer is plasma-cleaned together with an empty silicon nitride window (with its flat side facing upwards) at 40 W for about 30 s. The silicon nitride window is then immediately placed on top of the spacer under a stereomicroscope (Olympus SZ61), transferred onto a hot plate at about 95 °C and gently pressed to facilitate the bond between the silicon frame and the PDMS spacer. After a few minutes, the window is removed from the hot plate and the aluminum foil is peeled away. A typical result of this procedure is shown in Figure 2.3c. The window is then plasma treated once more, to render its membrane hydrophilic, and is subsequently stored in ultra pure water for at least 24 h. During this time the membrane stays hydrophilic and the PDMS spacer gets water-saturated. Indeed, PDMS is permeable to water [107–109], so to avoid drying of the sample chamber the spacer is saturated with water and its sides are sealed with a two-component silicone (Twinsil Extrahart; Picodent, Dental-Produktions- und Vertriebs-GmbH, Wipperfürth, Germany). The two-component silicone is easy to apply, fast to cure and the risk that it enters the chamber is low as it is highly hydrophobic.

Assembly of the sample chamber

The assembly of the wet sample chamber starts by taking a silicon nitride window with PDMS spacer, hereinafter referred to as "PDMS window", from its storage water and blotting it dry, taking particular care to dry the portion of silicon frame outside of the PDMS spacer. A rim of silicone is then added along the perimeter of the PDMS spacer (Figure 2.5a, b), and the window is placed into the indented part of the metallic frame mentioned above. A silicon nitride window containing fixed-hydrated cells, hereinafter referred to as "cell window", is taken from the fridge, and a small droplet (roughly 6 µL) of storage liquid of the cells is placed on the membrane of the PDMS window (Figure 2.5c, d). The cell window is dipped in ultra pure water to remove PBS from the concave part of the window: if salt crystals formed outside of the wet chamber, they would disturb the scattering signal. The frame of the cell window is quickly blotted and then laid on top of the PDMS window, with the cells facing downwards, so that they are inside the chamber and submerged in their storage liquid (Figure 2.5e, f). Finally, the flat metallic frame is placed on top of the indented one, and the two are screwed together (Figure 2.5g). By imaging a wet sample chamber in a time series started right after assembly (phase contrast, Olympus IX83 Inverted Microscope, Olympus UCPLFLN20XPH 20x objective), we found that evaporation from the chamber starts about 4 h after assembly, and it slowly proceeds until about 19 h after assembly. This would allow measurements if they were started directly after assembly; however, since the samples are assembled in-house and then shipped to the synchrotron, the sample chambers are put in ultra pure water right after

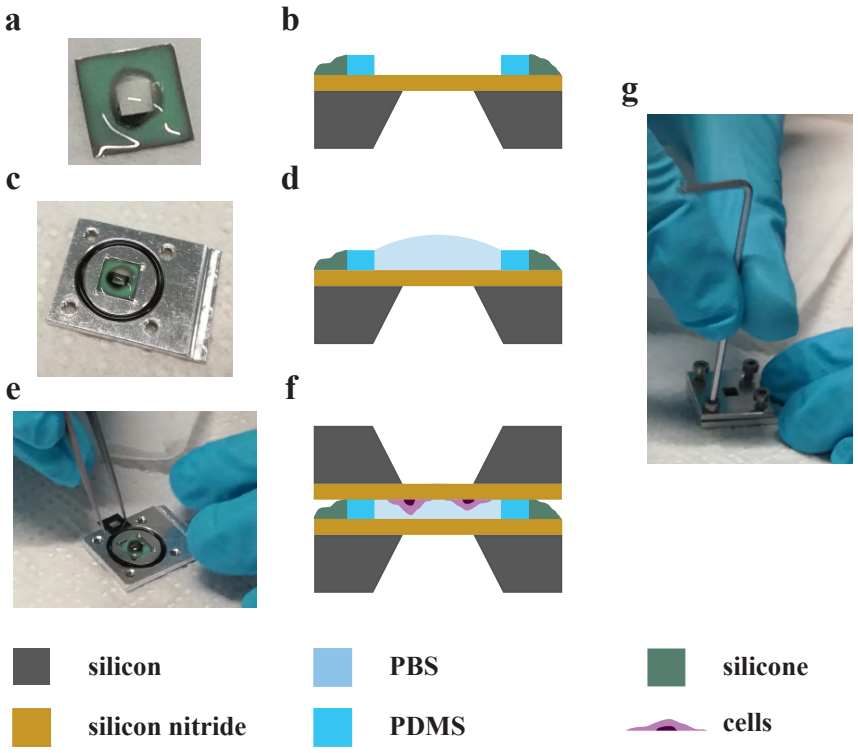

Figure 2.5: Assembly of the sample chamber. a) Photograph of the PDMS window with Twinsil Extrahart silicone sealing the PDMS spacer. b) Schematic of the PDMS window with Twinsil Extrahart silicone, side view (not to scale). c) Photograph of the PDMS window in the metallic frame, with a PBS droplet on top of the membrane. d) Schematic of the PDMS window with PBS, side view (not to scale; the metallic frame is omitted). e) Photograph of the cell window being transferred onto the PDMS window. d) Schematic of the complete wet sample chamber, side view (not to scale; the metallic frame is omitted). f) Photograph of the sample chamber being screwed together.

assembly and kept there at all times until right before they are measured, to avoid drying.

2.3 Sample characterization

The cellular samples are mainly characterized by scanning small-angle X-ray scattering (SAXS). As described above, cells are grown on silicon nitride windows and then measured at a synchrotron, in either the freeze-dried or fixed-hydrated state. Visible light phase contrast microscopy is used to monitor cellular changes during all steps of the sample preparation process. In addition, micrographs are recorded yielding overview images of the samples, which are useful when navigating a sample to find suitable regions to measure during X-ray measurements. Moreover, we use fluorescent dyes to label the actin network and the desmin in the vim -/-, vim -/- + hDes WT and vim -/- + hDes R406W cell lines, in order to visualize the expression of the two different kinds of desmin, and to verify if obvious differences in the actin network of the three cell lines can be seen.

2.3.1 Fluorescence microscopy

In preparation of fluorescence microscopy, cells are grown on glass coverslips and fixed with methanol-free formaldehyde, as described above. The cells are permeabilized by placing them on a shaker for 10 min after addition of 0.1 % (v/v) Triton X 100 (3051.3; Carl Roth) in PBS. The permeabilizing solution is then removed and the cells are washed three times in PBS; each time, they are left on the shaker for 5 min. The coverslips are then placed in 1 % (m/v) bovine serum albumine (BSA, BSA-1U; Capricorn Scientific GmbH, Ebsdorfergrund, Germany) in PBS and left on the shaker for 60 min, to block unspecific binding. Subsequently, the coverslips are placed in a simple wet chamber, consisting of a plastic box containing wet tissue paper covered with parafilm. The coverslips are laid on top of the parafilm, so that a small drop of liquid can be added to the coverslips and stays in place, as parafilm is hydrophobic; the wet tissue paper underneath ensures that the sample does not dry out. A 100 µL droplet of staining solution is added to the coverslips, containing 1:40 (v/v) Alexa Fluor 647 Phalloidin (A22287; Thermo Fisher Scientific) and 1:400 (v/v) Alexa Fluor 488 Anti-Desmin antibody [Y66] (ab185033; Abcam, Cambridge, UK) in 1 % BSA. The wet chambers are wrapped in aluminum foil to protect them from light and left at 4 °C overnight. The coverslips are then washed three times in PBS (each time, they are left on the shaker for 5 min) and finally mounted on rectangular glass slides (76 mm × 26 mm, 1.0 mm thick, 631-1550; VWR International GmbH, Darmstadt, Germany) with ProLong Diamond Antifade Mountant (P36965; Invitrogen, Thermo Fisher Scientific). The glass slides are kept at 4 °C in the dark until they are imaged. Imaging is performed using a confocal microscope (Olympus IX81), equipped with a 100x oil immersion objective (UPLSAPO100XO, Olympus, numerical aperture 1.4) and a digital CMOS camera (ORCA-Flash4.0 LT+, C11440; Hamamatsu Photonics Deutschland GmbH, Herrsching am Ammersee, Germany). An excitation wavelength of 488 nm (provided by an argon laser) is used to image desmin; an excitation wavelength of 635 nm (provided by a laser diode) is used to image actin.

2.3.2 Scanning SAXS: fast scanning at ID13

All X-ray measurements described in this work are performed at the micro-branch (experimental hutch II) of beamline ID13 of the European Synchrotron Radiation Facility (ESRF, Grenoble, France), in the course of three different experiments in April 2017, October 2018 and September 2020. A simplified schematic of the experimental setup is shown in Figure 3.1. Parabolic beryllium compound refractive lenses (Be-CRLs) of 200 µm radius at the apex (R_A)

are used to pre-focus the beam. A channel-cut Si(111) monochromator is used to obtain a photon energy of 13.0 keV. The beam is then focused down to micrometric dimensions by Be-CRLs ($R_A = 50\,\mu m$), conditioned with a 20 µm aperture and cleaned with a 80 µm guard aperture. The specific beam sizes and photon fluxes used in the different experiments are listed in Table 2.1. A sample is mounted on a piezoelectric scanning stage that is mounted on a hexapod stage: the hexapod stage provides coarse movements for sample positioning and alignment, the piezoelectric stage is used for the finer movements of the scans. A 70 mm flight tube filled with helium is placed downstream of the sample to reduce air scattering. When needed, a visible-light microscope can substitute the flight tube to align the sample. Right outside of the flight tube, the primary beam is blocked by a beam stop, thus protecting the detector, an Eiger X 4M (2017×2167 pixels, pixel size $75\,\mu m \times 75\,\mu m$; Dectris Ltd., Baden-Daettwil, Switzerland). Along with the "traditional" raster scanning mode, in which the sample is stationary during acquisitions, a "fast scanning" mode is possible, by moving the sample continuously at constant speed while the data acquisition is in progress [15, 50].

The setup used during the September 2020 experiment is similar to the one just described, with a noteworthy difference: the experiment takes place after the "Extremely Brilliant Source" (EBS) upgrade of ESRF [110]. The increased brilliance and coherence of the EBS-ESRF allow for a clean, focused beam using fewer CRLs to be rendered, thus resulting in a higher photon flux (see Table 2.1).

Table 2.1: Experimental parameters for the three different experiments presented in this work.

Experiment	Photon flux [cps]	Beam size [µm]	Sample-detector distance [m]
April 2017	$1.7 \cdot 10^{12}$	2×3	0.935
October 2018	$1.2 \cdot 10^{12}$	1.5×3	0.962
September 2020	$2.5 \cdot 10^{12}$	2×2	0.778

Unless otherwise stated, all the analysis of scanning SAXS data is performed by using Matlab (The MathWorks, Inc., Natick, MA, USA), version R2017b or later releases, including the Image Processing Toolbox and the Parallel Computing Toolbox. The power law fits discussed in Chapter 3 are all obtained by a non-linear least-squares minimization.

Chapter 3

Results and discussion

In this chapter, the results of scanning small-angle X-ray scattering (SAXS) on mouse embryonic fibroblasts are presented and discussed. Section 3.1 illustrates the way that large field-of-view dark field contrast images from scanning SAXS can be segmented into regions of interest, and how such segmentation enables further analysis. Section 3.2 uses scanning SAXS to compare three different cell lines. Section 3.3 compares the scanning SAXS signal of biological cells obtained the at the European Synchrotron Radiation Facility (ESRF) before and after its "Extremely Brilliant Source" (EBS) upgrade.

3.1 Segmentation of dark field contrast images from scanning SAXS

Scanning small-angle X-ray scattering (SAXS) in "fast" scanning mode of mouse embryonic fibroblasts on silicon nitride membranes provide low-intensity, membrane-wide scans consisting of up to 9×10^6 scattering patterns. The dark field contrast image of a scan is key in connecting the sample position with its corresponding scattering pattern: therefore, no analysis can take place without dividing the dark field contrast image into regions of interest, such as cell bodies or nuclei. The large dimensions of a membrane-wide dark field contrast image, and the low intensity of the signal due to the short exposure times necessary for fast acquisition present a series of challenges that need to be resolved by adequate treatment. The article reproduced below exemplifies the kind of analysis enabled by a good segmentation strategy.

3.1.1 Large field-of-view scanning small-angle X-ray scattering of mammalian cells

This section has been published as Chiara Cassini et al. "Large field-of-view scanning small-angle X-ray scattering of mammalian cells". In: *J. Synchrotron Radiat.* 27.4 (2020), pp. 1059–1068. DOI: 10.1107/s1600577520006864.

Chiara Cassini,[a,b] Andrew Wittmeier,[a] Gerrit Brehm,[a,b] Manuela Denz,[a] Manfred Burghammer[c] and Sarah Köster[a,b]

[a]Institute for X-Ray Physics, University of Göttingen, Friedrich-Hund-Platz 1, 37077 Göttingen, Germany
[b]Cluster of Excellence "Multiscale Bioimaging: from Molecular Machines to Networks of Excitable Cells" (MBExC), University of Göttingen, Germany
[c]European Synchrotron Radiation Facility, 71, Avenue des Martyrs, 38043 Grenoble, France

Author contributions: S. K. conceived and supervised the project. C. C., S. K., A. W., G. B. and M. D. collected SAXS data with the support of M. B. A. W. prepared the samples. C. C. analyzed the data. C. C. and S. K. wrote the manuscript, with input from all authors.

Keywords: biological cells, nanostructures, high throughput, scanning SAXS, image segmentation.

X-ray imaging is a complementary method to electron and fluorescence microscopy for studying biological cells. In particular, scanning small-angle X-ray scattering provides overview images of whole cells in real space as well as local, high-resolution reciprocal space information, rendering it suitable to investigate subcellular nanostructures in unsliced cells. One persisting challenge in cell studies is achieving high throughput in reasonable times. To this end, a fast scanning mode is used to image hundreds of cells in a single scan. A way of dealing with the vast amount of data thus collected is suggested, including a segmentation procedure and three complementary kinds of analysis, *i. e.* characterization of the cell population as a whole, of single cells and of different parts of the same cell. The results show that short exposure times, which enable faster scans and reduce radiation damage, still yield information in agreement with longer exposure times.

Introduction

Imaging biological cells with a spatial resolution sufficient for identifying subcellular structures is a very challenging task, currently tackled mainly by three kinds of probes: electrons, visible-light fluorescence and X-rays. Electron microscopy [1, 2] yields the best spatial resolution, resolving details down to the subnanometer range. However, it requires extensive sample preparation, typically including slicing and staining of the sample. Thanks to super-resolution techniques [3], fluorescence microscopy is widely used in labeled, intact cells [4, 5] and can resolve details on the order of tens of nanometers. X-ray imaging techniques [6, 7] rely on the small wavelength and high penetration depth of X-radiation. In particular, scanning small-angle X-ray scattering (SAXS) [8] is used on unsliced, unstained samples to obtain both real and reciprocal space information. A large variety of samples can be examined with this technique, including, but not limited to, bone [8–11], wood [8, 12] and teeth [13, 14]. In real space, the dark-field contrast image [15] offers an overview of the scanned area. The real-space resolution is limited by the dimensions of the X-ray beam and the step size of the scan. In reciprocal space, scanning SAXS can access the nanometer range *via* scattering patterns collected at each position of the scan. Thus, moderate resolution in real space is complemented by high resolution in reciprocal space. Thanks to this unique combination, several subcellular structures were studied in whole cells, including keratin bundles in SK8/18-2 cells [16–18], actin bundles in hair cell stereocilia [19] and in *Dictyostelium discoideum* [20] and chromatin in 3T3 fibroblasts [21]. A model-free diffraction pattern analysis was demonstrated for several cell types [22]. Notably, all these studies typically took into account only about 2-30 cells in total; when different cell types [22], differently prepared samples [17, 20] or cells in different stages of the cell cycle [21] were compared, each of the compared groups included at most ten cells.

Since cell-to-cell variability occurs even within the same monoclonal population [23], any cellular assay should include a statistically significant number of cells. However, achieving high resolution for a large number of cells in a single experiment is very challenging. The conditions for high spatial resolution usually limit the accessible field-of-view. This results in a low number of cells per acquisition, thus longer times are needed for large numbers of cells to be assessed. Recent attempts to overcome these limitations include, for super-resolution fluorescence techniques, the development of a large and uniform epi-illumination [24] or the decoupling of illumination and detection pathways with slab waveguides [25]. Multiple electron beams can extend the field-of-view of scanning electron microscopy by simultaneously scanning as many regions as the number of beams employed [26]. Field-of-view expansion has been demonstrated for scanning SAXS on cardiac tissue, thanks to a novel fast scanning mode [27] that resulted in a field-of-view of 6 mm × 5 mm with a pixel size of 5 µm for the dark-field contrast image.

Here, we use fast scanning SAXS to study single cells, thus accessing the subcellular structural information provided by the scattering patterns, corresponding to typical lengths of few nanometers to few tens of nanometers, while obtaining a panoramic view of the entire cell population (1.5 mm × 1.5 mm field-of-view) from the dark-field contrast image. Regardless of the imaging method, measurements carried out with high resolution over a large field-of-view lead to vast amounts of data that need to be handled in a time-efficient manner [26–28]. Here, we present a segmentation strategy for the dark-field contrast image that is key to dividing the data into regions of interest (ROIs), thus enabling further analysis in feasible times. Different levels of analysis, focusing on the overall cell population, on the characteristics of different cells or on the properties of different parts of the same cell are illustrated, as well as an application example that corroborates previous results with data from a more substantial number of cells. In particular, we pay attention to effects of radiation damage, which still pose a major challenge when imaging biological matter by X-rays. We thus enable statistically meaningful data acquisition and analysis by scanning SAXS and render it a complementary method to other

nanoscale imaging methods.

Materials and methods

Cell culture and sample preparation NIH-3T3 fibroblasts derived from Swiss albino mouse embryos [29] were cultured in high glucose ($4.5\,\mathrm{g\,L^{-1}}$) Dulbecco's Modified Eagle's Medium (DMEM, D6429; Sigma-Aldrich, Merck KGaA, Darmstadt, Germany) supplemented with 10% (v/v) fetal bovine serum (F0804; Sigma-Aldrich), $100\,\mathrm{units\,mL^{-1}}$ penicillin and $0.1\,\mathrm{g\,L^{-1}}$ streptomycin. The culture flasks were kept in a cell incubator at 37 °C in a water-saturated atmosphere with 5% CO_2. The cells were transferred onto the flat side of Si_3N_4 membranes (frame size 5 mm × 5 mm, window size 1.5 mm × 1.5 mm, membrane thickness 1000 nm; Silson Ltd, Warwickshire, UK) when they reach 80% confluence, by detaching them from the culture flasks using 0.05% (v/v) trypsin (T4799-5G; Sigma-Aldrich) and 0.02% (w/v) EDTA (8040.2; Carl Roth GmbH, Karlsruhe, Germany) in phosphate buffered saline (PBS). The membranes were seeded with an initial concentration of about $3.8 \times 10^8\,\mathrm{cells mL^{-1}}$. After about 24 h, the windows were washed with PBS, fixed [21] for 15 min with 3.7% formaldehyde solution stabilized with 1% methanol (104003; Merck, diluted 1 : 10 in PBS) and then washed three times with PBS. Fixed samples were washed in ultrapure water and plunge-frozen [16, 20–22] by fast immersion in a liquid ethane-propane mixture using an automatic grid plunger (EM GP2; Leica Microsystems GmbH, Wetzlar, Germany). The frozen samples were then lyophilized in a home-built freeze-drier [16, 20–22]. Visible-light phase contrast imaging was carried out before, between and after these steps for quality control.

Scanning SAXS We performed scanning SAXS experiments at the micro-branch (experimental hutch II) of beamline ID13 at the European Synchrotron Radiation Facility (ESRF, Grenoble, France). The beam was pre-focused by parabolic beryllium compound refractive lenses (Be-CRLs) of 200 µm radius at the apex (R_A) and monochromated by a Si-111 channel-cut monochromator to a photon energy of 13.0 keV. The beam was then focused by Be-CRLs with an R_A of 50 µm with 2 µm × 3 µm spot size and a flux of $1.7 \times 10^{12}\,\mathrm{photons\,s^{-1}}$. Close to the sample, the beam was conditioned with a 20 µm aperture and cleaned with an 80 µm guard aperture (pinhole camera). The sample was aligned with an on-axis visible-light microscope. Downstream the sample, a 70 mm helium-filled flight tube was employed to reduce air scattering. A beam stop right outside the exit window of the flight tube blocked the primary beam, while the scattered radiation was recorded by an Eiger X 4M detector (2070 rows × 2167 columns *i. e.* ≈ 4 megapixels, pixel size 75 µm × 75 µm; Dectris, Baden, Switzerland), located about 0.9 m away from the sample. A fast scanning mode [27] was achieved by continuously moving the sample at constant speed during data acquisition.

We used the fast scanning mode on the freeze-dried NIH-3T3 fibroblasts grown on Si_3N_4 windows. Each window contained about 800 cells on a 1.5 mm × 1.5 mm area. Scans of a window were obtained by moving the window horizontally (2974 positions) and vertically (2991 positions) through the X-ray beam (Fig. 3.1) in steps of 0.5 µm. These window-wide scans were performed using the minimum exposure time allowed by the detector, *i. e.* 1.34 ms per scan position. This way, each scan consisted of 8 895 234 scattering patterns in total, acquired in about 7 hours (25 602 s, including about 1.54 ms overhead per scan position). For comparison, we also performed scans of smaller regions containing single cells with longer exposure times (20 ms per scan position), comparable to cell scans performed in the past [17, 18, 21]. For both short and long exposure time scans, the step size was 0.5 µm × 0.5 µm. The radiation dose D can be estimated as shown by Weinhausen et al. [16] and Hémonnot et al. [21] following Howells et al. [30], who approximate the cellular material with an 'average protein' of empirical formula

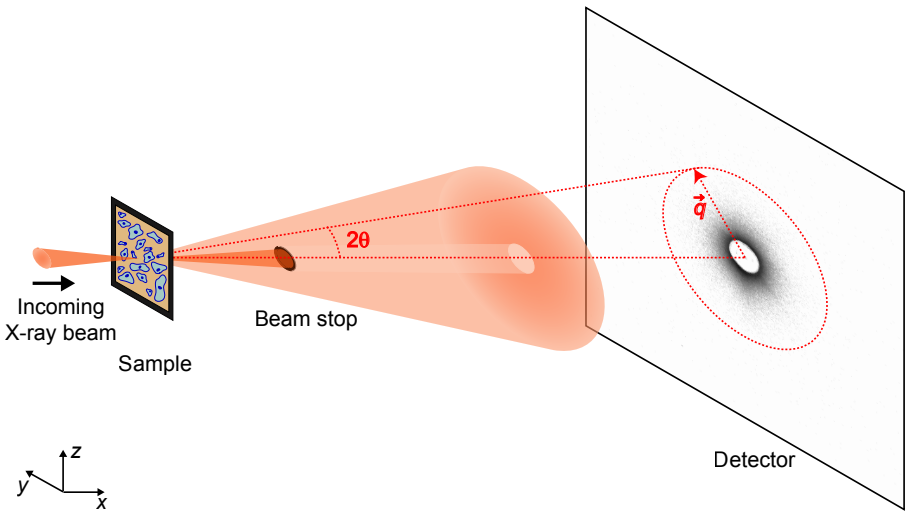

Figure 3.1: Experimental setup. A Si_3N_4 membrane with freeze-dried cells is moved along the y- and z-axes through the X-ray beam to obtain a raster scan. The undiffracted beam is blocked by the beam stop; the scattered X-rays are collected by the detector. The red dashed lines illustrate the relationship between the scattering angle 2θ and the direction of the corresponding scattering vector $\vec{q}$.

$H_{50}C_{30}N_9O_{10}S$. Accordingly, we use the equation

$$D = \frac{\mu/\rho_m I_0 h\nu T}{\Delta y \Delta z},$$

where $\mu/\rho_m = 2.55\,\mathrm{cm}^2/\mathrm{g}$ is the ratio between mass attenuation coefficient and mass density of the cellular material [31], I_0 is the photon flux, $h\nu$ is the photon energy, T is the exposure time per scan point and Δy and Δz are the step sizes of the scan in the horizontal and vertical direction, respectively. The resulting doses were 4.8×10^6 Gy for $T = 1.34\,\mathrm{ms}$ and 7.2×10^7 Gy for $T = 20\,\mathrm{ms}$.

Data analysis For each scan, a dark-field contrast image [15–17, 20, 21] of the scanned region was obtained by integrating the 2D scattering patterns within a region of interest on the detector corresponding to a maximum q value of $2.99\,\mathrm{nm}^{-1}$ and by plotting the resulting intensity values in a color-coded fashion at the corresponding scan positions. q is the magnitude of the scattering vector $\vec{q}$,

$$q = \frac{4\pi}{\lambda} \sin\theta, \tag{3.1}$$

where λ is the wavelength of the incoming X-rays and θ is half the scattering angle (see Fig. 3.1).

In order to define ROIs for our large datasets, we segmented the corresponding dark-field contrast image, where we could distinguish the cells from the background and the nuclei from the cytoplasm, as exemplified in Fig. 3.2a, b. The large number of cells grown on one window renders manual ROI selection unreasonable. Therefore, we used a semi-automated segmentation procedure detailed in the supporting information. In brief, we use local intensity thresholds [32] to separate the cells from the background (Fig. 3.2c) and a different Otsu threshold [33] for each cell to find the nuclei (Fig. 3.2d). The final ROIs are shown in Fig. 3.2e for the portion of the dark-field contrast image in the white box in Fig. 3.2a and in Fig. 3.4a for the complete frame.

One-dimensional radial intensity profiles $I(q)$ were obtained from the 2D scattering patterns by azimuthal integration [15–17, 20, 21] in the same q range as used for the dark-field

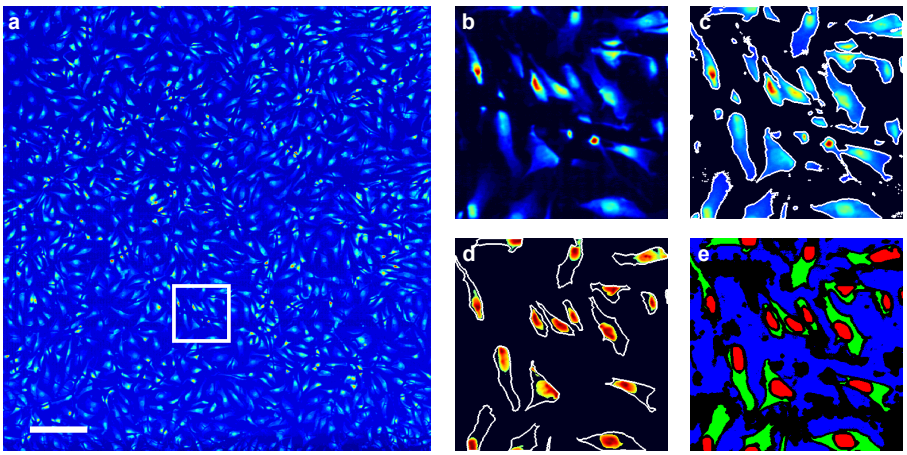

Figure 3.2: Dark-field contrast image segmentation. a) X-ray dark-field contrast image for the complete scan of the entire window. Scale bar: 200 µm. b) Detail of the region inside the white box in a. c) Result of local thresholding, showing the same region as in b, but the pixels identified as background have been masked out. The contours of the mask are shown in white. d) Result of global thresholding on single cells, showing the same region as in b, but only the nuclei. The contours of the cell bodies are shown in white. e) Final regions of interest for the region shown in b. Background is shown in blue, cytoplasm in green and nuclei in red. Black pixels are disregarded. The color scales have been readjusted individually in a-d for better visualization.

contrast image computation and are represented as a function of the scattering vector magnitude q (equation (3.1)). The radial intensity profiles were then normalized by the exposure time and the background intensity was subtracted from the nuclear and cytoplasmic intensities. The background-corrected radial intensity curves were fitted by a non-linear least-squares minimization to a power law in the q range $[0.185, 1.723]\,\mathrm{nm}^{-1}$, corresponding to real-space features between 3.6 nm and 34.0 nm.

All data analysis was carried out using self written MATLAB R2017b (The MathWorks, Inc., Natick, MA, USA) scripts, including the Image Processing Toolbox and functions from the Nanodiffraction toolbox developed by Nicolas et al. [27].

Results and discussion

Analysis of cell populations, single cells and subcellular positions The segmentation of the dark-field contrast image described above is used to compute the average scattering pattern for each ROI (Fig. 3.3a, b and c). Each ROI consists of a large number of scattering patterns – 3 610 683 for the background, 700 766 for the cytoplasm and 419 836 for the nuclei – and possible anisotropies due to local orientations are not visible in these average scattering patterns. Indeed, all anisotropies stem from the background scattering pattern, as confirmed by background scattering pattern subtraction (see the supporting information). Thus, the isotropy of the averaged patterns justifies the computation of one-dimensional radial intensity profiles through azimuthal integration of the two-dimensional scattering patterns. The resulting intensity values I are plotted in Fig. 3.3d against q (see equation (3.1)). The background radial intensity profile (blue curve in Fig. 3.3d) is then subtracted from the two curves containing the actual signal (red and green curves in Fig. 3.3d) to obtain the background-corrected radial intensity profiles shown in Fig. 3.3e. These profiles follow a power law decay,

$$I(q) = Kq^{\alpha} + B. \tag{3.2}$$

The additive constant B accounts for small density fluctuations in the sample, inelastic and incoherent scattering [10, 34]. The exponent α is related to the morphology of the sample.

For instance, monodisperse rods would lead to $\alpha = -1$, monodisperse platelets to $\alpha = -2$ and monodisperse spheres to $\alpha = -4$ [35, 36]. Non-integer exponents can be caused by polydisperse and/or fractal scatterers [37–39]. In particular, fractals are characterized by $\alpha > -4$ and values < -4 indicate polydispersity and heterogeneity. In the latter case, predictions on the precise value of α can only be made if a model for the electron density distribution is assumed. When $\alpha = -4$ at large q values, equation (3.2) is Porod's law [35, 36]. In this case, Porod's constant K depends on the electron density of the sample and the surface area of the interface between scatterers and air [35, 36].

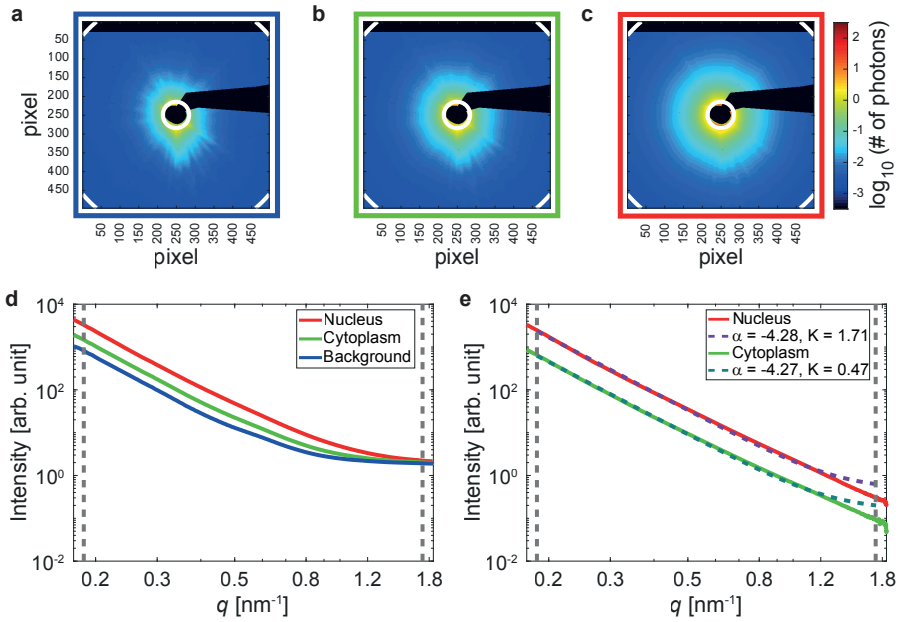

Figure 3.3: Data reduction and fitting. a) Average scattering pattern for the background region. b) Average scattering pattern for the cytoplasmic region. c) Average scattering pattern for the nuclear region. The white lines in a-c delimit the fitting range (see e). d) Radial intensity profiles for the background, cytoplasmic and nuclear regions, respectively obtained by azimuthal integration of the average scattering pattern shown in a, b, c. The vertical dashed lines delimit the fitting range (see e). e) Radial intensity profiles for the cytoplasmic and nuclear regions after background subtraction, fitted with equation (3.2). The vertical dashed lines delimit the fitting range.

The same analysis can be repeated on ensembles of scattering patterns, allowing us to compare different cells, or groups of cells. By accessing one cell at a time, we can compute background, cytoplasmic and nuclear average scattering patterns for each cell. For example, for the ROIs shown in Fig. 3.4c, we obtain the radial intensities shown in Fig. 3.4e (teal curve for the cytoplasm, orange curve for the nucleus). These curves are very similar to those obtained from averaging over the entire window (ROIs shown in Fig. 3.4a), also plotted in Fig. 3.4e for comparison (light green curve for the cytoplasm, red curve for the nucleus). The main difference is that the single cell curves are slightly noisier for high q values, which is not surprising since they were obtained by averaging a much smaller number of scattering patterns, *i.e.* 1373 instead of 700 766 for the cytoplasm and 461 instead of 419 836 for the nucleus. It is now possible to select a subpopulation of cells, for instance imposing conditions on the cell size. An example is shown in Fig. 3.4b, where only the ROIs belonging to the cells satisfying $N_{\text{nuc}} \geq 30$, $N_{\text{nuc}} \leq N_{\text{cyt}} \leq 5000$ and $N_{\text{cyt}} < N_{\text{bkg}} \leq 10000$ are shown (N_{nuc}, N_{cyt} and N_{bkg} are the numbers of pixels included in the nuclear, cytoplasmic and background region, respectively). We empirically set these conditions to reduce the number of connected components that are fragments of cells instead of whole cells, while retaining a statistically significant number of

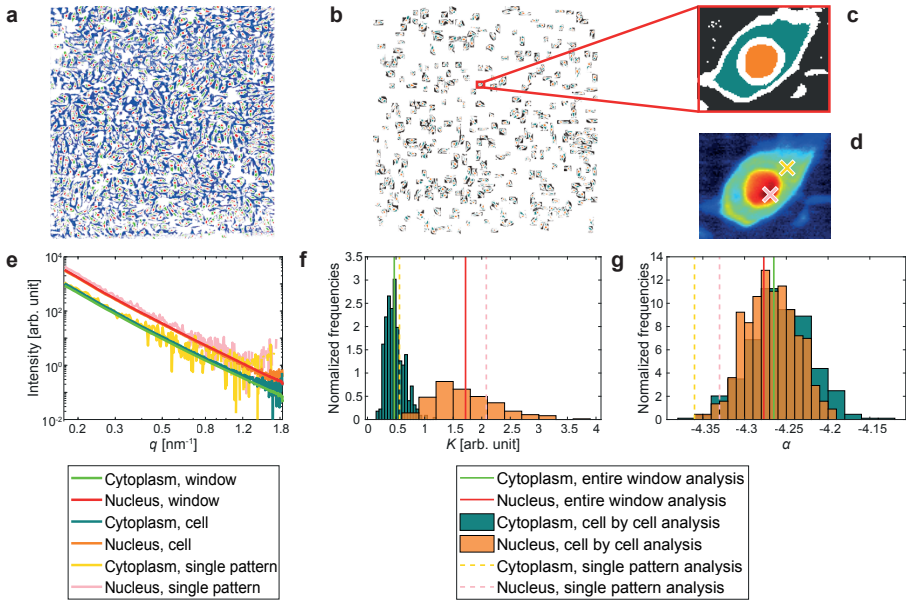

Figure 3.4: Analysis of different data ensembles. a) ROIs, entire window analysis. Background is shown in blue, cytoplasm in green and nuclei in red. b) ROIs, cell-by-cell analysis. Background is shown in black, cytoplasm in teal and nucleus in orange. c) Enlargement of the region in the red box in b: example of ROIs for one cell. d) Dark-field contrast image for the cell shown in c. The positions of the scattering patterns used to exemplify single scattering pattern analysis (see e, f, g) are marked by crosses in yellow for the cytoplasm and pink for the nucleus. e) Radial intensity profiles for the cytoplasmic and nuclear regions, after background subtraction. The curves were obtained by azimuthal integration of average scattering patterns coming from different ensembles: averaged over the entire window (ROIs shown in a), averaged over an individual cell (ROIs shown in c) or single (not averaged) scattering patterns (marked in d). f) Distribution of K values obtained from the cell subset shown in b. The values obtained from the entire window analysis and from the single scattering pattern analysis are also shown. g) Distribution of α values obtained from the cell subset shown in b. The values obtained from the entire window analysis and from the single scattering pattern analysis are also shown. For each bin in f and g, the frequencies are obtained by dividing the counts by the total number of values and then normalized by dividing them by the width of the bin.

cells. For further details, see the supporting information. K and α are analyzed with respect to this subpopulation by computing the average nuclear, cytoplasmic and background scattering patterns for each of the cells shown in Fig. 3.4b, by plotting the corresponding radial intensities and fitting them with equation (3.2). The result is a set of fit parameters, in particular K and α, for each of the 444 analyzed cells. The corresponding distributions are shown in Fig. 3.4f and g. For comparison, the K and α values obtained for the entire window are depicted as vertical solid lines. These values are close to the average values of the corresponding distributions (see also the supporting information, Table S2), suggesting that the subpopulation used here is representative of the total population. The highly overlapping distributions of α for nuclei (orange) and cytoplasm (teal; Fig. 3.4g) suggest that all cells have a similar nanostructure, with little difference between nuclear and cytoplasmic regions. Differences between nuclei and cytoplasm emerge in the K distributions (Fig. 3.4f) that have large standard deviations (as shown in Table S2 in the supporting information), reflecting the high variability occurring even among the same cell line.

The radial intensities can also be evaluated for each scan point within the cell body separately, *i.e.* without any averaging, so that the local variability is accessed. In this case, the assumption of isotropic scattering patterns is valid in first approximation only. An example is

shown for just two positions, indicated in Fig. 3.4d by a yellow cross (cytoplasm) and a pink cross (nucleus). The background is computed by averaging those background scattering patterns belonging to the surroundings of this cell (black pixels in Fig. 3.4c) that are on the same row as the cytoplasmic or nuclear scattering pattern considered. Due to the considerable length of one row, scattering patterns in different rows are acquired at very distant time points and, as the incoming beam intensity can fluctuate in time, using only background scattering patterns acquired very soon before or after the considered scattering pattern ensures that the incident X-ray intensity levels are not significantly different for the considered scattering pattern and its background. The resulting background-subtracted radial intensities, shown in Fig. 3.4e, follow the curves for the whole window well, but are visibly noisier than the others. Moreover, they show an increase at large q values, which is actually an artifact of the azimuthal integration procedure for low intensity values (see the supporting information). However, the fits of these lower-quality data with a power law are still possible, and the resulting K and α values (vertical dashed lines in Fig. 3.4f and g) fall within the boundaries of the distributions obtained for the single cell averages.

Validity of data from short exposure times The fits of the comparatively noisy individual radial intensity profiles shown in Fig. 3.4e yield results in good agreement with those obtained from averages over whole cells (see Fig. 3.4f, g), suggesting that even these low-intensity, non-averaged single scattering patterns contain valuable information that can be analyzed. The analysis of non-averaged scattering patterns from scanning SAXS has already been successfully applied not only on strongly scattering materials such as bone [8, 9, 11] [10], wood [8] [12] or teeth [13] [14], but also on weakly scattering samples, such as biological cells [16–18, 21, 22]. However, in all previous examples, the exposure times ranged from 30 ms to 10 s per scan point, with typical doses [16, 22, 30] on the order of 10^7 Gy–10^8 Gy, thus being considerably longer and more invasive than here (1.34 ms, corresponding to a dose of 4.8×10^6 Gy), and therefore preventing the recording of large data sets. The scattering patterns obtained with longer exposure times do not necessarily yield more information than those from shorter exposure times, as radiation damage plays an increasingly more important role when more dose is imposed on the sample [40–42].

We compare the results obtained from a specific region in our full window fast scans to slower scans of the identical cells, using the same step size but a different exposure time, *i.e.* 20 ms per scan point, corresponding to a dose of 7.2×10^7 Gy, added to the dose from the previous exposure, thus 7.68×10^7 Gy. This exposure time is chosen to maximize the signal-to-noise ratio (SNR) of the dark-field contrast image (for more details, see the supporting information). Fig. 3.5a shows a portion of the dark-field contrast image from Fig. 3.2a, while Fig. 3.5b shows the dark-field contrast image for a scan, carried out later, on the same region, with 20 ms exposure time. Despite the intensities being normalized with respect to the different exposure times, the two images are not identical: the background appears brighter for the longer exposure time. This might be due to a change in the cell-to-substrate contrast caused by radiation damage, to artifacts introduced by the detector, to intensity fluctuations of the incoming X-ray beam, to undetected defective detector pixels randomly switching on and off, or to a combination of the factors above.

A single scattering pattern analysis is performed on the two central cells of the region, with the procedure described above, yielding the K and α maps in Fig. 3.5c, d, f, g. The K maps look very similar to each other, although the one for the shorter exposure time (Fig. 3.5c) appears more pixelated. Their similarity is supported by the strong agreement of the distributions of K for cytoplasmic and nuclear regions as shown in Fig. 3.5e. The two distributions also have similar, although not identical, medians, standard deviations and averages, as reported in Table S3. The distributions of α resemble each other as well (Fig. 3.5h) and their ranges

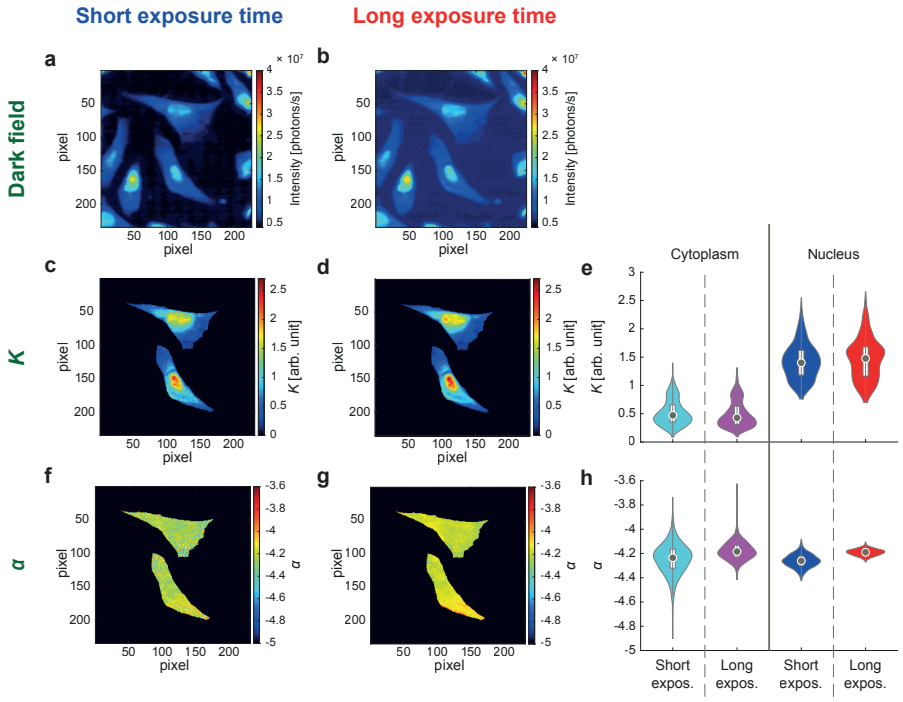

Figure 3.5: Comparison of fast and slow scans. a) Dark-field contrast image of one particular region from a fast scan (exposure time: 1.34 ms). b) Dark-field contrast image of the same region from a slow scan (exposure time: 20 ms). c) Map of K values, fast scan and d) slow scan. e) Violin plots of the K values shown in c, d. f) Map of α values, fast scan and g) slow scan. h) Violin plots of the α values shown in f, g. In the violin plots [43, 44] in e and h, the gray circles mark the median value and the white boxes represent the interquartile range.

strongly overlap, although the cytoplasmic distributions differ in their extreme values and the nuclear distribution for the long exposure time is shifted to larger values with respect to the distribution for the short exposure time. Of note, the α maps (Fig. 3.5f, g) are fairly homogeneous, indicating a similar local morphology throughout the cell, in agreement with previous work [21]. In fact, all four distributions shown in Fig. 3.5h have similar medians and averages, as can be seen in Table S3. At a closer look, these values are more similar within the same scan (*i.e.* between the different cellular regions) than within the same cellular region (*i.e.* nucleus or cytoplasm) in different scans. This suggests that α is determined by the exposure time rather than by the point in the cell that the signal originated from. Indeed, a previous study on the same cell line [21] suggests that evident differences among α values are related to different severity of radiation damage. The authors show that freeze-dried samples lead to $\alpha \approx -3.6$, freeze-dried samples scanned with an attenuated beam intensity to $\alpha \approx -4$ and cryoprotected freeze-dried samples to $\alpha \approx -4.3$. Moreover, the sample preparation seems to influence the power law exponent values, as found for SK8/18-2 cells [17] and for *Dictyostelium discoideum* [20]. Regardless of the cell type, living cells have larger exponents than chemically fixed cells, which in turn have larger exponents than frozen-hydrated cells, and freeze-dried cells yield the smallest exponents. It is possible that the low variation we observe for α throughout a cell is due to the freeze-drying procedure we apply. The aforementioned study of SK8/18-2 cells reports a larger difference between the average nuclear and cytoplasm exponents, for both living and hydrated cells, than what we measure here. However, it should be kept in mind that in this work we are dealing with a different cell line and with a single scattering pattern analysis rather than an average scattering pattern analysis.

In addition to radial intensity profiles the analysis of orientation and anisotropy of scattering patterns has recently been used on biological tissues and cells to obtain orientation maps for *Dictyostelium discoideum* [20], several types of human and murine cells [22], cardiomyocytes [45] and cardiac tissue [27]. We perform an analysis of orientation and anisotropy for the scattering patterns of the fast and slow scans shown in Fig. 3.5, following Bernhardt et al. [22] and Nicolas et al. [27], as explained in the supporting information, including Fig. S5. We find that, regardless of the exposure time and of the examined cell, a predominant orientation of about 21° emerges. This is an indication that the signal form the sample is not strong enough to allow for this kind of analysis. Indeed, orientations significantly different from 21° are only visible in some parts of the nuclei, where the signal is stronger, *i.e.* more scatterers are present in the beam, as the nucleus is thicker and denser than the cytoplasm. Analysis of orientation and anisotropy will strongly benefit from new-generation synchrotrons such as the current ESRF-EBS upgrade, as a higher brilliance will compensate for the faintness of cellular signals.

Dependence of the fit parameters on the cell size The possibility to analyze one cell at a time allows us to compare various properties of a large number of cells. As an example, we show (Fig. 3.6) the dependence of K and α on the cell area, for the subpopulation shown in Fig. 3.4b. For each cell, the cell area is quantified by counting the pixels belonging to the given cell, according to the cell body mask discussed above. Although there is no perfect anticorrelation, K evidently tends to decrease with increasing cell area (Fig. 3.6a). This is true for both the nucleus and the cytoplasm. Conversely, no dependence of α on the cell area emerges in Fig. 3.6c.

The cell size is related to the phase of the cell cycle [46]: the cellular volume grows during gap 1 (G1) phase; the DNA is duplicated during synthesis (S) phase; the cellular volume grows again during gap 2 (G2) phase, then the cell divides (mitosis, M, and cytokinesis) into two "daughter" cells that usually enter their own G1 phase [47]. These volume changes appear in our two-dimensional dark-field contrast image of adherent cells (Fig. 3.2a) as changes in the

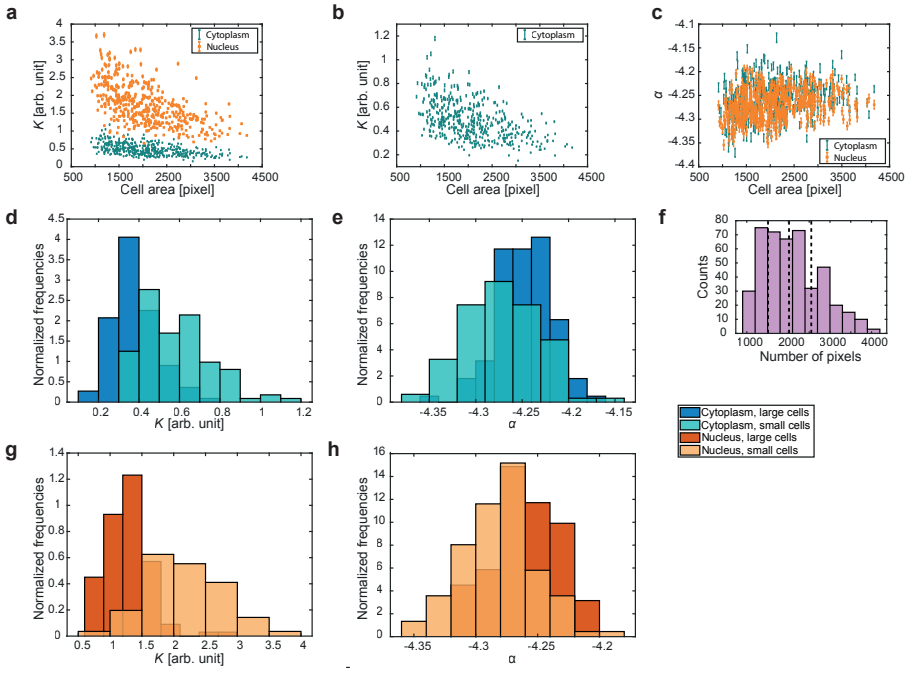

Figure 3.6: Dependence of K and α on the cell area for a subpopulation of cells. a) Dependence of K and c) α from the cell-by-cell analysis (see Fig. 3.4) on the cell size. b) Same as a, rescaled for the cytoplasm. d) Distributions of the K and e) α values for the cytoplasmic regions, for the cells in the first (light blue) and fourth (dark blue) area quartile. f) Distribution of the cell areas for the subpopulation. The vertical dashed lines (corresponding to 1510 pixels, 2015 pixels and 2550 pixels) delimit the quartiles of the area distribution. g) Distributions of the K and h) α values for the nuclear regions, for the cells in the first (pale orange) and fourth (dark orange) area quartile. For each bin in d, e, g and h, the frequencies are obtained by dividing the counts by the total number of values and then normalized by dividing them by the width of the bin.

cell (projected) area. Since there is no one-to-one correspondence between cell size and phase of the cell cycle [46], it is not possible to tell the exact point of the cell cycle for a cell looking at its area only; nevertheless, among the smaller cells there is a higher incidence of cells in the G1/S phase, and among the bigger cells there is a higher incidence of cells in the G2/M phase [21]. Therefore, we expect the cells in the first quartile of the area distribution (see Fig. 3.6f) to be mostly in the G1/S phase and the cells in the fourth quartile to be mostly in the G2/M phase. For the sake of simplicity, in the following we refer to the cells in the first quartile of the area distribution as 'small' cells and to those in the fourth quartile as 'large' cells.

The distributions of α for small and large cells are globally different, as the two-sample Kolmogorov-Smirnov test [48] yields a p-value of 9.23×10^{-8} for the cytoplasmic distributions and of 4.60×10^{-8} for the nuclear distributions. Both values are well below the commonly used 0.05 p-value threshold. However, only a very small shift to larger values is observed for the large cells, both for the cytoplasm (Fig. 3.6e) and for the nucleus (Fig. 3.6h). The average values of these distributions are equal within experimental error (see also Table S4 in the supporting information). As already discussed, the exponent α is determined by the morphology of the sample. In the present case, the exponents are quite close to -4, which is the exponent associated with identical three-dimensional scatterers with well defined boundaries [34–37]. However, all exponents we find are slightly but systematically smaller than -4, thus hinting to three-dimensional, heterogeneous scatterers, possibly having diffuse boundaries. Additional information is provided by K, that displays a much more evident difference in the distributions for small and large cells, both for the cytoplasm (Fig. 3.6d) and for the nucleus (Fig. 3.6g). The distributions for the small cells are wider, *i. e.*, they have larger standard deviations (see also Table S4 in the supporting information) and are centered on larger values. The difference between the average values is evident (as can be seen in the supporting information, Table S4), and the two-sample Kolmogorov-Smirnov test produces extremely low values (1.16×10^{-15} for the cytoplasmic K distributions and 5.52×10^{-26} for the nuclear K distributions). This suggests a decrease of K from the earlier to the later phases of the cell cycle. When $\alpha = -4$ and the scatterers have a uniform electron density, K coincides with Porod's constant, which is proportional to the square of the electron density contrast $\Delta\rho$ and to the surface area S of the interface between scatterers and air [35, 36]:

$$K \propto S(\Delta\rho)^2. \tag{3.3}$$

Assuming this holds for our data in first approximation, it follows that, during the cell cycle, there is a decrease in $\Delta\rho$, or in S, or both. As we perform our measurements in air, changes in the electron density contrast $\Delta\rho$ are equivalent to changes in the electron density of the scatterers, which, in turn, is directly proportional to the mass density of the scatterers. We speculate that a decrease in mass density could be caused by a rearrangement of proteins that are expressed anew during the growth phases of the cell cycle into their final conformation. A decrease of S is supposedly due to scatterers being packed in a different manner, and thus with a smaller exposed surface, in later phases of the cell cycle compared with the earlier phases.

Conclusions

We demonstrate that fast scanning SAXS experiments on a large number of mammalian cells are possible, thanks to the synchronization of the continuous movement of the sample stage with the data acquisition [27]. This approach brings scanning SAXS to an entirely new level as it is now possible to acquire and analyze data from reasonably large populations of cells so as to draw statistically valid conclusions, despite cell-to-cell variability. The requirement for high resolution is fulfilled as each individual scattering pattern is determined by all structures within the illuminated area and we detect typical dimensions between 3.6 nm and 34.0 nm. At the same

time, we achieve high throughput, as we examine roughly 800 cells, storing 8 895 234 scattering patterns in about 7 h. Furthermore, the vast amount of data provided by one acquisition can be dealt with thanks to the semi-automated segmentation of the corresponding dark-field contrast image.

Such segmentation enables three different kinds of analysis. First, the properties of the nuclear and cytoplasmic ROIs are analyzed as averages over the entire scanned area, thus characterizing the entire cell population. Second, a single cell is characterized *globally*: the nuclear and cytoplasmic scattering patterns belonging to the same cell are averaged, providing information about the 'overall properties' of that specific cell. To exemplify a statistically relevant analysis of a cell subpopulation, we examine the dependence of quantitative structural parameters (K and α) on the cell size. Assuming the cell size to be indicative of the cell cycle phase, we find a decrease of K as the cell cycle proceeds from earlier phases (small cells) to later phases (large cells) of the cell cycle, thus supporting previous results [21] with data from many more cells, that is, 444 instead of 16. Third, a single scattering pattern analysis characterizes single cells *locally*: the scattering patterns are not averaged, so that the pseudo-resolution provided by the step size of the scan, 0.5 µm × 0.5 µm, is not lost.

The exposure time for a single scattering pattern is comparatively low (1.34 ms); however, this does not significantly impair the results of the power law fits with respect to those obtained using a longer exposure time, as shown by the comparison with a 20 ms exposure time scan, similar to what has been successfully used for cell scans in the past [17, 18, 21]. Importantly, while the radiation dose of the slower scans is comparable with values [7] typical of scanning SAXS, *i. e.* about 10^7 Gy–10^8 Gy, with our method the dose is considerably lowered, $\approx 10^6$ Gy, comparable with ptychography. Overall, our approach lends itself to a variety of applications in the studies of subcellular structures and can be used as a high-throughput, label-free complementary method for other popular techniques such as fluorescence or electron microscopy.

Acknowledgements. The authors thank J.-D. Nicolas and T. Salditt for providing the Nanodiffraction toolbox and for fruitful discussions on data analysis. The experiments were performed on the ID13 beamline at the European Synchrotron Radiation Facility (ESRF), Grenoble, France.

Funding information. This work was financially supported by the German Research Foundation (DFG) in the framework of SFB 755, "Nanoscale Photonic Imaging", projects C10 and B07 and SFB 860 "Integrative Structural Biology of Dynamic Macromolecular Complexes", project B10; by the Cluster of Excellence and DFG Research Center "Nanoscale Microscopy and Molecular Physiology of the Brain" (CNMPB); and under Germany's Excellence Strategy - EXC 2067/1- 390729940. Furthermore, funding was granted by the German Ministry of Education and Research (BMBF) under grants no. 05K16MG2 and 05K19MG3.

References

[1] Abraham J Koster and Judith Klumperman. "Electron Microscopy in Cell Biology: Integrating Structure and Function". In: *Nat. Rev. Mol. Cell Biol.* 4.9; SUPP (2003), SS6–SS9. DOI: 10.1038/nrm1194.

[2] N. de Jonge et al. "Electron Microscopy of Whole Cells in Liquid with Nanometer Resolution". In: *Proc. Natl. Acad. Sci. U. S. A.* 106.7 (2009), pp. 2159–2164. DOI: 10.1073/pnas.0809567106.

[3] S. W. Hell. "Far-Field Optical Nanoscopy". In: *Science* 316.5828 (2007), pp. 1153–1158. DOI: 10.1126/science.1137395.

[4] Marta Fernández-Suárez and Alice Y. Ting. "Fluorescent Probes for Super-Resolution Imaging in Living Cells". In: *Nat. Rev. Mol. Cell Biol.* 9.12 (2008), pp. 929–943. DOI: 10.1038/nrm2531.

[5] Bo Huang, Hazen Babcock, and Xiaowei Zhuang. "Breaking the Diffraction Barrier: Super-Resolution Imaging of Cells". In: *Cell* 143.7 (2010), pp. 1047–1058. DOI: 10.1016/j.cell.2010.12.002.

[6] Janos Kirz, Chris Jacobsen, and Malcolm Howells. "Soft X-Ray Microscopes and Their Biological Applications". In: *Q. Rev. Biophys.* 28.01 (1995), p. 33. DOI: 10.1017/s0033583500003139.

[7] Clément Y. J. Hémonnot and Sarah Köster. "Imaging of Biological Materials and Cells by X-Ray Scattering and Diffraction". In: *ACS Nano* 11.9 (2017), pp. 8542–8559. DOI: 10.1021/acsnano.7b03447.

[8] P. Fratzl et al. "Position-Resolved Small-Angle X-Ray Scattering of Complex Biological Materials". In: *J. Appl. Crystallogr.* 30.5 (1997), pp. 765–769. DOI: 10.1107/s0021889897001775.

[9] Mathias Hauge Bünger et al. "Nanostructure of the neurocentral growth plate: Insight from scanning small angle X-ray scattering, atomic force microscopy and scanning electron microscopy". In: *Bone* 39.3 (2006), pp. 530–541. DOI: 10.1016/j.bone.2006.03.013.

[10] Aurélien Gourrier et al. "Scanning Small-Angle X-Ray Scattering Analysis of the Size and Organization of the Mineral Nanoparticles in Fluorotic Bone Using a Stack of Cards Model". In: *J. Appl. Crystallogr.* 43.6 (2010), pp. 1385–1392. DOI: 10.1107/s0021889810035090.

[11] Mikael J. Turunen et al. "Evaluation of composition and mineral structure of callus tissue in rat femoral fracture". In: *J. Biomed. Opt.* 19.2 (2014), p. 025003. DOI: 10.1117/1.jbo.19.2.025003.

[12] H. Lichtenegger et al. "Variation of Cellulose Microfibril Angles in Softwoods and Hardwoods—A Possible Strategy of Mechanical Optimization". In: *J. Struct. Biol.* 128.3 (1999), pp. 257–269. DOI: 10.1006/jsbi.1999.4194.

[13] J.H. Kinney et al. "Collagen Orientation and Crystallite Size in Human Dentin: A Small Angle X-ray Scattering Study". In: *Calcif. Tissue Int.* 69.1 (2001), pp. 31–37. DOI: 10.1007/s00223-001-0006-5.

[14] Sebastian Gaiser et al. "Understanding Nano-Anatomy of Healthy and Carious Human Teeth: a Prerequisite for Nanodentistry". In: *Biointerphases* 7.1 (2012), p. 4. DOI: 10.1007/s13758-011-0004-8.

[15] O Bunk et al. "Multimodal x-ray scatter imaging". In: *New J. Phys.* 11.12 (2009), p. 123016. DOI: 10.1088/1367-2630/11/12/123016.

[16] Britta Weinhausen et al. "X-ray nano-diffraction on cytoskeletal networks". In: *New J. Phys.* 14.8 (2012), p. 085013. DOI: 10.1088/1367-2630/14/8/085013.

[17] Britta Weinhausen et al. "Scanning X-Ray Nanodiffraction on Living Eukaryotic Cells in Microfluidic Environments". In: *Phys. Rev. Lett.* 112.8 (2014), p. 088102. DOI: 10.1103/physrevlett.112.088102.

[18] Clément Y. J. Hémonnot et al. "X-rays Reveal the Internal Structure of Keratin Bundles in Whole Cells". In: *ACS Nano* 10.3 (2016), pp. 3553–3561. DOI: 10.1021/acsnano.5b07871.

[19] Valeria Piazza et al. “Revealing the Structure of Stereociliary Actin by X-ray Nanoimaging”. In: *ACS Nano* 8.12 (2014), pp. 12228–12237. DOI: 10.1021/nn5041526.

[20] Marius Priebe et al. “Scanning X-Ray Nanodiffraction on Dictyostelium discoideum”. In: *Biophys. J.* 107.11 (2014), pp. 2662–2673. DOI: 10.1016/j.bpj.2014.10.027.

[21] Clément Y. J. Hémonnot et al. “Following DNA Compaction During the Cell Cycle by X-ray Nanodiffraction”. In: *ACS Nano* 10.12 (2016), pp. 10661–10670. DOI: 10.1021/acsnano.6b05034.

[22] Marten Bernhardt et al. “X-Ray Micro- and Nanodiffraction Imaging on Human Mesenchymal Stem Cells and Differentiated Cells”. In: *Biophys. J.* 110.3 (2016), pp. 680–690. DOI: 10.1016/j.bpj.2015.12.017.

[23] L. Pelkmans. “Using Cell-to-Cell Variability–A New Era in Molecular Biology”. In: *Science* 336.6080 (2012), pp. 425–426. DOI: 10.1126/science.1222161.

[24] Kyle M. Douglass et al. “Super-Resolution Imaging of Multiple Cells by Optimized Flat-Field Epi-Illumination”. In: *Nat. Photonics* 10.11 (2016), pp. 705–708. DOI: 10.1038/nphoton.2016.200.

[25] Robin Diekmann et al. “Chip-Based Wide Field-of-View Nanoscopy”. In: *Nat. Photonics* 11.5 (2017), pp. 322–328. DOI: 10.1038/nphoton.2017.55.

[26] A.L. Eberle et al. “High-Resolution, High-Throughput Imaging with a Multibeam Scanning Electron Microscope”. In: *J. Microsc.* 259.2 (2015), pp. 114–120. DOI: 10.1111/jmi.12224.

[27] Jan-David Nicolas et al. “Scanning X-ray diffraction on cardiac tissue: automatized data analysis and processing”. In: *J. Synchrotron Radiat.* 24.6 (2017), pp. 1163–1172. DOI: 10.1107/s1600577517011936.

[28] Anne Beghin et al. “Localization-Based Super-Resolution Imaging Meets High-Content Screening”. In: *Nat. Methods* 14.12 (2017), pp. 1184–1190. DOI: 10.1038/nmeth.4486.

[29] George J. Todaro and Howard Green. “Quantitative studies of the growth of mouse embryo cells in culture and their development into established lines”. In: *J. Cell Biol.* 17.2 (1963), pp. 299–313. DOI: 10.1083/jcb.17.2.299.

[30] M.R. Howells et al. “An assessment of the resolution limitation due to radiation-damage in X-ray diffraction microscopy”. In: *J. Electron Spectrosc. Relat. Phenom.* 170.1-3 (2009), pp. 4–12. DOI: 10.1016/j.elspec.2008.10.008.

[31] MJ Berger et al. “XCOM: Photon Cross Sections Database, NIST Standard Reference Database 8 (XGAM)”. In: *URL http://physics. nist. gov/PhysRefData/Xcom/Text/XCOM.html* (2010).

[32] Derek Bradley and Gerhard Roth. “Adaptive Thresholding Using the Integral Image”. In: *J. Graph. Tools* 12.2 (2007), pp. 13–21. DOI: 10.1080/2151237x.2007.10129236.

[33] Nobuyuki Otsu. “A Threshold Selection Method from Gray-Level Histograms”. In: *IEEE Trans. Syst., Man Cybern.* 9.1 (1979), pp. 62–66. DOI: 10.1109/tsmc.1979.4310076.

[34] W. Ruland. “Small-angle scattering of two-phase systems: determination and significance of systematic deviations from Porod’s law”. In: *J. Appl. Crystallogr.* 4.1 (1971), pp. 70–73. DOI: 10.1107/S0021889871006265.

[35] G. Porod. “Die Röntgenkleinwinkelstreuung von dichtgepackten kolloiden Systemen”. In: *Kolloid-Z.* 124.2 (1951), pp. 83–114. DOI: 10.1007/bf01512792.

[36] André Guinier and Gérard Fournet. *Small-Angle Scattering of X-Rays*. John Wiley & Sons, 1955.

[37] J. T. Koberstein, B. Morra, and R. S. Stein. "The Determination of Diffuse-Boundary Thicknesses of Polymers by Small-Angle X-Ray Scattering". In: *J. Appl. Crystallogr.* 13.1 (1980), pp. 34–45. DOI: 10.1107/s0021889880011478.

[38] P. W. Schmidt. "Interpretation of Small-Angle Scattering Curves Proportional to a Negative Power of the Scattering Vector". In: *J. Appl. Crystallogr.* 15.5 (1982), pp. 567–569. DOI: 10.1107/s002188988201259x.

[39] J. E. Martin and A. J. Hurd. "Scattering from Fractals". In: *J. Appl. Crystallogr.* 20.2 (1987), pp. 61–78. DOI: 10.1107/s0021889887087107.

[40] Emilie Leccia et al. "Hard Alpha-Keratin Degradation Inside a Tissue Under High Flux X-Ray Synchrotron Micro-Beam: A Multi-Scale Time-Resolved Study". In: *J. Struct. Biol.* 170.1 (2010), pp. 69–75. DOI: 10.1016/j.jsb.2009.11.006.

[41] Ewelina Kosior et al. "Study of Radiation Effects on the Cell Structure and Evaluation of the Dose Delivered by X-Ray and α-Particles Microscopy". In: *Appl. Phys. Lett.* 101.26 (2012), p. 263102. DOI: 10.1063/1.4773181.

[42] A. Gianoncelli et al. "Soft X-Ray Microscopy Radiation Damage on Fixed Cells Investigated With Synchrotron Radiation FTIR Microscopy". In: *Sci. Rep.* 5.1 (2015). DOI: 10.1038/srep10250.

[43] Bastian Bechtold. "Violin Plots for Matlab". In: *GitHub repository. URL https://github.com/bastibe/Violinplot-Matlab* (2016).

[44] Jerry L. Hintze and Ray D. Nelson. "Violin Plots: A Box Plot-Density Trace Synergism". In: *Am. Stat.* 52.2 (1998), p. 181. DOI: 10.2307/2685478.

[45] M Bernhardt et al. "Anisotropic x-ray scattering and orientation fields in cardiac tissue cells". In: *New J. Phys.* 19.1 (2017), p. 013012. DOI: 10.1088/1367-2630/19/1/013012.

[46] E.C. Anderson et al. "Cell Growth and Division: IV. Determination of Volume Growth Rate and Division Probability". In: *Biophys. J.* 9.2 (1969), pp. 246–263. DOI: 10.1016/s0006-3495(69)86383-6.

[47] Bruce Alberts et al. *Molecular Biology of the Cell*. 4th ed. New York: Garland Science, 2002.

[48] D. A. Darling. "The Kolmogorov-Smirnov, Cramer-von Mises Tests". In: *Ann. Math. Stat.* 28.4 (1957), pp. 823–838. DOI: 10.1214/aoms/1177706788.

Supporting Information

Detailed segmentation procedure

In the following, the complete procedure employed to obtain the segmentation presented in Fig. 2 in the main text is outlined. The results of the main steps of this procedure are summarized in Fig. S1.

1. **Local thresholding.** We first separate the background from the cells. Since the background is much darker (lower signal, fewer photons) than the cells, which are bright enough to be easily recognized by the human eye, a simple intensity threshold should in first approximation be sufficient. However, the background intensity is not constant

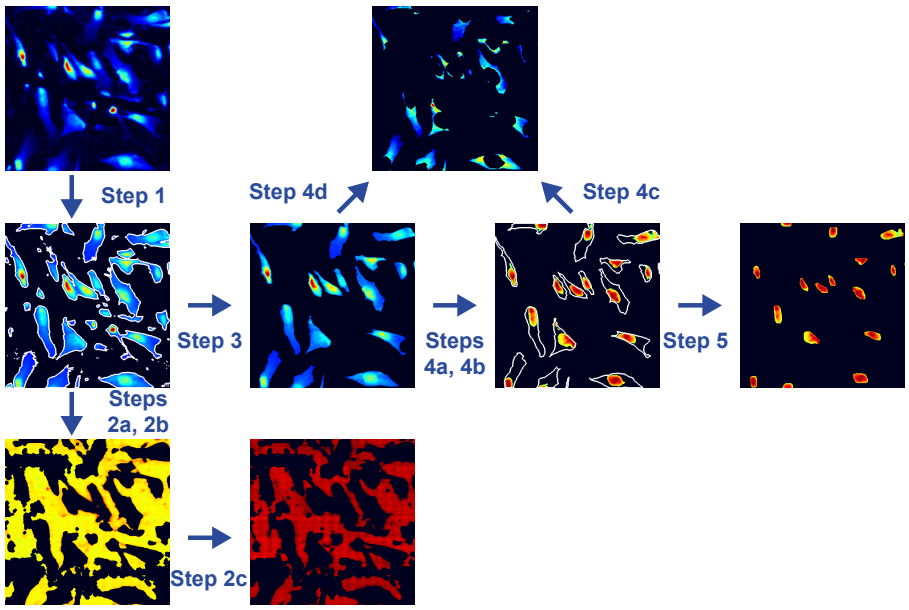

Figure S1: Schematic of the main steps of the segmentation procedure. The effects of the various steps are presented for a portion of the dark-field contrast image shown in Fig. 2a in the main text (the region inside the white box, also shown in Fig. 2b in the main text).

throughout the dark-field contrast image, but varies, particularly along the vertical direction. This is caused by variations in the intensity of the incoming X-ray beam over the full duration of the scan of about 7 hours. Furthermore, there is a rather large variability in the intensity between different cells. As a result, some cells in the lower-intensity regions have parts of the cytoplasm that are roughly as intense as the background of the higher-intensity regions. For this reason, a single intensity value does not work as a threshold. A local thresholding strategy is more suitable. For each pixel of the dark-field contrast image, a local average intensity is computed within a 129 px × 79 px box centered on the considered pixel itself. The pixel is regarded as foreground if its intensity is above the local average, otherwise it is included in the background (Bradley's threshold [1]). The result is a logical mask with '1' at the locations of the foreground pixels and '0' at the positions of the background pixels.

2. **Background definition.** The first step in the background definition is a local thresholding step, where the threshold is 95% of the local average, so that a larger region than what was defined above is considered as foreground. The resulting mask then undergoes:

   (a) *inversion*, to switch from foreground to background;

   (b) *morphological closing* with a 4 px radius, disc-shaped structuring element, so that the contours of the region are smoothed and slightly expanded;

   (c) *intensity selection* on the background region, where only pixels with intensity values within one standard deviation from the average are retained.

3. **Cell bodies definition.** The foreground mask obtained in Step 1 is refined to yield single-cell contours through the following operations:

   (a) *morphological erosion* with a 2 px radius, diamond-shaped structuring element;

   (b) *size selection*, where only connected components containing a number of pixels equal to or greater than 250 are retained;

(c) *manual cleaning*, where connected components are visually checked one by one and their contours are manually modified if necessary. Each of the final connected components must have exactly one nucleus.

4. **Cytoplasm definition.** In order to define the cytoplasmic region in each connected component, the cell bodies region obtained in the previous step undergoes:

   (a) cell by cell *contrast expansion*, where the intensity within each connected component is rescaled so that all available values are used. This step is just performed for better visualization and is not strictly necessary for the rest of the procedure to work;

   (b) cell by cell *global thresholding*, in which a nuclear mask is obtained for each connected component by selecting the pixels more intense than Otsu's threshold [2], calculated for the intensity distribution of the considered connected component.

   After this first raw nuclear region mask is obtained, it is

   (c) *morphologically dilated* with a 4 px radius, diamond-shaped structuring element;

   (d) *subtracted* from the cell bodies region mask. The resulting mask defines the cytoplasmic region.

5. **Nuclei definition.** Finally, the raw nuclear region mask obtained in Step 4b is refined by:

   (a) cell-by-cell *morphological opening* with a disk-shaped structuring element, with a surface area equal to 1/17 of the surface area of each cell's bounding box. This operation smooths the nuclear boundaries so that they assume a more disk-like shape;

   (b) *morphological erosion* with a 1 px radius, diamond-shaped structuring element;

   (c) *real nucleus selection*, where for each cell, only the biggest connected component is considered to be the nucleus, and other connected components in the cell body, if present, are rejected.

Isotropy of the 2D scattering patterns

The isotropy of the average X-ray scattering signal from the cells clearly emerges if we carry out the background subtraction on the two-dimensional scattering patterns (Fig. S2) averaged over the entire window. This shows that the anisotropy visible in Fig. 3a, b and c in the main text are due to the setup only. Contributions may come from optics and collimation upstream of the sample and/or flight tube and beam stop downstream of the sample. The background subtraction step is therefore essential for a correct data analysis. Local anisotropies of the sample are lost in the averaging process, but they can be present in the individual scattering patterns.

Selection of a subpopulation of cells

For the cell by cell analysis presented in the main text, only a subpopulation of the cells detected during image segmentation is considered. This is done mainly to reduce the computation time, but also to reduce the number of cellular fragments in the population. Indeed, our segmentation procedure cannot distinguish between a cell and a fragment of a cell, provided that the fragment is big enough and that it contains part of the nucleus. In our experience, fragmentation of the cells is not uncommon for freeze-dried samples such as ours. As a result, about 23% of the 912

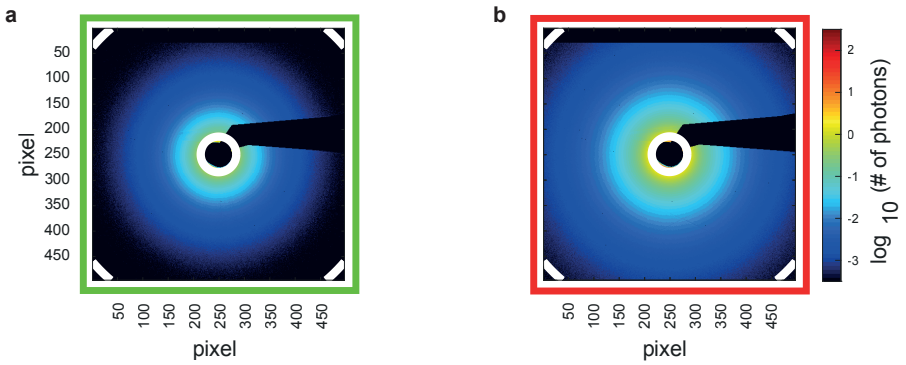

Figure S2: Isotropy of the average scattering patterns. a) Difference between the cytoplasmic average scattering pattern (Fig. 3b in the main text) and the background average scattering pattern (Fig. 3a in the main text). b) Difference between the nuclear average scattering pattern (Fig. 3c in the main text) and the background average scattering pattern (Fig. 3a in the main text). The white lines in a, b delimit the fitting range.

cellular regions identified by our segmentation are really cellular fragments. By selecting only the cellular regions satisfying

- $N_{nuc} \geq 30$;
- $N_{nuc} \leq N_{cyt} \leq 5000$;
- $N_{cyt} < N_{bkg} \leq 10000$,

with N_{nuc}, N_{cyt} and N_{bkg} numbers of pixels included in the nuclear, cytoplasmic and background region of the given cellular region, respectively, we are left with 444 cellular regions, constituting the subpopulation of cells shown in Fig. 4b in the main text, of which only about 6% are fragments.

Artifacts of azimuthal integration

In order to obtain radial intensity profiles from the measured scattering patterns, an azimuthal integration needs to be performed. This means, in practice, that for each q value considered, a corresponding circumference is defined; subsequently, all the photon counts registered along that circumference are summed up; finally, this total number of counts is divided by the number of pixels along the circumference, so that the result is the intensity value $I(q)$ for the specific q value. The pixels corresponding to detector segments or to the beam stop are masked out (black pixels in Fig. S3a). Since these purely geometrical features are always the same throughout the scans (we use the same mask for all scans), for each q value the number of counts along a circumference is always divided by the same number, shown in Fig. S3d. Therefore, if we had only one photon count per q value, we would get just the reciprocal of the points in Fig. S3d, that is, the lowest black line in Fig. S3b, c, e and f. All the intensity values obtained as one count per circumference fall on this line; all the intensity values obtained as two counts per circumference fall on a line obtained multiplying the one-count line by two, and so on. The 15 black lines in Fig. S3b, c, e and f correspond to the values due to 1 to 15 photon counts per circumference. All intensity values lie on one of the lines that are multiples of the one-count line. This "discretization" effect, due to the fact that the possible radial intensity values are ratios of two integer numbers, is less visible for higher intensities, where the black lines would lie closer and closer together. The effect is reduced, or even eliminated, by averaging, as can be clearly seen in the background curves in Fig. S3b and c that are calculated from average scattering patterns. Since these background curves are much smoother because of the averaging,

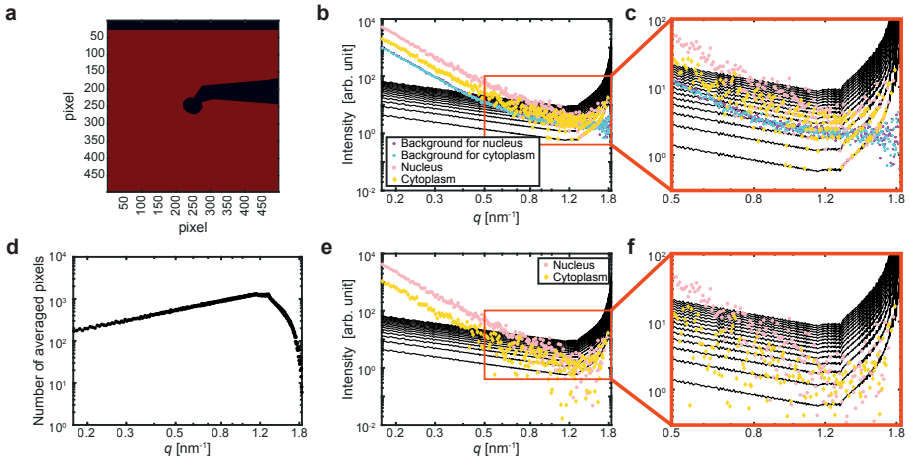

Figure S3: Artifacts due to the azimuthal integration of low-intensity scattering patterns. a) Logical mask defining which detector pixels are taken into account during the azimuthal integration procedure: red pixels are used, black pixels are ignored. b) Radial intensity profiles for the background (cyan for the cytoplasm, purple for the nucleus), for a cytoplasmic (yellow) and for a nuclear (pink) scattering pattern (the same ones as used in Fig. 4 in the main text). c) Enlargement of the region in the red box in b. d) Number of pixels whose value is averaged along a circumference corresponding to q, to obtain the intensity value $I(q)$. e) Background-subtracted radial intensity profiles for a cytoplasmic (yellow) and a nuclear (pink) scattering pattern (the same ones as used in Fig. 4 in the main text). f) Enlargement of the region in the red box in e. The black lines in b, c, e and f represent the intensity profiles we would get if we had only one photon count per q value (lowest line), only two (line just above the lowest) and so on up to 15 counts per q value (highest line). Note that the lowest black line is not exactly the reciprocal of the values in d, because it is normalized by the exposure time in order to match the data (also normalized). The other black lines have been normalized as well.

the background subtraction on the curves shown in Fig. S3b reduces this effect, as can be seen in Fig. S3e and f. However, the curves remain visibly noisy, displaying an increase in their terminal part due to the decrease of pixels associated with high q values (see Fig. S3d) as well as many extremely small intensity values (because the signal and the background differs only slightly) or even missing points (when the signal is lower than the background, the difference is negative, so it can not be shown in a logarithmic plot).

Determination of the optimized exposure time

Four 300 µm × 300 µm scans, each with the same step size (2 µm both horizontally and vertically) but with different exposure times (5 ms, 10 ms, 20 ms and 100 ms per scan point) are carried out in order to determine an optimized "long exposure time", used in the main text for comparison with the shorter exposure time of our window-sized scans (1.34 ms). The corresponding dark-field contrast images are shown in Fig. S4a-d. In order to evaluate the quality of the scans, the signal to noise ratio (SNR) of each dark-field contrast image is computed. The SNR is defined as

$$\mathrm{SNR} = \frac{I_{\mathrm{FRG}} - I_{\mathrm{BKG}}}{\sigma_{\mathrm{BKG}}}, \tag{S4}$$

where I_{FRG} is the average foreground intensity, I_{BKG} is the average background intensity and σ_{BKG} is the standard deviation of the background intensity. The foreground is determined with a local threshold, in analogy to the first step of the segmentation procedure illustrated above; in this case, the local average intensity is calculated within a 35 px × 35 px box. Since only an estimate of the foreground region is needed here, the foreground mask is not further processed;

the results are shown in Fig. S4e-h. All the pixels of the dark-field contrast images that do not belong to the foreground are considered background. According to the resulting SNR values, presented in Table S1, the best (highest) value corresponds to an exposure time of 20 ms.

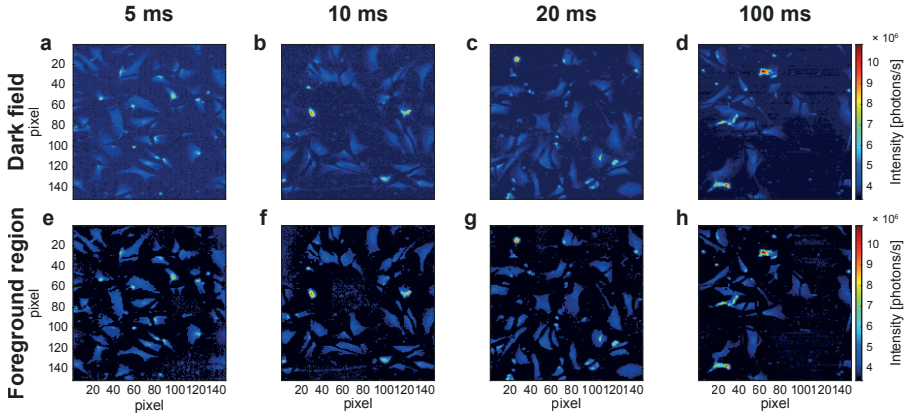

Figure S4: Dark-field contrast images obtained with different exposure times. a-d) Dark-field contrast images for exposure times of 5 ms, 10 ms, 20 ms and 100 ms per scan point, respectively; one pixel corresponds to 2 µm × 2 µm. e-h) Same as a-d, but the background region, obtained by local thresholding, is masked out. All images (a-h) are normalized by the exposure time and depicted on the same color scale.

Table S1: SNR for the dark-field contrast images shown in Fig. S4a-d.

Exposure time [ms]	SNR
5	7.8
10	9.8
20	10.4
100	8.4

Orientation and anisotropy of single scattering patterns

In order to quantify the local anisotropy and orientation of the scanned points of the sample, a principal component analysis (PCA) [3] is performed on individual scattering patterns. The complete PCA procedure is explained in detail in Refs. [4, 5]. Briefly, the covariance matrix of the scattering vector in the detector plane is diagonalized. The eigenvector corresponding to the larger eigenvalue defines the orientation of the scattering pattern. The corresponding orientation in real space is perpendicular to this direction. The anisotropy is defined as the absolute value of the difference between the two eigenvalues, divided by their sum. The PCA is performed in the q range $[0.1744, 0.7664]\,\mathrm{nm}^{-1}$, corresponding to real space features between 8.2 nm and 36.0 nm. The results are shown in Figure S5.

Additional tables

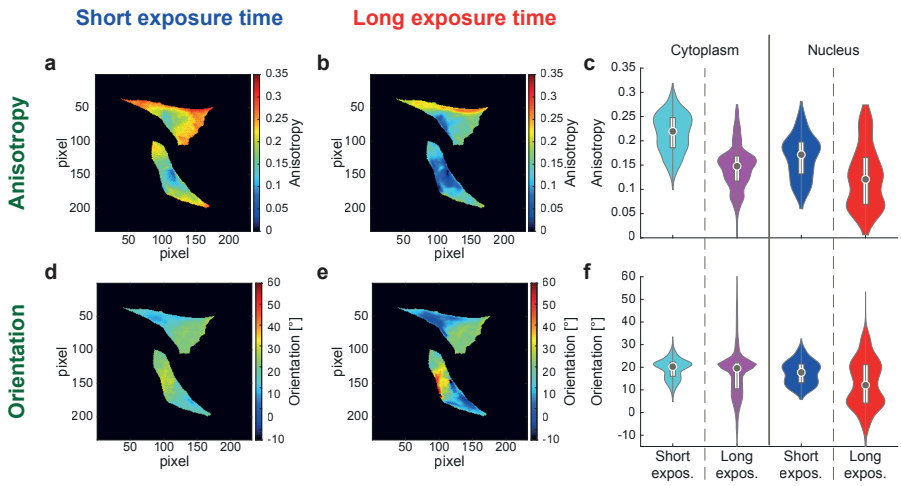

Figure S5: Comparison of anisotropy analysis for the fast and slow scans examined in the main text (Fig. 5). a) Map of anisotropy values, fast scan. b) Map of anisotropy values, slow scan. c) Violin plots of the anisotropy values shown in a, b. d) Map of orientation values, fast scan. e) Map of orientation values, slow scan. f) Violin plots of the orientation values shown in d, e. In the violin plots, the gray circles mark the median value and the white boxes represent the interquartile range.

Table S2: K and α obtained from the different data ensembles illustrated in Fig. 4 in the main text. Note that for the entire window and single scattering pattern analysis, the fit coefficients K and α are given, with the standard error computed from the fit in parentheses. For the cell by cell analysis, instead, the average value for each distribution is given, with the standard deviation of the distribution in parentheses.

	Entire window Fit value (Std. err.)	Cell by cell Average (Std. dev.)	Single scattering pattern Fit value (Std. err.)
K, cytoplasm [arb. unit]	0.468 (0.004)	0.48 (0.16)	0.56 (0.07)
K, nucleus [arb. unit]	1.71 (0.02)	1.7 (0.6)	2.08 (0.11)
α, cytoplasm	−4.265 (0.007)	−4.26 (0.04)	−4.36 (0.10)
α, nucleus	−4.277 (0.009)	−4.27 (0.03)	−4.33 (0.04)

Table S3: Selected statistical descriptors (median, standard deviation, average and standard error of the average) of the distributions shown in Fig. 5e and h in the main text. The cytoplasmic region consists of of 3394 data points, the nuclear region of 1393 data points. Values obtained with the short exposure time (1.34 ms) are shown in blue, values obtained with the long exposure time (20 ms) are shown in red.

	Exposure	Median	Standard deviation	Average (Std. err.)
K, cytoplasm [arb. unit]	short	0.470	0.224	0.519 (0.004)
	long	0.428	0.234	0.493 (0.004)
K, nucleus [arb. unit]	short	1.401	0.320	1.420 (0.009)
	long	1.476	0.366	1.461 (0.010)
α, cytoplasm	short	−4.235	0.129	−4.244 (0.002)
	long	−4.1841	0.0748	−4.1785 (0.0013)
α, nucleus	short	−4.2610	0.0548	−4.2610 (0.0015)
	long	−4.1898	0.0268	−4.1906 (0.0007)

References

[1] Derek Bradley and Gerhard Roth. “Adaptive Thresholding Using the Integral Image”. In: *J. Graph. Tools* 12.2 (2007), pp. 13–21. DOI: 10.1080/2151237x.2007.10129236.

Table S4: Average values of the distributions of K values (Fig. 6d, g in the main text) and of α values (Fig. 6c, h in the main text) for small and large cells. The standard deviation of each distribution is given in parentheses. Note that the standard deviation of the distribution is preferred here to the standard deviation of the mean, in order to highlight the properties of the complete distribution, instead of focusing on the average value only.

	Small cells Average (Std. dev.)	Large cells Average (Std. dev.)
K, cytoplasm [arb. unit]	0.59 (0.17)	0.38 (0.11)
K, nucleus [arb. unit]	2.2 (0.6)	1.3 (0.3)
α, cytoplasm	−4.27 (0.04)	−4.25 (0.03)
α, nucleus	−4.28 (0.03)	−4.26 (0.03)

[2] Nobuyuki Otsu. “A Threshold Selection Method from Gray-Level Histograms”. In: *IEEE Trans. Syst., Man Cybern.* 9.1 (1979), pp. 62–66. DOI: 10.1109/tsmc.1979.4310076.

[3] Karl Pearson. “LIII. On lines and planes of closest fit to systems of points in space”. In: *Philos. Mag.* 2.11 (1901), pp. 559–572. DOI: 10.1080/14786440109462720.

[4] Marten Bernhardt et al. “X-Ray Micro- and Nanodiffraction Imaging on Human Mesenchymal Stem Cells and Differentiated Cells”. In: *Biophys. J.* 110.3 (2016), pp. 680–690. DOI: 10.1016/j.bpj.2015.12.017.

[5] Jan-David Nicolas et al. “Scanning X-ray diffraction on cardiac tissue: automatized data analysis and processing”. In: *J. Synchrotron Radiat.* 24.6 (2017), pp. 1163–1172. DOI: 10.1107/s1600577517011936.

3.1.2 Detection of cell bodies

The local thresholding process described above can be improved by implementing a way to automatically select the size of the neighbourhood within which the local threshold is computed. The size of the neighbourhood should be on the order of that of the objects to be detected. Thus, we start the process with the default neighbourhood of the Matlab (The MathWorks, Inc., Natick, MA, USA) adaptthresh() function (Image Processing Toolbox), namely a rectangle each side of which is 1/8 of the sides of the full dark field contrast image. The average area of the resulting segmented objects is then used to define a new neighbourhood with the same area as the average area of the segmented objects. As there is no reason to prefer one direction, the neighbourhood should be a square, so the value of its area fully defines it. The default neighbourhood is much bigger than the typical size of one cell, therefore the procedure tends to reduce the size of the neighbourhood. The procedure is iterated until the new side of the square differs from the old one by two pixels or less.

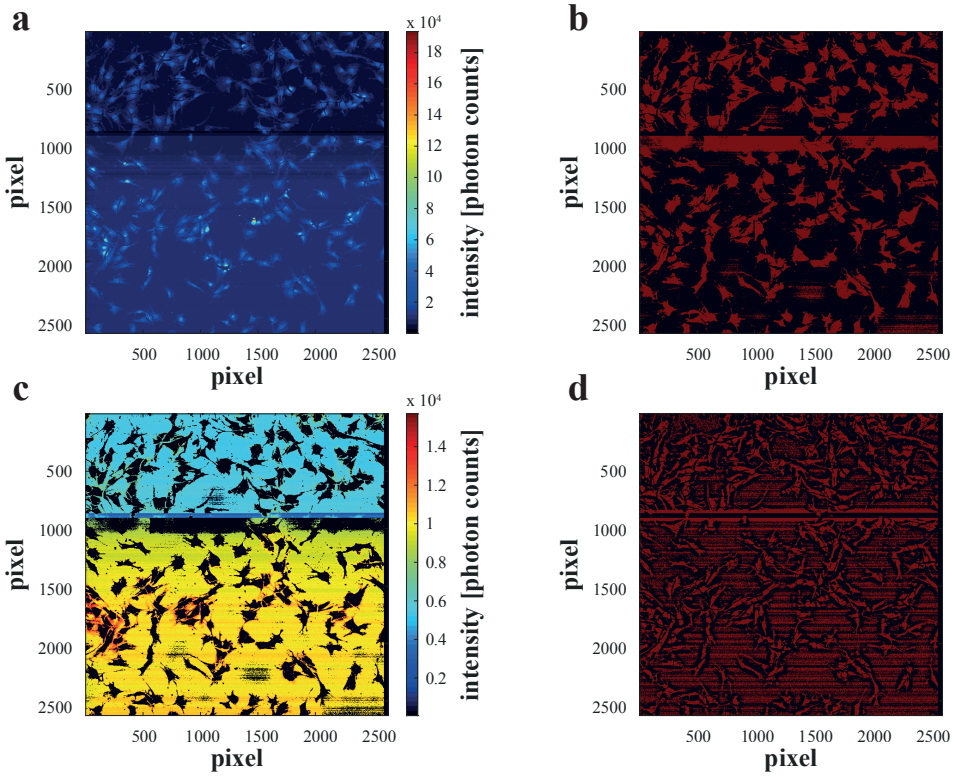

Figure 3.6: Example of local thresholding with different neighbourhood sizes. a) Dark field contrast image of a SAXS scan of freeze-dried vim -/- + hDes WT cells on a silicon nitride membrane. b) Binarization of the dark field contrast image shown in panel a with the default neighbourhood (329 pixel × 323 pixel). The foreground is shown in red, the background in black. c) Background region of the dark field contrast image in panel a according to the mask in panel b. d) Binarization of the dark field contrast image shown in panel a with the neighbourhood determined by iteration (67 pixel × 67 pixel). The foreground is shown in red, the background in black. Each pixel represents a different scan position, so the pixel size is 0.5 µm × 0.5 µm.

An example is shown in Figure 3.6, where the local thresholding is applied to the dark field contrast image in panel a. The default neighbourhood and the neighbourhood determined by iteration are compared. The use of the larger default neighbourhood produces a binarization that overestimates the foreground (Figure 3.6b). Therefore, its negation can be used to define the background region (Figure 3.6c). Conversely, the iteratively determined neighbourhood

results in a binarization that recognizes the gaps between cell fragments, but it also includes many background pixels into the foreground (Figure 3.6d). The background pixels included in the foreground in Figure 3.6d can be removed using the background mask to exclude them.

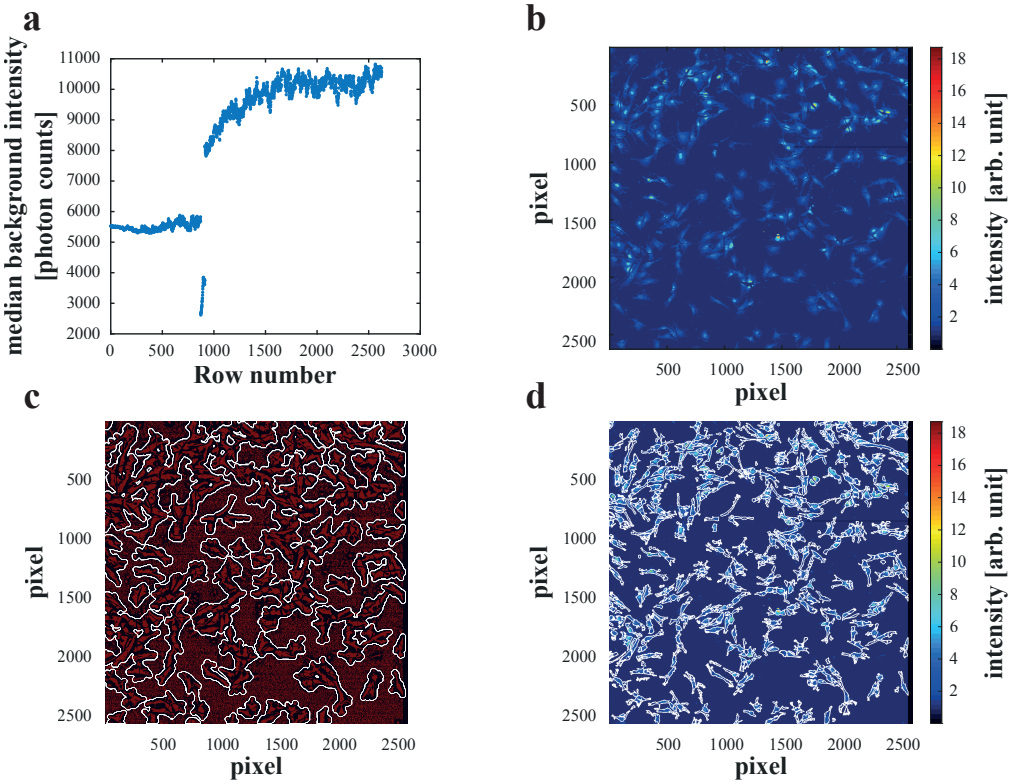

Figure 3.7: Intensity normalization and local thresholding. a) Median background intensity for each row of (Figure 3.6c). b) Result of normalizing the intensity of the dark field contrast image in Figure 3.6 panel a by dividing each of its rows by the corresponding median background intensity value. c) Binarization of the dark field contrast image shown in Figure 3.6a with the neighbourhood determined by iteration. The foreground is shown in red, the background in black. The white outlines represent background regions to be excluded from the foreground, detected by smoothing and expanding the background region obtained with the default neighbourhood. d) Normalized dark field contrast image with the foreground region outlined in white. Each pixel represents a different scan position, so the pixel size is 0.5 µm × 0.5 µm.

As a result of temporal variations in the intensity of the incoming X-ray beam, the overall intensity of the dark field contrast image can undergo significant changes, particularly along the slow (vertical) scan direction (Figure 3.6a, c). This impairs both the segmentation and the subsequent analysis, as the intensities of scattering patterns obtained with different incoming intensities cannot be consistently compared to each other. In order to correct for this, we take, for each horizontal line of the scan, the median intensity value of the background (Figure 3.7a). Each horizontal line of the dark field contrast image is divided by the corresponding median background intensity value: the resulting dark field contrast image (Figure 3.7b) displays a much more uniform intensity level. The scattering patterns can also be corrected in the same way, by dividing their intensity by the median background intensity value of the horizontal line they belong to, so that scattering patterns of different parts of the scan can be compared. The intensity thresholding is repeated on the corrected dark field contrast image, resulting in the binarization shown in Figure 3.7c. The white contours outline background regions to be excluded from the foreground. These background regions are obtained by binarizing with the default neighbourhood followed by morphologically opening the foreground mask with a

disk-shaped structuring element with a two pixel radius. Regions composed of less than 100 pixels are excluded. A diamond-shaped structuring element with a radius of 25 pixels is used to morphologically close the mask and regions with less than 1200 pixels are excluded. The mask is then dilated with a 20 pixel radius disk-shaped structuring element. The logical negation of this mask includes regions of the background that were mistakenly included into the foreground. The final foreground region is outlined on the dark field contrast image in Figure 3.7d.

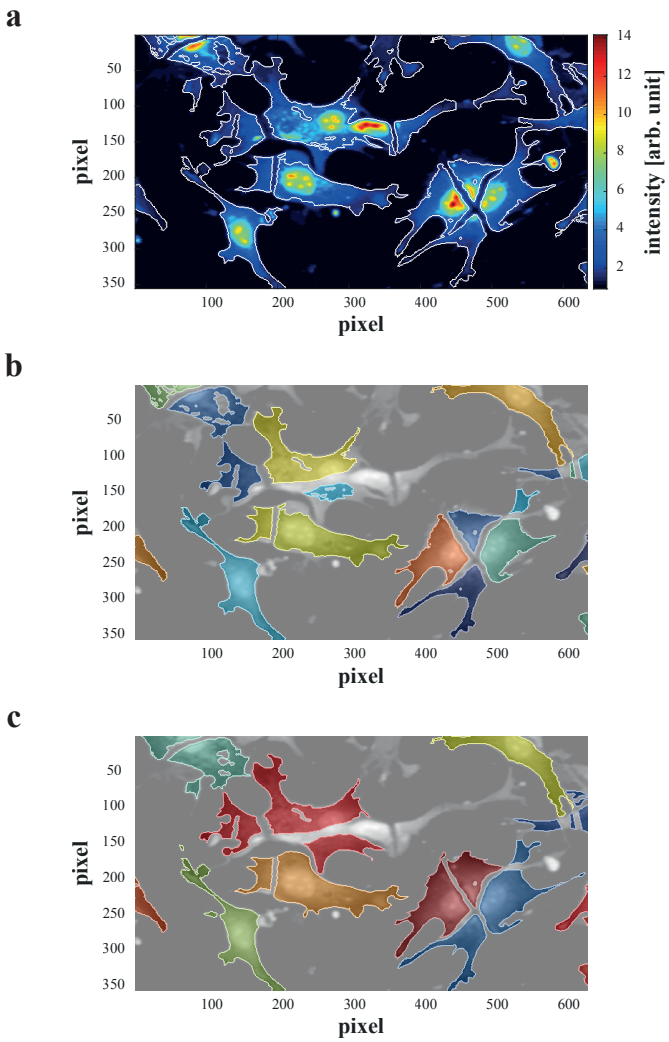

Figure 3.8: Manual check of the cell body mask. a) Portion of a dark field contrast image of a SAXS scan of freeze-dried vim -/- + hDes R406W cells on a silicon nitride membrane. Outlines of the foreground mask obtained by local thresholding are shown in white. b) The same dark field contrast image portion as in panel a is shown here in gray scale. Overlaid on it in different colors are the cell bodies after manual exclusion of unwanted regions. Different colors represent different labels. c) Final cell bodies for the dark field contrast image shown in panel a. The dark field contrast image is shown in gray scale, and the cell bodies are overlaid on it in different colors. Each color represents a different cell. Each pixel represents a different scan position, so the pixel size is 0.5 µm × 0.5 µm.

While this procedure distinguishes the foreground fairly well from the background, a manual check on the mask is still needed to exclude unwanted debris and where cells overlap. An example of this exclusion is shown in Figure 3.8 for a portion of a dark field contrast image. Figure 3.8a displays the contours of the "raw" mask obtained by local thresholding, while Figure 3.8b shows the same cells where unwanted regions have been masked out. Each fragment is "labelled", *i. e.* it is assigned a unique number; each color in Figure 3.8b represents a different

label. Next, fragments belonging to the same cell are manually grouped to be assigned the same label. Finally, portions of the cells mistakenly excluded from the foreground are manually included. The result is shown in Figure 3.8c, where fragments belonging to the same cell are displayed in the same color (same label).

3.1.3 Background definition

As mentioned above, the background region can be obtained via a logical negation of an overestimated version of the foreground mask (Figure 3.6b). A typical background region thus defined contains about 3×10^6 scattering patterns; as a comparison, typical cells comprise about (4–10) $\times$ 10^3 scattering patterns. It is therefore reasonable to decrease the number of scattering patterns used in the analysis, so that computation times are reduced. To this end, only background positions with dark field intensity values within one standard deviation from the average background intensity are used. Moreover, only background scattering patterns belonging to the same horizontal line as the foreground scattering pattern should be used for background subtraction: as the horizontal direction is the fast scanning direction, scattering patterns belonging to the same horizontal line are acquired at close time points. Therefore, we expect little to no variation of the incoming X-ray beam along a horizontal line, so the correct background subtraction needs to be performed with scattering patterns belonging to the same horizontal line. In order to limit the computation times even further, only a fixed number of background scattering patterns per horizontal line are averaged together. For the same horizontal line, averaging 100, 200, 300, 400, 500 or 600 randomly picked background scattering patterns always yields the same radial intensity curve $I_\mathrm{r}(q)$ within experimental error, as can be seen in Figure 3.9. The only effect of a larger number of averaged background scattering patterns is a decrease in the uncertainties of the radial intensity values. Thus, the number of scattering patterns to be averaged per line should be the largest number allowing for the averaging to take a reasonable amount of time: we use 300 scattering patterns per line. With our current computational setup, the average background scattering pattern determination for a full window scan takes about 24 h.

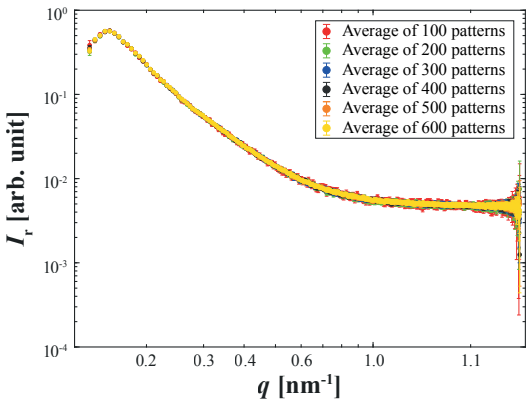

Figure 3.9: Background radial intensity profiles obtained via azimuthal integration of average scattering patterns. The different scattering patterns are a simple average of 100 (red), 200 (green), 300 (blue), 400 (black), 500 (orange) and 600 (yellow) background scattering patterns randomly selected from the same row of the scan.

3.1.4 Detection of nuclei

In the article reproduced above, each fragment belonging to the foreground of the dark field contrast image is treated as a cell. In that case, each fragment needs to have a nucleus and it can happen that parts of the same cell are treated separately. In contrast, when multiple fragments are considered as belonging to the same cell, it is no longer advisable to retain only one region of the cell as the nucleus and discard other bright regions, because the nucleus might be fragmented. Moreover, because of fragmentation, the nucleus is not necessarily circular- or oval-shaped, therefore a morphological opening with a disk-shaped structuring element is not indicated.

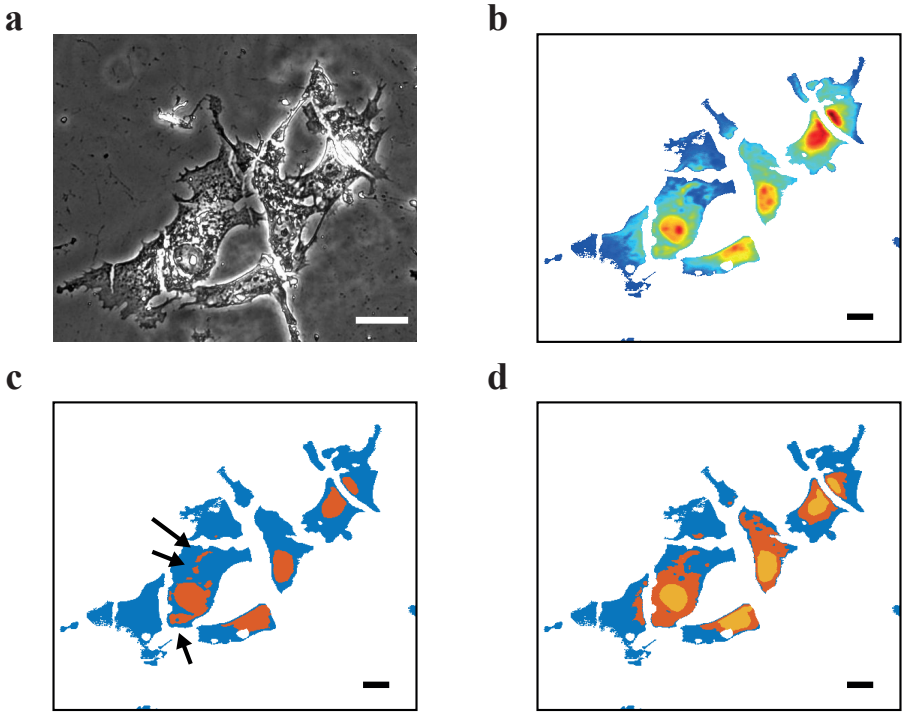

Figure 3.10: Detection of cell nuclei. a) Optical phase contrast image of freeze-dried vim -/- + hDes R406W cells on a silicon nitride membrane. b) Dark field contrast image of a SAXS scan of the cells in panel a. c) Separation of the cells in panels a and b into a high (orange) and a low (blue) intensity region by a single intensity threshold. The black arrows point out examples of regions that are included in the high intensity region and do not belong to the nuclei. d) Separation of the cells in panels a and b into a high (yellow), a medium (orange) and a low (blue) intensity region by two intensity thresholds. Scale bars: 35 µm.

The simplest way to distinguish a nucleus from the rest of the cell remains an intensity threshold, different for each cell as different cells scatter more or less intensely. An example of nuclei detection is shown for a portion of a sample in Figure 3.10. Figure 3.10a displays a phase contrast image of freeze-dried vim -/- + hDes R406W cells on a silicon nitride membrane. The dark field contrast image of a SAXS scan of the same cells is shown in Figure 3.10b, where the cell bodies have already been segmented and the background is omitted. For each cell, the dark field intensity distribution is considered and Otsu's criterion [77] is applied to obtain either one (Figure 3.10c) or two (Figure 3.10d) intensity thresholds, using Matlab multithresh() function. While the single threshold is already very effective in separating nuclei (Figure 3.10c, orange) and cytoplasm (Figure 3.10c, blue), few bright regions of the cytoplasm are sometimes included in the nuclear region (black arrows in Figure 3.10c). In contrast, the use of two thresholds (Fig-

ure 3.10d) divides each cell into three intensity levels: the high intensity region (Figure 3.10d, yellow) almost always coincides with the nucleus of the cell; the medium intensity region (Figure 3.10d, orange) includes the brightest portions of the cytoplasm, usually located around the nucleus; finally, the low intensity region (Figure 3.10d, blue) accounts for the peripheral cytoplasm.

3.2 Comparison of different cell lines

In this section, scanning SAXS is applied to a biological problem: we quantitatively compare three different cell lines. Thanks to scanning SAXS, we are able to combine a moderate-resolution overview of the sample, offered by a dark field contrast image of the scan, with nanometer-resolution quantitative structural information from the single scattering patterns acquired at each sample position. The fast scanning mode allows us to obtain SAXS scans of a large number of cells (several tens to hundreds), thus rendering the comparison more statistically sound than simply measuring 30 cells or less, as is typical for traditional (slower) scanning SAXS. A quantitative analysis is achieved by examining both the dark field contrast images and the scattering patterns. The dark field contrast images allow us to retrieve quantities pertaining to individual cells, such as the cellular area or the intensity scattered by one cell. The scattering patterns reveal properties of the local position of the cell that was irradiated to obtain them. Such properties emerge by characterizing the radial intensity profile and the azimuthal intensity profile of a given scattering pattern, *i. e.* by quantifying how the scattered intensity decays as the distance from the beam center increases, and by quantifying how much the scattered intensity deviates from an isotropic distribution around the beam center.

3.2.1 Biological system

Desmin is an intermediate filament protein expressed in smooth, skeletal and cardiac muscle cells [112–121]. It is believed to play a fundamental role in the organization of the cellular architecture of myocytes, in their resistance to mechanical stress and in the alignment and cohesion of myocytes within muscular tissue [112–117, 119, 120, 122–126]. The importance of desmin in muscle tissue is confirmed by a class of degenerative muscular diseases, called desminopathies and cardiodesminopathies, caused by mutations in the human desmin gene [93, 116, 117, 121, 125–134]. Mutations in the desmin gene can encode for a mutant version of the desmin protein: mutant desmin can present anomalies in the formation of filaments. While it is possible to quantify and compare the ability of different mutants to form filaments *in vitro*, using for instance electron microscopy or atomic force microscopy [93, 118, 119, 125, 129, 130], a quantitative comparison in cells is more challenging, as the system is more complex and resolution at different scales is required: ideally, both the entire cell and subcellular positions should be monitored. Scanning SAXS offers moderate resolution in real space, limited by the beam dimension and by the step size of the scan, and high resolution in reciprocal space, where it is limited at large angles (nanometers in real space) by the noise level and at small angles (tens of nanometers in real space) by the beam stop size. Thus, scanning SAXS is an ideal candidate to compare subcellular structures of different cell lines. In particular, the fast scanning capabilities of the microbranch of ID13 (ESRF, Grenoble, France) allow for large scans, so that, for each cell line, tens to hundreds of cells, instead of up to 5 cells [64], can be assessed. With fast scanning SAXS, we can therefore safely state that we are comparing cell lines, capturing the specific properties of a population of cells rather than of few individual cells, where the variability of the single cell could bias the conclusions drawn for the entire cell line. Here, we apply fast scanning SAXS to mouse embryonic fibroblasts lacking vimentin and expressing either wild type human desmin or mutant R406W human desmin (vim -/- + hDes WT cells and vim -/- + hDes R406W cells, respectively, as explained in Section 2.1). Both cell lines derive from vimentin knockout mouse embryonic fibroblasts (vim -/- cells), that are also measured as a control. The use of these specific cell lines reduces the complexity of the system: we use the vim -/- cells as a common environment where two different types of human desmin, wild type or R406W, are expressed. We therefore expect differences within the three cell lines to stem from the differences in their desmin proteins (or their lack of any intermediate filament

protein, in the case of vim -/- cells).

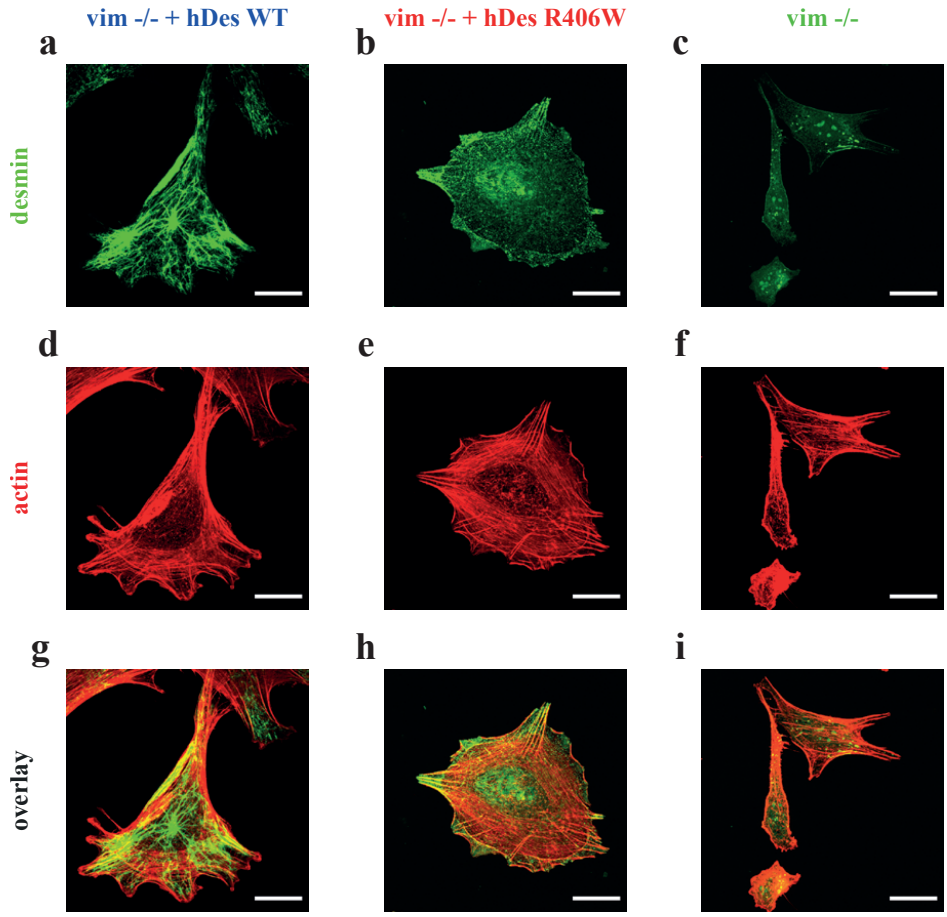

Figure 3.11: Confocal images of desmin and actin in vim -/- + hDes WT, vim -/- + hDes R406W and vim -/- cells. Desmin in a) vim -/- + hDes WT, b) vim -/- + hDes R406W and c) vim -/- cells is shown in green. Actin in d) vim -/- + hDes WT, e) vim -/- + hDes R406W and f) vim -/- cells is shown in red. g) Overlay of panels a and d. h) Overlay of panels b and e. i) Overlay of panels c and f. Scale bars: 25 µm.

In order to observe the different structures formed by the wild type and mutant desmin in these cell lines, we fluorescently stain the desmin and actin in the three cell lines and image them with a confocal microscope, as detailed in Section (2.3). Typical fluorescence micrographs are shown in Figure 3.11. We cannot see any evident differences within the actin networks of the different cell lines (Figure 3.11d-f). Vim -/- + hDes WT cells display well-developed desmin networks (Figure 3.11a), confirming that we can confidently use them as a model for healty desmin expression. In stark contrast, vim -/- + hDes R406W cells do not display any network-like structure in the desmin channel (Figure 3.11b), but rather few regions of stronger fluorescent signal, where brighter dots appear, particularly at the periphery of the cells. A comparison between the desmin antibody signal from vim -/- + hDes R406W cells and from vim -/- cells (Figure 3.11c), where the latter are used as a control, since they do not express desmin at all, highlights the faintness of the R406W desmin signal: while differences emerge clearly, particularly at the cell periphery, the high laser power necessary to clearly see desmin signal in the vim -/- + hDes R406W cells make some bright spots emerge also in the images of vim -/- cells, most likely due to autofluorescence of the cell. The same observations can be made for Figure 3.12, which displays the desmin signal of two additional cells per cell line.

All the desmin images were acquired with the same experimental settings and the intensity scale used in Figure 3.12 is the same for all cells, so that the different strength of the signals can be directly compared. These observations suggest that the desmin aggregates formed by R406W desmin in the cytoplasm are very small, comparable with the resolution of the confocal microscope (0.215 µm). It is therefore importat to use caution when interpreting the desmin fluorescent signal from vim -/- + hDes R406W cells.

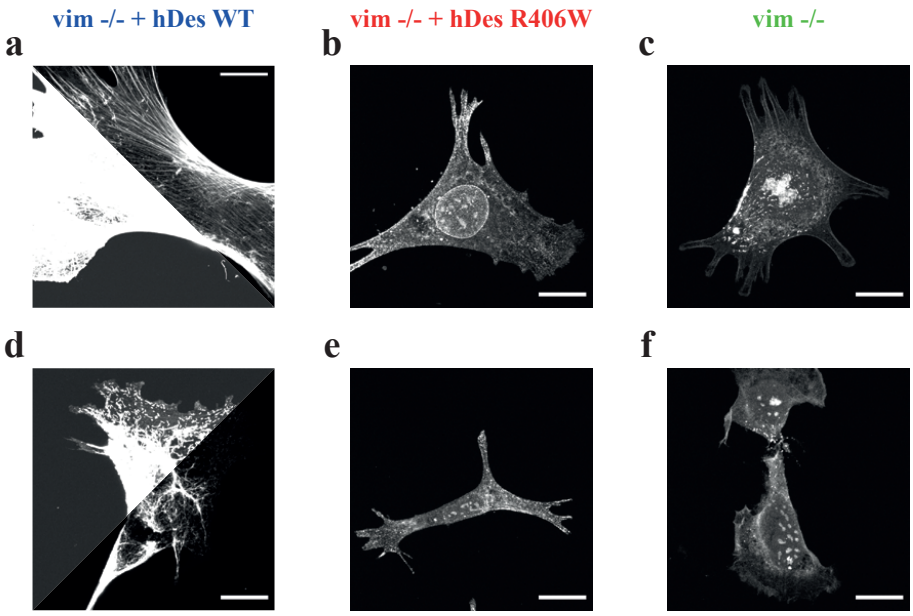

Figure 3.12: Confocal images of desmin in vim -/- + hDes WT, vim -/- + hDes R406W and vim -/- cells. The same intensity scale is used for better comparison of the different images. a, d) Desmin network in vim -/- + hDes WT cells. The half images containing the scale bar are displayed using an intensity scale suitable for visualizing the network well; the other halves employ the same intensity scale necessary to see the desmin signal from the mutant expressing cells (shown in b, e). b, e) Desmin channel in vim -/- + hDes R406W cells. c, f) Desmin channel in vim -/- cells. Using the same intensity scale as in panels b, e, some signal emerges, although these cells do not express desmin. Scale bars: 25 µm.

The maximum thickness of the three cell lines is also measured, as detailed in Appendix A. Briefly, the maximum thickness is defined as the distance between the surface of the cell culture dish, where the cells adhere, and the last plane where at least a portion of the nuclear surface is still in focus. As the nucleus is the thickest part of the cells that we measure, for each cell the maximum thickness of the nucleus is measured. As reported in Table A.1, an average thickness value is computed for each cell line. No relevant difference in thickness among the three cell lines emerges.

3.2.2 Cell area and scattered intensity

Four silicon nitride windows containing vim -/-, vim -/- + hDes WT (two windows) or vim -/- + hDes R406W cells are scanned during the October 2018 experiment in fast scanning SAXS mode. All scans are performed in $\Delta y = \Delta z = 0.5\,\mu\text{m}$ steps in both horizontal and vertical direction, with an exposure time of $T = 3\,\text{ms}$. Each sample is irradiated with a dose $D = 7.6 \times 10^6\,\text{Gy}$, obtained as:

$$D = \frac{\mu/\rho_m I_0 h\nu T}{\Delta y \Delta z}, \tag{3.5}$$

with $h\nu = 13.0\,\text{keV}$ the photon energy; $\mu/\rho_m = 2.55\,\text{cm}^2\,\text{g}^{-1}$ the ratio between mass attenuation coefficient and mass density of the cellular material [28] at 13.0 keV (assuming the average composition of the cellular material to be $H_{50}C_{30}N_9O_{10}S$); $I_0 = 1.2 \times 10^{12}$ cps the photon flux. In total, one window-wide scan per window is taken, with slightly different fields of view. The number of horizontal and vertical steps of each scan is listed in Table 3.5, together with the corresponding field-of-view.

Table 3.5: Number of scan steps, corresponding field-of-view and number of cells for the four window-wide scans performed during the October 2018 experiment.

Scan	Hor. steps	Vert. steps	Field-of-view [mm^2]	Number of cells
vim -/-	2832	2154	1.4×1.1	72
vim -/- + hDes WT (1)	2633	2626	1.3×1.3	189
vim -/- + hDes WT (2)	2633	2562	1.3×1.3	244
vim -/- + hDes R406W	2832	2487	1.4×1.2	192

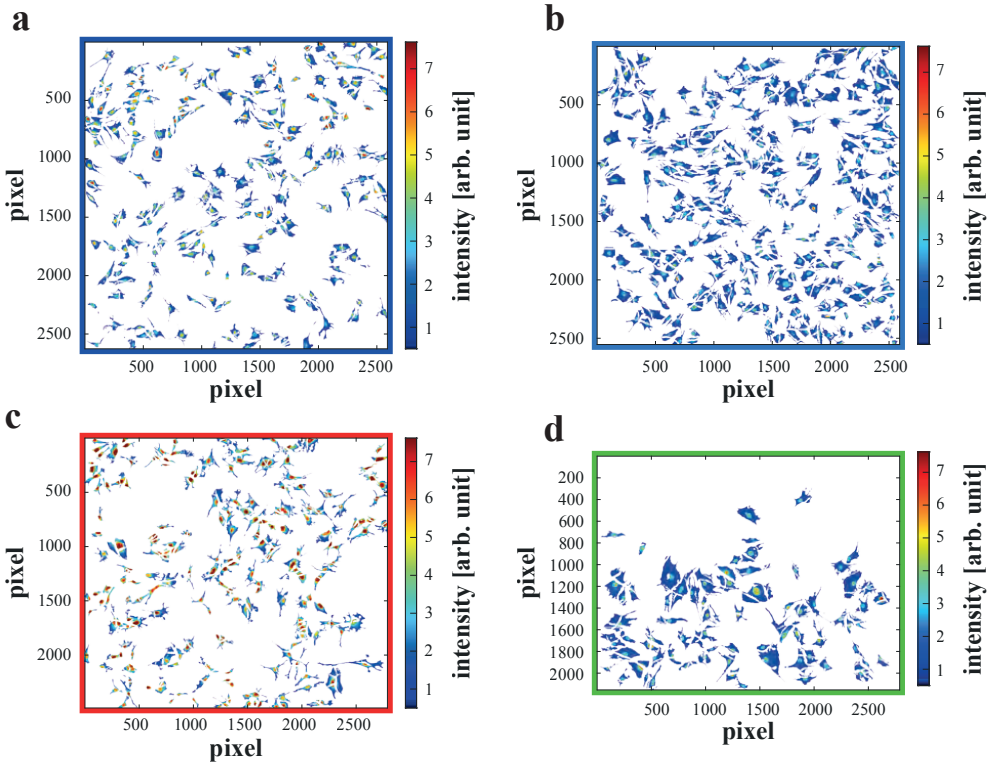

Figure 3.13: Dark field contrast images of window-wide scans. a) Vim -/- + hDes WT (1). b) Vim -/- + hDes WT (2). c) Vim -/- + hDes R406W. d) Vim -/-. Each pixel represents a different scan position, so it equals 0.5 µm × 0.5 µm.

A dark field contrast image is computed for each scan. For each scan position, all intensity values in the scattering pattern are summed together, obtaining the intensity scattered in total from that position; each summed scattered intensity value is plotted at the corresponding position to form the dark field contrast image. Each dark field contrast image is segmented into cells and background with the procedure explained in Section 3.1. In order to account for variations in the primary beam intensity, each horizontal line of the dark field contrast image is divided by the median intensity value of the background. Thus, each horizontal line is associated with a normalization factor, used not only to display the dark filed contrast images, but also, in

later analysis, to normalize the intensity of the scattering patterns belonging to the same line. The segmented dark field contrast images of the four scans are shown in Figure 3.13, where the intensity normalization has already taken place, the background is not displayed and all images are shown in the same intensity scale. For each scan, the number of cells segmented and used in the subsequent analysis is listed in Table 3.5. A simple visual inspection of Figure 3.13 suggests that larger cells occur more likely among vim -/- cells (Figure 3.13d), and that a larger scattered intensity is more commonly found among vim -/- + hDes R406W cells (Figure 3.13c).

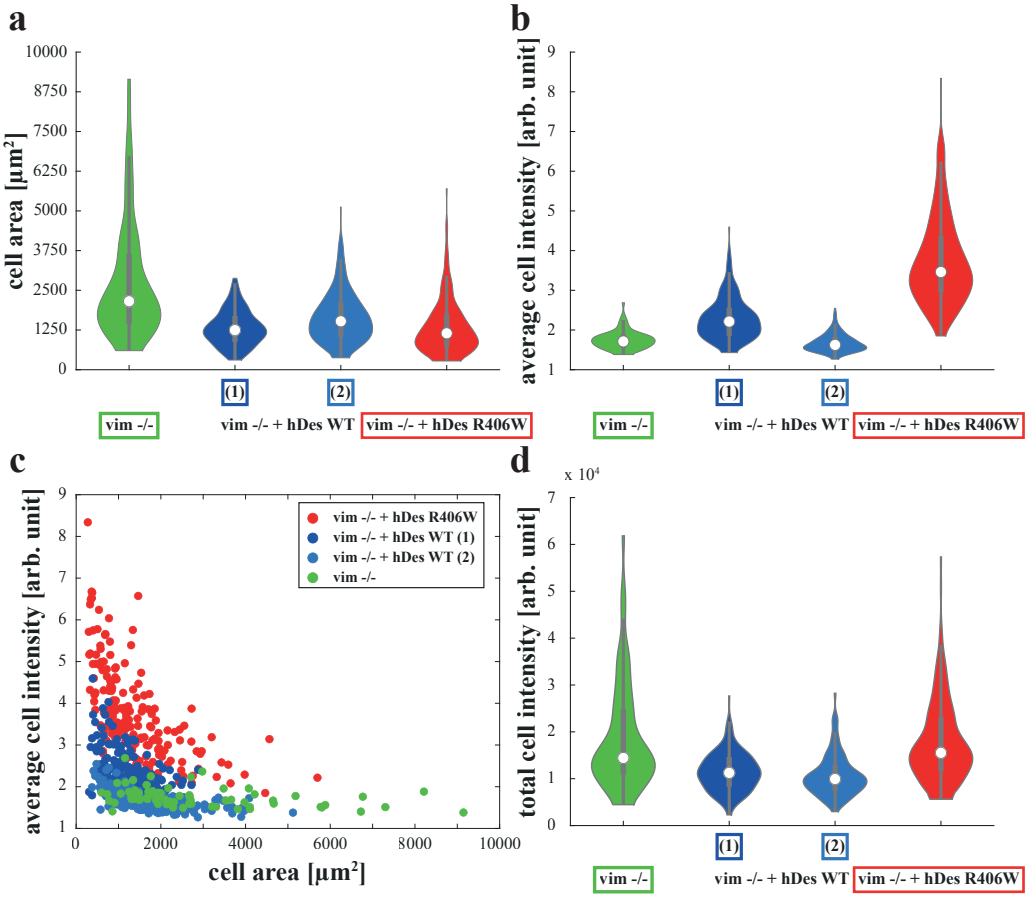

Figure 3.14: Areas and scattered intensities of the cells shown in Figure 3.13. a) Violin plots of the distributions of cell area. b) Violin plots of the distributions of average cell scattered intensity. c) Average cell scattered intensity plotted against cell area. d) Violin plots of the distributions of total cell scattered intensity. The median values are shown in the violin plots [135, 136] by white circles, while the gray boxes indicate the interquartile range and the gray whiskers mark the interval outside of which the data are considered outliers by Tukey's criterion [137].

In order to verify these impressions, the distributions of the cell areas and of the intensity scattered on average by each cell are compared among the four scans in Figure 3.14a, b respectively. The area occupied by a cell is defined by the number of pixels in the dark field contrast image belonging to the cell, multiplied by the area of one pixel, *i. e.* 0.25 µm^2. The average cell intensity is computed from the dark field contrast image by summing all the scattered intensity values belonging to the cell and dividing the sum by the number of pixels belonging to the cell. The cell area distributions compared in Figure 3.14a present similar but different median values (white circles) and interquartile ranges (gray boxes). In agreement with the qualitative considerations emerging from a visual inspection of Figure 3.13, the vim -/- + hDes R406W cells have the smallest median area (1147 µm^2), while the vim -/- cells have the largest (2156 µm^2). In addition, the distribution of the the vim -/- cellular areas is wider than the

others and it reaches larger extreme values. The area distributions of the two vim -/- + hDes WT scans are noticeably different, as confirmed by a two-sample Kolmogorov-Smirnov test [138], that yields a p-value of 8×10^{-5} for the null hypothesis that the two data sets have the same distribution (it is customary to reject the null hypothesis when $p < 0.05$). The four scans differ even more when the average cell intensity is considered (Figure 3.14b). In this case, the largest median intensity value is that of vim -/- + hDes R406W cells (3.46), the lowest is that of vim -/- cells (1.71). A two-sample Kolmogorov-Smirnov test on the average cell intensity distributions of the two vim -/- + hDes WT scans yields an extremely low p-value (5×10^{-38}) for the null hypothesis that the two data sets have the same distribution. Considering how large area values seem to correspond to small average intensities and *vice versa*, it is reasonable to ask if there is a dependency between the area of a cell and the average intensity scattered by the cell. Indeed, when plotting the average cell intensity against the cell area (Figure 3.14c), it is clear that the two variables are not independent of each other. Specifically, lower average intensities seem to occur more likely for larger cells and, conversely, large average intensities appear to be more frequent for smaller cells. In order to explain this, let us make the irrealistical assumption that the electron density of the cellular material is homogeneous throughout the cell and that all cells have the same volume. This would mean that each cell scatters globally the same amount of radiation, thus the averaging process over the cell area would yield average intensities inversely proportional to the cell area. If these conditions were exactly valid, then for each cell line the total scattered intensity (*i. e.* the sum of all the scattered intensity values belonging to one cell, not divided by the number of pixels belonging to the cell) would be a constant, dependent on the electron density and on the volume of a cell. For each cell line, the distributions of total cell intensity would therefore be normal distributions centered on this cell line-specific value. This is not the case in reality, as shown in Figure 3.14d: all distributions are asymmetric, with "tails" elongated towards large intensity values. This comes as no surprise, as volume variability within the same cell line is well documented, as well as local density variations within a single cell [4, 139–143]. Nevertheless, the two distributions of vim -/- + hDes WT values resemble each other more than in the case of cell areas or average intensities, even though we still cannot consider them as one distribution (the two-sample Kolmogorov-Smirnov test gives here $p = 4 \times 10^{-4}$). Thus, it is reasonable to conclude that the dependency between average cell intensity and cell area is indeed caused by the fact that larger cells tend to be overall thinner and thus they scatter less on average, although the dependency is not a perfect inverse proportionality.

3.2.3 Radial intensity profiles

While the dark field contrast images provide information about "global" properties of the cells, such as their area, each scattering pattern is determined by the local structures irradiated to obtain it. Specifically, the irradiated volume is defined by the beam size ($1.5\,\mu\text{m} \times 3\,\mu\text{m}$) and by the thickness of the cell in that position. Within that volume, all structures with dimensions corresponding to the accessible q range contribute to the signal: in this case, $q \in [2.2, 36]\ \text{nm}^{-1}$, corresponding to real space lengths of about 2 nm to 36 nm. As more extensively explained in Section 3.2.4, the individual scattering patterns in these scans are fairly isotropic, so most of the information they can provide resides in the way that the scattered intensity changes as the distance from the beam center grows, regardless of the azimuthal angle φ. Each scattering pattern is therefore azimuthally integrated, to obtain radial intensity profiles $I_\text{r}(q)$. Additionally, the signal is not very strong: thus, it is advisable to look at averaged radial intensity profiles. In particular, as desmin imaging suggests that the vim -/- + hDes R406W cells express desmin mostly in the cell periphery (Figures 3.11 and 3.12), the cell periphery of the three cell lines should be compared. As detailed in Section 3.1, each cell is segmented

into three regions of interest by the use of two Otsu's thresholds on the intensity of its dark field signal. For each cell, the thresholds are chosen using Matlab multithresh() function on the intensity distribution of the cell, so different thresholds are used for different cells.

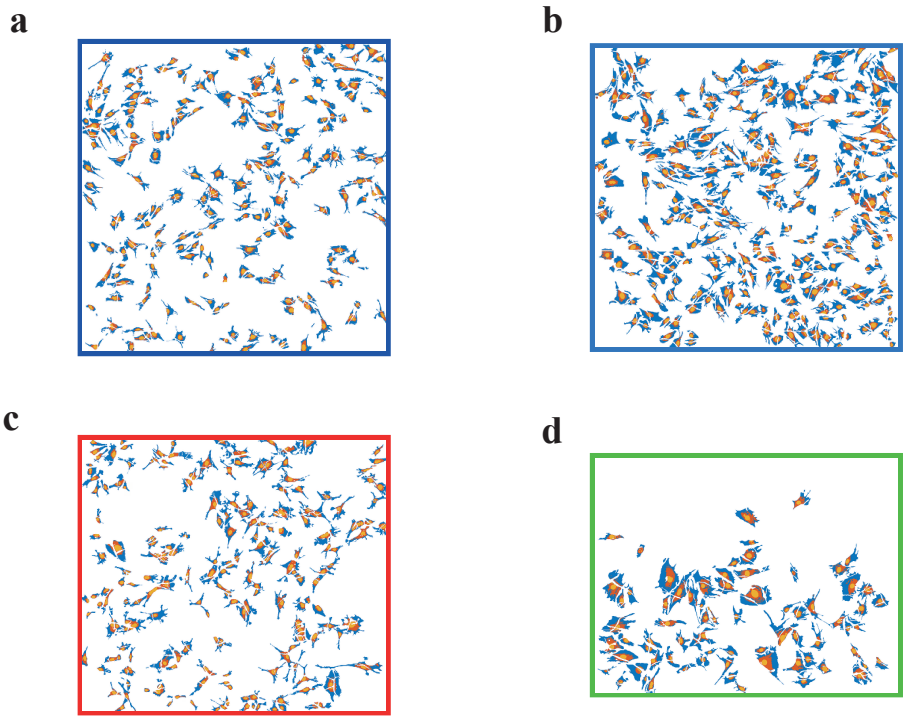

Figure 3.15: Cellular regions of interest corresponding to the dark field contrast images of Figure 3.13 (same dimensions). a) Vim -/- + hDes WT (1). b) Vim -/- + hDes WT (2). c) Vim -/- + hDes R406W. d) Vim -/-. The high intensity region is shown in yellow, the medium intensity region in orange and the low intensity region in blue.

Figure 3.15 displays the resulting high (yellow), medium (orange) and low (blue) intensity regions for the dark field contrast images shown in Figure 3.13. For the vast majority of the cells, the high intensity region corresponds to the nucleus, the medium intensity region to cytoplasm close to the nucleus and the low intensity region to cytoplasm far from the nucleus. For a few cells, the high intensity region only includes bright spots in the nucleus and the rest of the nucleus belongs to the medium intensity region. However, the low intensity region reliably excludes the nucleus and accounts for the peripheral cytoplasm, which can be used to obtain average radial intensity curves. In practice, individual scattering patterns belonging to the peripheral cytoplasm are first azimuthally integrated; the radial intensity profiles thus obtained are background-corrected and the intensity is normalized with the median background intensity value of the horizontal line they belong to; finally, all peripheral cytoplasm curves belonging to the same scan are averaged. The resulting average radial intensity profiles are shown in Figure 3.16a.

In accord with the analysis of the dark field contrast images, vim -/- cells (green filled circles) display the lowest intensity, vim -/- + hDes R406W cells (red filled circles) the highest. Additionally, the vim -/- curve drops at relatively small q values ($q \approx 0.7$ nm^{-1}), meaning that, for this scan, the noise level starts at lower q values than for the other scans. This is most probably due to the very faint signal of the vim -/- scan. The two vim -/- + hDes WT curves differ, though slightly, in intensity; they appear to have similar shapes at lower q values, but they significantly deviate from each other in their terminal part: the vim -/- + hDes WT (1) curve (dark blue filled circles) starts to decrease more slowly, resembling the vim -/- + hDes

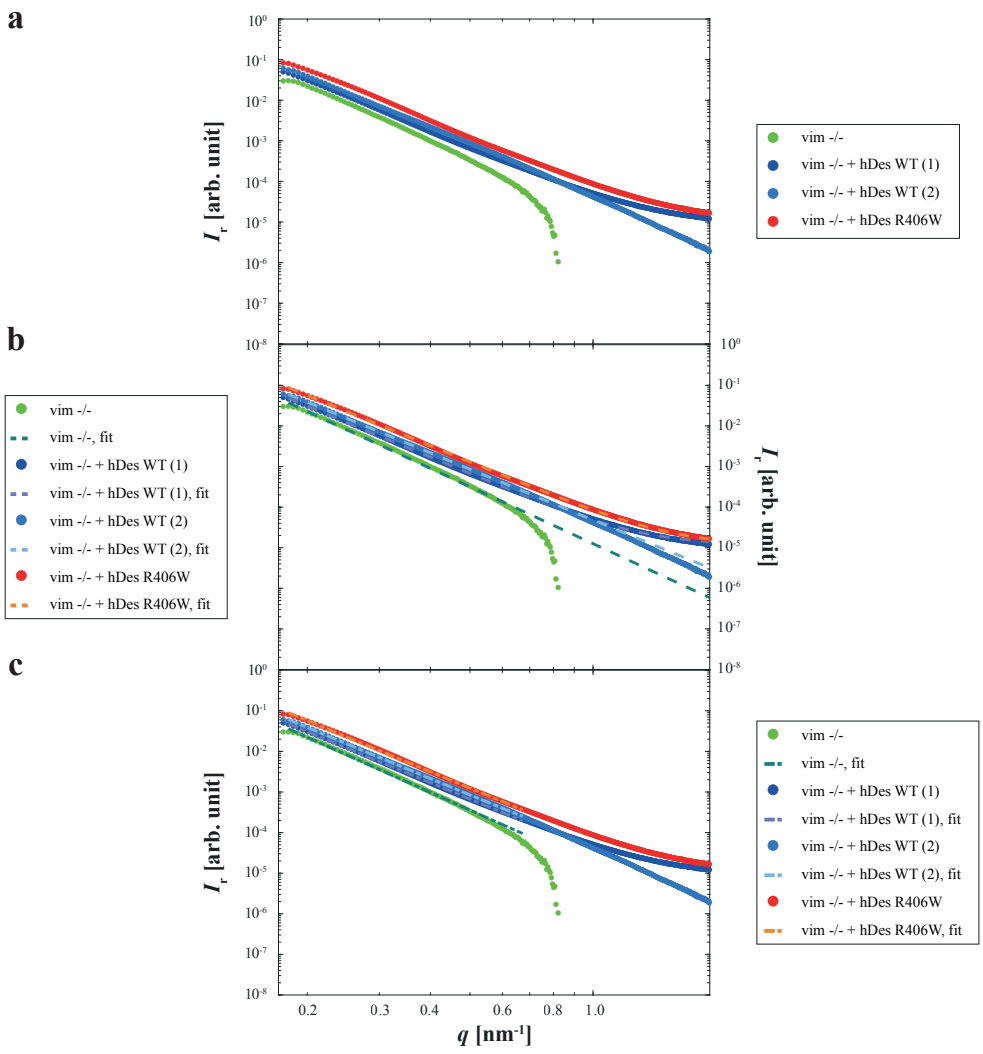

Figure 3.16: Radial intensity decay for the peripheral cytoplasm region. a) Average radial intensity curves for the peripheral cytoplasm (blue regions in Figure 3.13) of the four window-wide scans. b) Results of the power law fits, $q \in [0.1798, 1.925]$ nm^{-1}. c) Results of the power law fits, $q \in [0.1798, 0.6677]$ nm^{-1}.

R406W behaviour, while the vim -/- + hDes WT (2) curve (light blue filled circles) continues its power law decay. Interestingly, while the total scattered intensity is lower for the vim -/- + hDes WT (2) scan than for the vim -/- + hDes WT (1) (Figure 3.14b, d), their radial intensity profiles are "swapped" for lower q values, with the vim -/- + hDes WT (2) curve above the vim -/- + hDes WT (1) curve. A more quantitative description of the radial intensity profiles can be provided by fitting them with a suitable function. A power law is suggested by the seemingly linear decay displayed by all profiles in most of the q range in the double logarithmic plot of Figure 3.16a. The power law behaviour has been observed in various studies on freeze-dried cells and the functional form

$$I_{\mathrm{r}}(q) = Kq^{\alpha} + B \tag{3.6}$$

is usually sufficient to describe this kind of radial intensity profile [56, 62, 64, 65, 67, 68, 71, 73]. Ideally, the fit should be executed in the largest possible q range. The largest q value is usually chosen as the value where the noise level starts. As the noise level for the vim -/- curve starts at much lower q values than for the other curves, two fits are presented, one with $q \in [0.1798, 1.925]$ nm^{-1} (Figure 3.16b), the other with $q \in [0.1798, 0.6677]$ nm^{-1} (Figure 3.16c). The larger fitting range is chosen so that the noise level of the vim -/- + hDes R406W curve is reached and corresponds to real space distances of 3.26 nm to 34.9 nm; the smaller fitting range stops before the noise level of the vim -/- curve and corresponds to real space distances of 9.41 nm to 34.9 nm. The fit coefficients for the larger fitting range are listed in Table 3.6, those for the smaller fitting range are listed in Table 3.7. The fitting curve for vim -/- cells in the larger fitting range evidently deviates from the data at large q values, confirming that the vim -/- radial intensity profile can only be correctly fitted in the smaller fitting range. The larger-range fit of this profile is dominated by the small-q data because the large-q data have very large uncertainties (not shown). The shape of the fit function is effectively fully described by the the power law exponent α; a larger absolute value for α indicates a faster decay of the radial intensity. In both fitting ranges, the vim -/- curve decays much faster than the other curves, that are almost parallel in the smaller range, as indicated by their α values there, that are equal within experimental error. In the larger fitting range, the vim -/- +hDes WT (2) exponent resembles that of the vim -/- + hDes R406W curve more than that of the vim -/- +hDes WT (1) curve. The two vim -/- +hDes WT curves also differ significantly in their K values, thus they cannot be considered as coinciding even in the smaller fitting range. For both fitting ranges, the vim -/- curve has the smallest K value, followed by the vim -/- + hDes WT (1) curve and by the vim -/- + hDes WT (2) curve; the largest K value is that of the vim -/- + hDes R406W curve. This resembles the comparison of total scattered intensity of Figure 3.14b, d, but with the vim -/- + hDes WT order swapped, as already qualitatively noted in the description of the radial intensity profiles above.

Table 3.6: Fit coefficients of the curves shown in Figure 3.16b. Fitting range: $[0.1798, 1.925]$ nm^{-1}. Values are not accompanied by their uncertainty when Matlab reported a fixed at bound warning for them

Scan	K [$\times 10^{-6}$ arb. unit]	α	B [$\times 10^{-6}$ arb. unit]
vim -/-	12.7 ± 1.0	-4.66 ± 0.06	$\approx 1 \cdot 10^{-5}$
vim -/- + hDes WT (1)	36.5 ± 0.2	-4.189 ± 0.005	11.8 ± 0.4
vim -/- + hDes WT (2)	48.3 ± 0.3	-4.151 ± 0.004	$\approx 1 \cdot 10^{-5}$
vim -/- + hDes R406W	74.0 ± 1.0	-4.126 ± 0.008	11.3 ± 1.3

The values of the additive constant B, that is usually included in equation (3.6) to account for inelastic and incoherent scattering, are very small and effectively negligible in this analysis. The B values reported without error were given as fixed at bound by Matlab's non linear least

Table 3.7: Fit coefficients of the curves shown in Figure 3.16c. Fitting range: $[0.1798, 0.6677]$ nm^{-1}. Values are not accompanied by their uncertainty when Matlab reported a fixed at bound warning for them.

Scan	K [$\times 10^{-6}$ arb. unit]	α	B [$\times 10^{-6}$ arb. unit]
vim -/-	15.6 ± 0.6	-4.51 ± 0.03	≈ 1
vim -/- + hDes WT (1)	36.7 ± 0.4	-4.184 ± 0.008	≈ 2
vim -/- + hDes WT (2)	46.0 ± 1.0	-4.190 ± 0.014	10 ± 10
vim -/- + hDes R406W	67 ± 3	-4.20 ± 0.03	10 ± 30

squares fitting routine, meaning that B would have gone below 0 if the condition $B \geq 0$ was not enforced. All B values for the smaller fitting range are either fixed at bound or they present an error equal to or greater than the value itself, suggesting that in this range $B = 0$. Thus, the fitting function

$$I_{\mathrm{r}} = Kq^{\alpha} \tag{3.7}$$

is used in the smaller range, yielding the results in Table 3.8. As visually these fitting curves do not appear particularly different from those of Figure 3.16c, their plots are omitted. For these results, similar considerations to those above can be made; importantly, in this case the α values of the vim -/- + hDes WT (1), (2) and vim -/- + hDes R406W are no longer equivalent.

Table 3.8: Fit coefficients for equation (3.7), fitting range: $[0.1798, 0.6677]$ nm^{-1}.

Scan	K [$\times 10^{-6}$ arb. unit]	α
vim -/-	17.2 ± 0.6	-4.46 ± 0.03
vim -/- + hDes WT (1)	36.9 ± 0.4	-4.182 ± 0.008
vim -/- + hDes WT (2)	50.0 ± 0.5	-4.128 ± 0.007
vim -/- + hDes R406W	74.7 ± 1.7	-4.119 ± 0.016

3.2.4 Local anisotropy and orientation

SAXS is frequently used to determine sample orientation [144–148], also when combined with scanning the sample [37, 44, 47, 50]. As a scattering pattern is related to the electron density that generated it by a Fourier transform, if the scattering pattern displays a preferred orientation, then the corresponding scatterers also have a preferred orientation, perpendicular to that of the scattering pattern. We test three different methods to automatically compute orientation and anisotropy of our SAXS scans and determine the most suitable for our kind of signal. The anisotropy is meant as a way to quantify how "strongly" the scattering pattern (and thus, the scatterers that originated it) is oriented. Therefore, it is important to always accompany the orientation value with an anisotropy value, as the orientation of isotropic or nearly isotropic scattering patterns is not particularly meaningful. We then look into whether longer exposure times could lead to a better orientation analysis.

Comparison of different methods

We use three different orientation analyses, all successfully employed in the past on scattering patterns from scanning SAXS of biological samples [15, 56, 57, 62, 64, 66–68, 102]. For all three methods, we pre-process the scattering patterns in the same way: we consider a small region of interest around the beam center (Figure 3.17a, b), corresponding to q values in the

range [0.1969, 1.6572] nm^{-1}; the beam stop, detector gaps and invalid (hot or dead) pixels are masked out (Figure 3.17c) and replaced with their point-symmetric counterparts with respect to the beam center (Figure 3.17d).

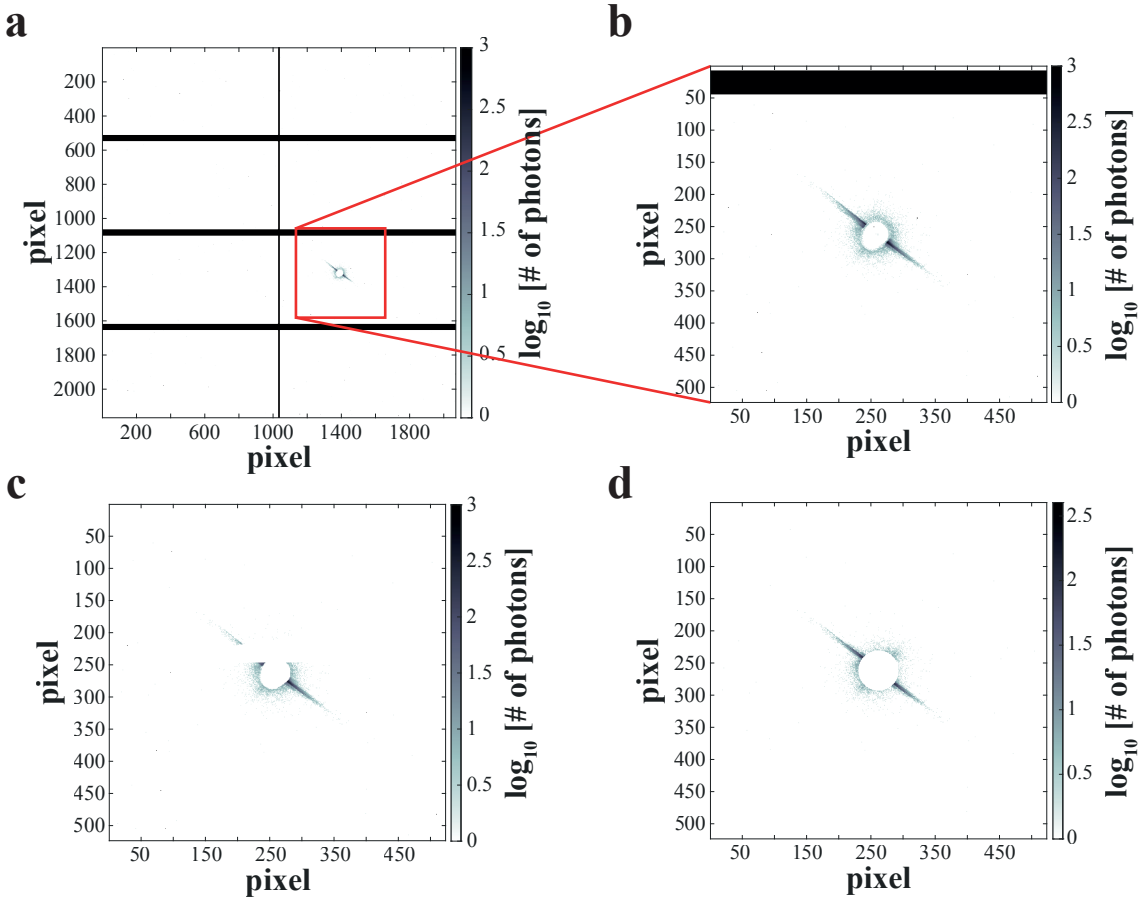

Figure 3.17: Scattering pattern pre-processing for orientation analysis. a) Original scattering pattern. Th red box marks the region of interest, centered on the beam center. b) Enlarged detector region of interest. c) Enlarged detector region of interest; the invalid pixels have been masked out. d) Enlarged detector region of interest; wherever possible, the invalid pixels have been replaced by their point-symmetric counterparts with respect to the beam center.

The first method we use to determine the orientation of a given scattering pattern consists in binarizing the scattering pattern and fitting an ellipse to it: the angle formed by the major axis of the ellipse with the horizontal direction is taken to be the orientation of the scattering pattern. The Matlab code for this analysis is kindly provided by Jan-Philipp Burchert. Following [62], we compute an average background scattering pattern (Figure 3.18a) from "empty" scan regions (where no cells are present) and subtract it from the scattering pattern (Figure 3.17d), coming from a cellular position, that we are analyzing. The result of the background subtraction is shown in Figure 3.18b. Subsequently, we reduce the noise in the scattering pattern with a median filter (Figure 3.18c). An intensity threshold is used to binarize the scattering pattern (Figure 3.18d). The beam stop is added to the binary image as a circular region to avoid artifacts (Figure 3.18e). Finally, an ellipse is fitted to the largest connected component of the binary image using the regionprops() function of Matlab's Image Processing Toolbox (Figure 3.18f). This function returns the centroid of the connected component, the minor and major axis of the ellipse having the same second moments and the orientation φ_{ell} of the major axis of such an ellipse. The eccentricity e of the ellipse can be regarded as a measure of the anisotropy of the scattering pattern, with 0 (a circle) corresponding to perfect isotropy and 1 (a segment

identified with the major axis) corresponding to maximum anisotropy.

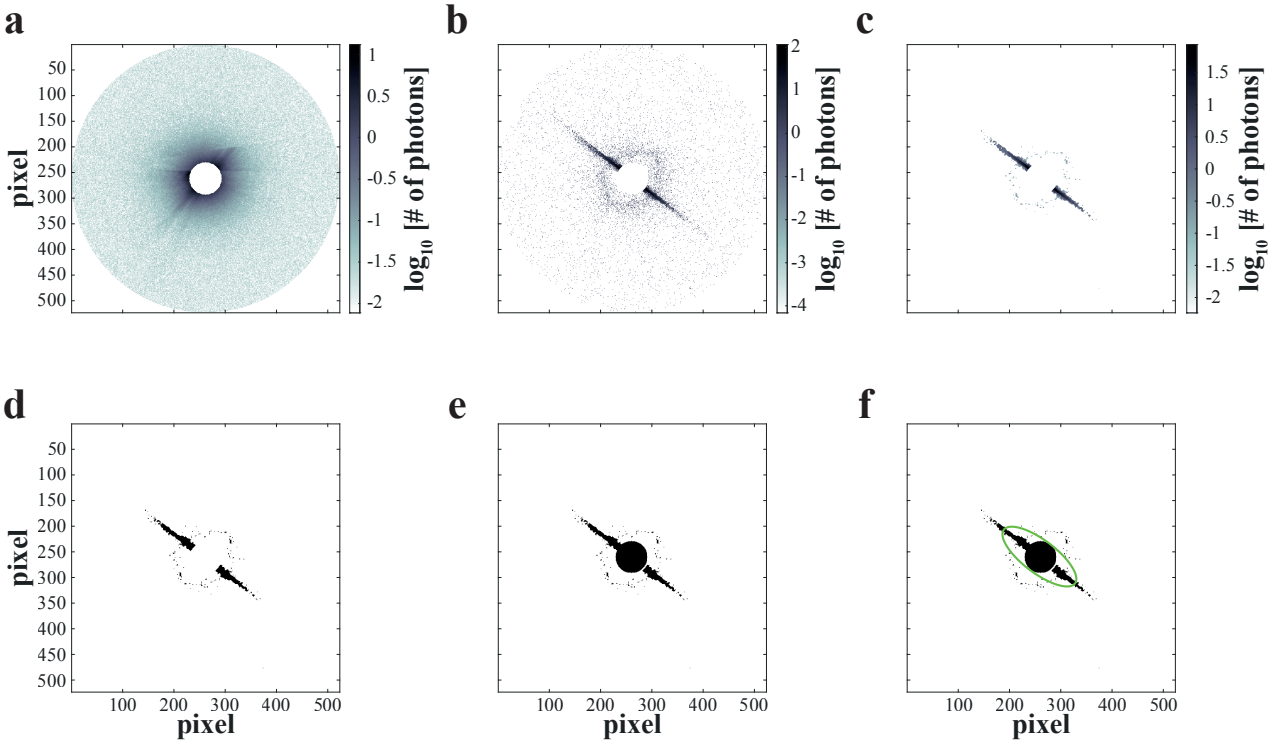

Figure 3.18: Illustration of the ellipse-fitting method. a) Average background scattering pattern, pre-processed as explained in Figure 3.17. b) Background-subtracted scattering pattern. c) Scattering pattern after median filtering. d) Binarized scattering pattern. e) Binarized scattering pattern; the beam stop is added as a circle of radius $0.1969\,\mathrm{nm}^{-1}$. f) Binarized scattering pattern, with the ellipse resulting from the analysis plotted in green.

Since the ellipse fitting method includes some arbitrary choices (namely, the choice of a filter kernel for the median filter and the choice of an intensity threshold for binarization), we decided to also test a parameter-free method, based on principal component analysis (PCA). In this case, the Nanodiffraction Toolbox [15], a set of Matlab scripts developed by dr. Jan-David Nicolas and prof. Tim Salditt at the Institute for X-Ray Physics of the University of Göttingen, is used. The method was described in several publications [15, 64, 66]; briefly, an average background scattering pattern is subtracted from the scattering pattern being analyzed just like for the ellipse fitting method (Figure 3.18b). The covariance matrix of the background-subtracted scattering pattern is computed and diagonalized. The direction of the eigenvector corresponding to the largest eigenvalue (Figure 3.19, blue arrow) coincides with the line of best fit [149], thus its orientation φ_{pca} can be used as the orientation of the scattering pattern. Here, the anisotropy is quantified as the ratio ω between the absolute value of the difference of the two eigenvalues λ_1, λ_2 and their sum:

$$\omega = \frac{|\lambda_1 - \lambda_2|}{\lambda_1 + \lambda_2}. \tag{3.8}$$

A perfectly isotropic scattering pattern has $\lambda_1 = \lambda_2$, thus $\omega = 0$; conversely, a scattering pattern made of perfectly aligned points has $\lambda_2 = 0$, thus $\omega = 1$ corresponds to maximum anisotropy. It should be noted that, while PCA is equivalent to fitting an ellipse to the scattering pattern, the eccentricity e found by the ellipse fitting method and the parameter ω defined by equation (3.8) are *not* the same quantity.

The Nanodiffraction Toolbox mentioned above contains a second way to obtain the orientation of a given scattering pattern, particularly useful when the signal is low and other scattering

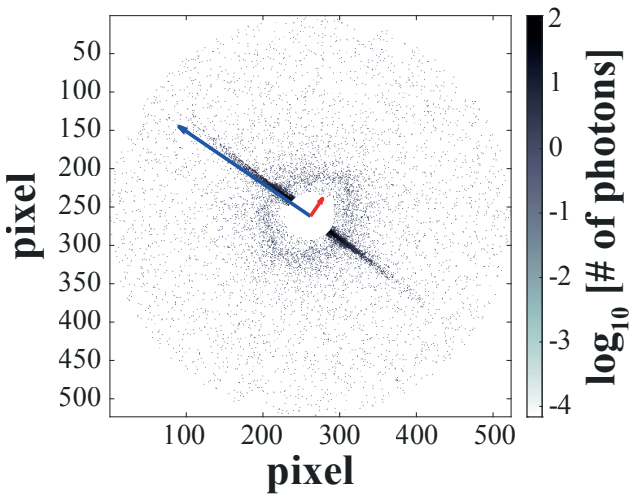

Figure 3.19: Illustration of the PCA method. The blue and red arrows represent the eigenvector of the covariance matrix corresponding to its largest and smallest eigenvalues, respectively. The directions of the two arrows coincide with the directions of the respective eigenvalues. The length of the blue arrow is proportional to the largest eigenvalue, while the length of the red arrow is proportional to the smallest eigenvalue.

contributions, coming e. g. from the X-ray optics or from the beam stop, cause artifacts in the PCA [56]. This alternative method [56, 57] consists in radially integrating the scattering pattern we are analyzing (Figure 3.17d) and the background scattering pattern (Figure 3.18a) separately, to obtain two azimuthal intensity profiles, respectively $I_{\mathrm{frg}}(\varphi)$ (Figure 3.20a, purple) and $I_{\mathrm{bkg}}(\varphi)$ (Figure 3.20a, red). The background-subtracted azimuthal intensity profile (Figure 3.20b, blue) is then computed as $I_{\mathrm{az}}(\varphi) = I_{\mathrm{frg}}(\varphi) - I_{\mathrm{bkg}}(\varphi)$. Finally, the circular mean and variance [150] of $I_{\mathrm{az}}(\varphi)$ are calculated. The circular mean φ_{cir} (Figure 3.20b, green) is taken to be the orientation of the scattering pattern, while the circular variance v can be used to quantify its anisotropy. In particular, $v = 0$ means that the angle does not vary, thus corresponding to maximum anisotropy, while $v = 1$ means that the angle is uniformly distributed within 360°, that is, the scattering pattern is perfectly isotropic.

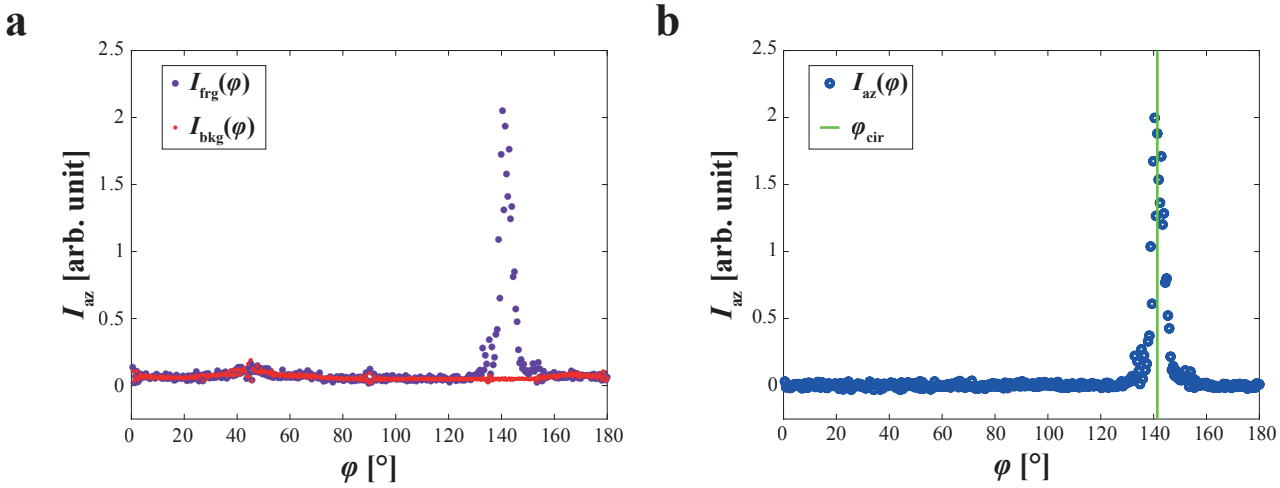

Figure 3.20: Illustration of the circular mean method. a) Azimuthal intensity profiles, from radial integration of the foreground scattering pattern (purple) and of the background scattering pattern (red). b) Background-subtracted azimuthal intensity profile (blue) and its circular mean value (green line).

In order to compare the three methods, we apply them to the same SAXS scan, performed

at ID13, ESRF during the September 2020 experiment. The scan was performed on freeze-dried vim -/- + hDes R406W cells, with a 0.5 µm step size in both directions and 1.4 ms exposure time, in fast scanning mode. The dark field contrast image of the analyzed cell is shown in Figure 3.21a, and the positions used as background (empty regions without cellular material) are shown in blue in Figure 3.21e. All of the background scattering patterns belonging to the same horizontal line of the scan (same vertical position of the sample) are averaged together (simple average), so that a different average background pattern is obtained for each line. All the background subtraction steps described above for the three different methods are always carried out line-by-line, that is, for a given scattering pattern being analyzed, the corresponding background scattering pattern is the one belonging to the same horizontal line. All the scattering patterns of the scan are analyzed, including the background ones, as a control: for the results of the analyses to be meaningful, we expect to see differences between the cellular body and the empty regions. The anisotropy values of the background, in particular, should help in establishing a threshold to distinguish isotropic (or nearly isotropic) scattering patterns, for which the orientation value is not relevant, from the scattering patterns for which an orientation value is relevant.

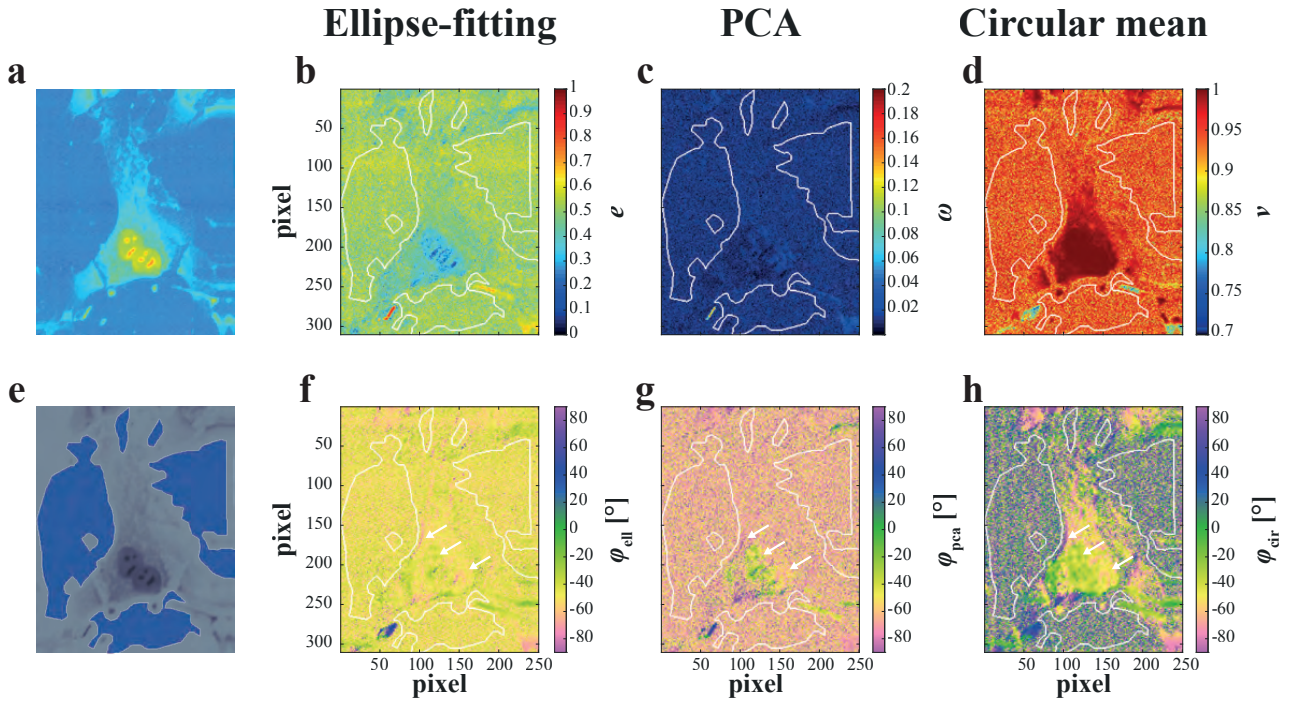

Figure 3.21: Comparison of the different orientation analyses. a) Dark field contrast image of the analyzed scan. b) Eccentricity map obtained with the ellipse-fitting method. c) ω map obtained with the PCA. d) Circular variance map obtained with the circular mean method. e) Regions of interest of the analyzed scan: the dark field contrast image shown in a is presented here in gray scale; the positions used as background are shown in blue. f) Orientation map obtained with the ellipse-fitting method. g) Orientaion map obtained with the PCA. h) Orientation map obtained with the circular mean method. The white arrows in the orientation maps f-h point out examples of similar orientations detected by all three methods at the same position.

The eccentricity and orientation maps from the ellipse-fitting analysis are shown in Figure 3.21b, f, respectively; the ω and orientation maps from the PCA are shown in Figure 3.21c, g, respectively; and the variance and orientation maps from the circular mean analysis are shown in Figure 3.21d, h, respectively. In all of the maps, the background region is outlined in white; the orientation maps are all depicted in the same color map, that identifies $-90°$ and

90°, as they represent the same orientation. All orientation maps represent real space orientations, thus they show angles perpendicular to the orientation of the corresponding scattering patterns.

The first observation we can make when seeing these results is that, regardless of the method used, all of the positions in the scan appear to be very isotropic. Additionally, in the anisotropy maps (Figure 3.21b-d), the regions belonging to the cellular body are either indistinguishable from the background region or more isotropic than the background region: therefore, the corresponding orientation values are not very meaningful, as the "strength" of the local orientation, quantified by the values e, ω or v, is very low. The most isotropic part of the cell appears to be the nuclear region. The nucleus is denser than the cytoplasm, that is, it contains more material: keeping in mind that the SAXS signal is the average result of the scattering from everything inside the irradiated volume, this means that the signal from the nucleus is an average over a larger number of scatterers than the cytoplasm. Consequently, only a strong anisotropy within the scale of the irradiated volume would show in the nuclear signal; the similarity between the cytoplasm and the background e, ω and v values is probably due to the faintness of the cytoplasmic signal.

As the scattering patterns appear to be, for the most part, at least as isotropic as the background, the values shown in the orientation maps (Figure 3.21f-h) should be regarded as not particularly significant. However, it is striking how the results of the circular mean approach show differences between the empty membrane regions, where the angles seem to be randomly distributed, and the cellular regions, where groups of adjacent positions with similar orientations appear. In contrast, the other two methods seem unable to detect differences between the background and the cellular morphology, excluding few regions of the nucleus and of the cellular membrane (white arrows). Importantly, these regions where the cellular orientation emerges as different from the background orientation show similar angular values regardless of the method used.

Comparison of different exposure times

As observed above, the limited effectiveness of the orientation analyses (*i. e.* the similarity of the results obtained for empty membrane and cell, and the high isotropy of all of the scattering patterns) might stem from the weakness of the signal, in particular the cytoplasmic signal. In order to check if a longer exposure time (meaning better photon statistics) could improve the signal, we investigate the orientation and anisotropy of scans performed with the same step size but different exposure times.

The scans are obtained at ID13, ESRF during the April 2017 experiment, on freeze-dried NIH-3T3 cells on a silicon nitride window. A 2 µm step size is used in both directions; four scans are performed on adjacent regions of the same sample with increasing exposure times: 5 ms, 10 ms, 20 ms and 100 ms. The orientation analysis is carried out using the circular mean method, as it seems to perform best with our type of data, being the only method that yields an orientation map where the cellular body can be distinguished from the background. Prior to application of the circular mean method, the dark field contrast image of each scan is segmented into background and foreground using a local intensity threshold (that is, we use Matlab Image Processing Toolbox `adaptthresh()` function, with the sensitivity parameter set at 0.6 and the neighborhood parameter set at $[35, 35]$), without any further mask refinement (see also the "Determination of the optimized exposure time" in the Supporting Information of [111]). For each horizontal line in the scan, the average background scattering pattern is determined as the simple average of all the background scattering patterns belonging to that line. The foreground region of each scan is outlined in white in each of the anisotropy and orientation maps presented in Figure 3.22.

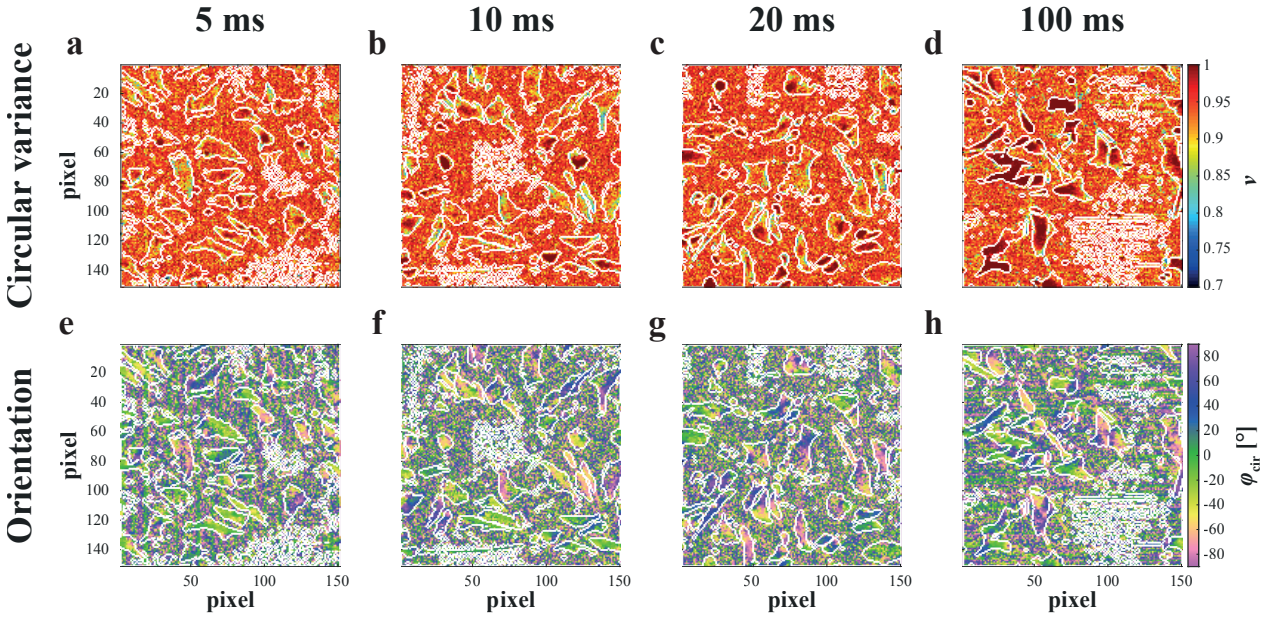

Figure 3.22: Comparison of orientation analysis results for different exposure times. Circular variance map for a) 5 ms exposure, b) 10 ms exposure, c) 20 ms exposure, d) 100 ms exposure. Orientation map for map for e) 5 ms exposure, f) 10 ms exposure, g) 20 ms exposure, h) 100 ms exposure.

Independent of the exposure time, the circular variance maps (Figure 3.22a-d) display large values, meaning that most of the scattering patterns are isotropic or nearly isotropic. Moreover, it is very difficult to distinguish foreground and background by only looking at the circular variance maps. A notable exception is represented by a few very intensely "red" cells, *i. e.* cells displaying variances very close to one. This seems to be particularly evident for the longest exposure time, 100 ms (Figure 3.22d). Indeed, if we count the number N_1 of occurrences of $v = 1$ in the foreground region of each variance map, and divide the count by the total number N_{tot} of pixels in the foreground region, we find that the fraction $f_1 = N_1/N_{\text{tot}}$ of $v = 1$ in the foreground increases with increasing exposure time, as shown in Table 3.9. Table 3.9 also shows the ninth decile D_9 of each foreground v distribution, *i. e.* 10 % of the distribution is larger than or equal to D_9. D_9 also increases with increasing exposure time, meaning that the cells display larger and larger circular variance values as the exposure time grows longer. We take this to mean that either the cells are very isotropic within the irradiated volume, and we are only able to see this properly with long exposure times as the signal is too faint otherwise, or the longest exposure times cause more severe radiation damage, in the form of a destruction of local order in the sample, that emerges here as increased isotropy.

Table 3.9: Fraction f_1 of circular variance equal to 1 and ninth decile D_9 of the circular variance distributions for the foregrounds of Figure 3.22a-d.

Exposure time [ms]	f_1	D_9
5	0.28 %	0.979
10	1.05 %	0.981
20	2.07 %	0.990
100	7.29 %	1.000

Analogously to Figure 3.21h, the orientation maps in Figure 3.22e-h display a seemingly

random background and a distinguishable, non-random foreground.

As the cells appear to be at least as isotropic as the background, if not more, we cannot guarantee that the orientation values are well defined, therefore we decided not to use the orientation analysis to compare different cell lines.

3.2.5 Discussion

The capability of scanning SAXS to provide wide "overview images" of the samples is employed to examine how the cell area and the intensity scatterd by a cell are distributed within one cell sample. The total cell intensity distributions of the vim -/- and vim -/- + hDes R406W scans are characterized by a long tail of larger values, suggesting that these cell lines possess a larger variability than vim -/- + hDes WT cells. In the case of vim -/- cells, this could just be an effect of the smaller number of cells examined (see Table 3.5). However, it is not unreasonable to suggest that the presence of a well developed network of intermediate filaments could "stabilize" the cell properties, resulting in samples less variable in size and density, which would imply a smaller variability in the total scattered intensity. The differences in the distributions for the two vim -/- + hDes WT samples are unlikely due to differences in the sample preparation, as all the sample preparation steps for these two samples were performed on the same days in the same conditions. Nevertheless, slight variations cannot completely be ruled out: for instance, a pipetting error might have changed the number of cells initially deposited on the silicon nitride membrane, or a small difference in the fixation time could have affected the samples. The differences in scattered intensity might also be due to differences in the scan conditions: as an example, it is possible that dividing the intensity by the median intensity value of the background of each line is not sufficient to correct for differences in the intensity of the incoming beam. It is worth noting that, during the October 2018 experiment, the beam was slightly unstable and frequent realignments of the optical elements upstream of the sample were necessary. Regardless of their cause, the differences between the two vim -/- + hDes WT scans suggest that we cannot conclusively attribute the differences among the other scans to properties of the cell lines as a whole.

Confocal imaging of vim -/-, vim -/- + hDes WT and vim -/- + hDes R406W cells reveals the formation of seemingly normal desmin networks in vim -/- + hDes WT cells, while no network is visible in vim -/- + hDes R406W cells. Herrmann *et al.* [93] have observed an accumulation of desmin signal around the nucleus and in the cellular periphery of vim -/- + hDes R406W cells. Our results are in agreement with those observations (Figure 3.11b). However, the desmin signal from our vim -/- + hDes R406W cells is so low, that at the same conditions some signal from the vim -/- cells is also visible, particularly as bright spots in the nucleus (Figure 3.12c, f). Conversely, the cellular periphery of vim -/- cells is barely visible. Thus, we elect to limit the analysis of SAXS patterns to the ones belonging to the cellular periphery.

The power law fits of the average intensity profiles of the cellular periphery yield exponents lower than -4, *i. e.* faster decays than those predicted by Porod's law. Porod's law is the name of equation 3.6 when $\alpha = -4$ for large q values. It describes the terminal part of the radial intensity profile for three-dimensional scatterers with smooth interfaces [30, 32, 35, 151]. As discussed in Section 1.1, when Porod's law is valid, Porod's constant K is directly proportional to the surface area of the interface between scatterers and air and to the electron density contrast squared (equation (1.21)). If the differences in the K values obtained from the fit were only due to the surface area contribution, while the electron density remained constant within the irradiated volume, then it would make sense for the vim -/- + hDes R406W K value to be larger than that of the vim -/- + hDes WT cells: a set of scatterers organized in an interconnected network of filaments would expose a smaller surface area than the same quantity

of scatterers "broken up" into small aggregates. However, this interpretation is very far-fetched, as all exponents are significantly different from -4. Additionally, comparisons between K values should not be attempted when there are doubts on the validity of the intensity normalization.

Three methods for the determination of anisotropy and orientation of the scattering patterns are compared. The cellular orientations yielded by the circular mean method are significantly different from the orientations of the background positions, so the circular mean method seemingly outperforms the other two methods. The reason resides in the different background subtraction strategy employed by this method. The background subtraction of 2D scattering pattern treats each pixel of the detector singularly. This can prove to be ineffective when the scattering signal is low and noisy and the background is anisotropic: for instance, after background subtraction an anisotropic gray halo, most probably not belonging to the cell signal, is still present in Figure 3.18b. Thanks to radial integration, this anisotropy is captured in both $I_{\mathrm{bkg}}(\varphi)$ and $I_{\mathrm{frg}}(\varphi)$, appearing as a small peak between 40° and 60° in both curves of Figure 3.20a. In this case, the background subtraction effectively removes the peak (Figure 3.20b). All cellular positions are quite isotropic according to all of the methods used. This probably means that local preferred orientations, if present, are averaged out in the irradiated volume of the cells, which is in the order of $1\,\mu\mathrm{m}^3$. In other words, the insensitivity to local orientation is most likely caused by the beam size rather than its intensity. This is confirmed by the fact that increasing the exposure time does not reduce the isotropy of the signal.

3.3 EBS upgrade

The measurements taken in September 2020 were performed after the "Extremely Brilliant Source" (EBS) upgrade of ESRF. According to the ESRF website [152], the upgrade increased the brilliance and coherence of the primary beam by a factor of 100. Effectively, this resulted in our particular case in approximately a two-fold increase in the photon flux, with the same photon energy and a comparable beam size; the exact numerical values are given in Table 2.1. In order to compare this new setup with the previous one, vim -/- + hDes R406W cells grown on a silicon nitride membrane and freeze-dried were scanned with a step size of 0.5 µm in both scan directions and an exposure time of 1.4 ms per position. The radiation dose was therefore 7.4×10^6 Gy, very similar to that employed in the window-wide scans of October 2018 (7.6×10^6 Gy). The vim -/- + hDes R406W sample was prepared on the same day and in the same conditions as the vim -/- + hDes R406W sample measured in October 2018, described in Section 3.2. For the sake of simplicity, the October 2018 scan will be referred to as the "earlier scan", the September 2020 scan as the "later scan". At the moment of acquisition, the 2020 window-wide scan was divided into 42 square sub-scans comprising 401 × 401 scan position each, in order to facilitate the data transfer from the detector to the storage. Without this strategy, the detector would often crash before scan completion.

3.3.1 Comparison of scanning SAXS of freeze-dried cells before and after the EBS upgrade

The intensity of the dark field contrast image of each square sub-scan is normalized with the background median intensity, as described in Section 3.2. The dark field contrast image of the complete window is segmented into cells and background, and each cell is divided into three intensity levels, in the same way as reported above. The results are shown in Figure 3.23. The dark field contrast image in Figure 3.23a is compared with the vim -/- + hDes R406W cells of the earlier scan, shown in Figure 3.13c (the color map is the same). The dark field contrast image of Figure 3.23a is more "fragmented" than the other image, with missing vertical and horizontal segments. The missing vertical segments are positions at the end of each horizontal line of a sub-scan: for a minor bug in the software controlling the data acquisition, the detector keeps acquiring scattering patterns while the sample motors are decelerating at the end of the line. This causes the inclusion of a few unwanted scattering patterns into the data set that need to be excluded from the analysis. The missing horizontal segments occur when a horizontal line in a sub-scan does not contain any background position. In such a circumstance, the intensity normalization fails and the horizontal line must be excluded from the analysis.

Despite these missing portions, the distributions of cell areas of the two samples are very similar, as can be seen in Figure 3.24a. While the earlier scan (red) presents a longer "tail" of particularly large outliers, the interquartile ranges and median values of the two distributions resemble each other very much. A two-sample Kolmogorov-Smirnov test [138] yields a p-value of 0.64 for the null hypothesis that the two data sets have the same distribution, confirming that the two distributions most likely represent the same population.

Conversely, the average cell intensity distributions are very different from each other (Figure 3.24b), with the average cell intensities of the earlier scan (red) much larger than those of the later scan (blue). This fact suggests that a better intensity normalization strategy is needed than the one used here, as such inconsistencies among different scans prevent any intensity comparison.

Average radial intensity curves can also be computed, similarly to what is presented in Section 3.2.3, separately for the three intensity levels shown in Figure 3.23b and Figure 3.15c (Figure 3.25, red, green and blue symbols for the high, medium and low intensity regions,

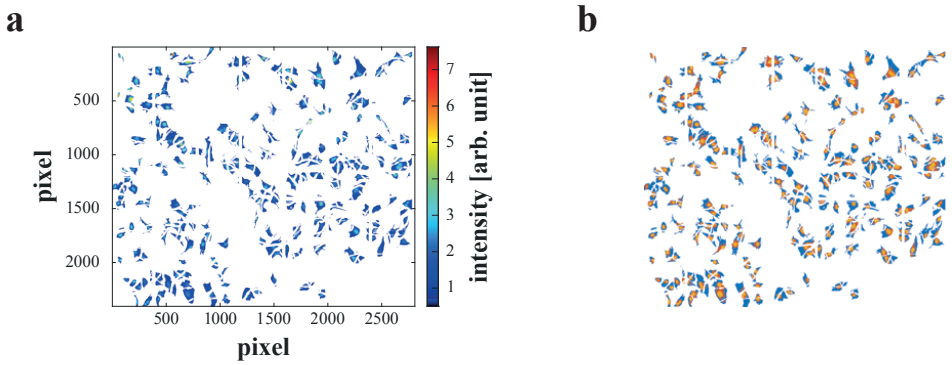

Figure 3.23: Dark field contrast image and cellular regions of interest of the later window-wide scan. a) Dark field contrast image (183 cells). b) Cellular regions of interest for the dark field contrast image shown in a. The high intensity region is shown in yellow, the medium intensity region in orange and the low intensity region in blue. Each pixel represents a different scan position, so it equals 0.5 µm × 0.5 µm.

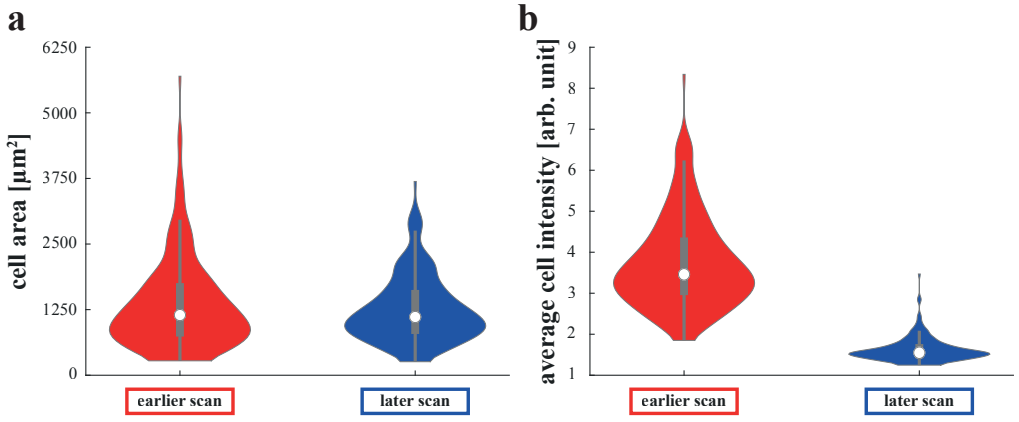

Figure 3.24: Area and scattered intensity distributions of the cells shown in Figure 3.13c and Figure 3.23a. a) Violin plots of the distributions of cell area. b) Violin plots of the distributions of average cell scattered intensity. The median values are shown in the violin plots [135, 136] by white circles, while the gray boxes indicate the interquartile range and the gray whiskers mark the interval outside of which the data are considered outliers by Tukey's criterion [137].

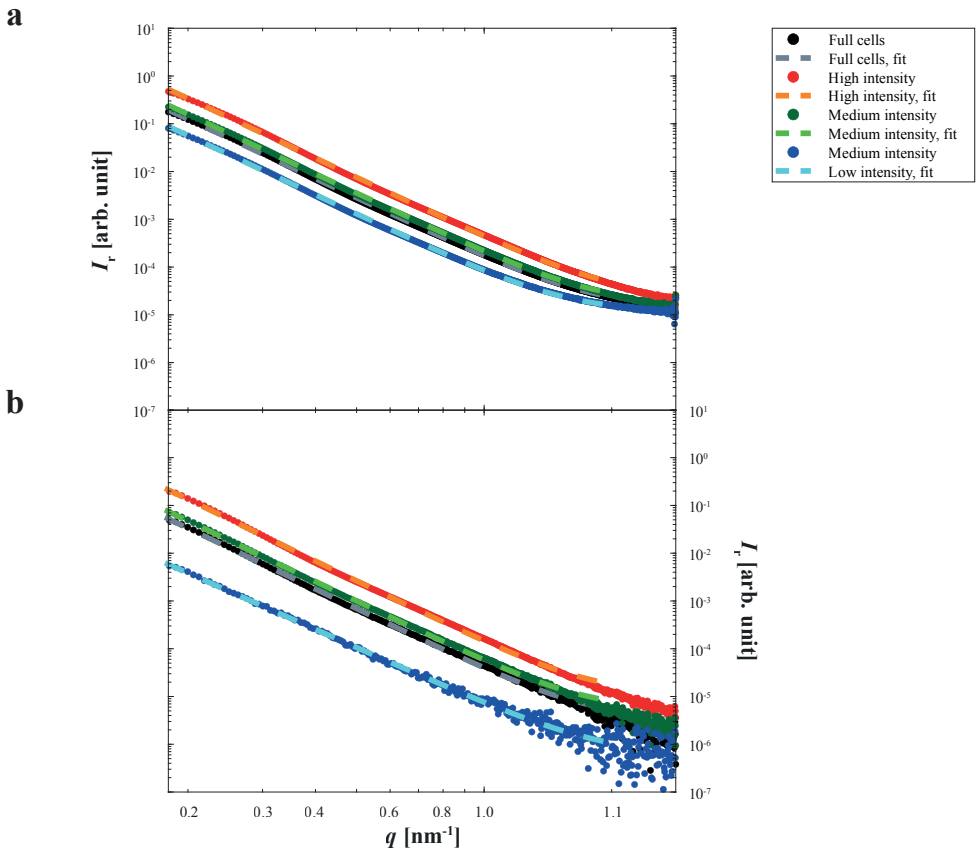

Figure 3.25: Radial intensity decay for matching regions of interest of the samples shown in Figure 3.13c and Figure 3.23a. a) Average radial intensity curves and power law fits for $q \in [0.1798, 1.925]$ nm^{-1}, earlier scan (Figure 3.13c). b) Average radial intensity curves and power law fits for $q \in [0.1798, 1.925]$ nm^{-1}, later scan (Figure 3.23a).

respectively) or for all the cells in Figure 3.23a and Figure 3.13c (Figure 3.25, black symbols). The power law decay of the average radial intensity curves is fitted with equation (3.6). Because of the intensity mismatch highlighted by Figure 3.24b, a comparison of the different K values would be meaningless. However, the shape of the curve, described by the value of the exponent α, can still be examined. We expect similar exponents for curves corresponding to the same region of interest in the two different samples, represented by the same color in Figure 3.25a, b for the earlier and later scan, respectively. The fit curves are plotted as dashed lines. The corresponding α values are listed in Table 3.10. From their comparison, it is evident that exponents of corresponding curves do not perfectly match. Therefore, the differences in the two scans cannot be fully attributed to a faulty intensity normalization: differences are also present in the steepness of the radial intensity decay, with the later scan showing a steeper decay for every region of interest except for the low intensity region, where the opposite is true. Steeper decays have been associated with a lower radiation damage, that is, with a reduction of the radiation dose achieved by either attenuating the beam or cryoprotecting the sample [65]. While the dose in the later experiment was indeed smaller than in the earlier one, the difference was small (roughly, 3 %), so the lower α values are not necessarily due to a smaller radiation damage.

Table 3.10: Power law exponents α for the fits of the curves shown in Figure 3.25. Fitting range: $[0.1798, 1.925]$ nm^{-1}.

Region of interest	Earlier scan	Later scan
Cell	-4.142 ± 0.008	-4.234 ± 0.009
High intensity	-4.151 ± 0.009	-4.287 ± 0.011
Medium intensity	-4.146 ± 0.007	-4.220 ± 0.009
Low intensity	-4.126 ± 0.008	-3.917 ± 0.010

Interestingly, the curves obtained from the later scan (Figure 3.25b) appear to be noisier than those obtained from the earlier scan, particularly in their terminal part. It is possible that the September 2020 setup offered a poorer contrast than the October 2018 setup. It should also be noted that, while the computation of the radial intensity curves was performed with as similar a procedure as possible for the two scans, a few differences were inevitably introduced by the division in sub-scans of the later scan. In particular, for each horizontal line of the earlier scan, 300 random background positions were averaged to obtain the average background radial intensity for that line. To be consistent with this method, for each horizontal line of each sub-scan of the later measurement 40 random background positions were averaged to obtain the average background radial intensity for that line. The number 40 was chosen because the total scan is horizontally divided into 7 sub-scans, and $300/7 \approx 40$. This different background statistics might explain, at least in part, why the later measurements present noisier background-subtracted radial intensity curves. Additionally, while the two samples are as similar to each other as possible in terms of their preparation, the sample measured in September 2020 was kept in storage for about a year longer than the other sample before the measurements took place, so modifications of the sample due to prolonged storage cannot be excluded.

3.3.2 Scanning SAXS on fixed-hydrated cells

In September 2020, chemically fixed, hydrated cells were also measured. The samples were prepared as detailed in Section 2.2, where a description of the wet sample chamber can also be found. As the access to ESRF was restricted due to the COVID-19 pandemic, the mea-

surements at the synchrotron took place remotely, meaning that we monitored the experiment via videoconference, with limited remote access to the computer system of the control hutch, and all on-site operations had to be performed by the beamline responsible for ID13, Manfred Burghammer (ESRF, Grenoble). Therefore, all samples had to be shipped to the ESRF. In order prevent the cells from drying, sample chambers were fully assembled and completely immersed in ultra pure water. The chambers were taken out of the water and their exteriors were carefully dried only just before X-ray measurements, meaning that they remained stored in water for up to two weeks. The exterior part of the silicon nitride membranes of the samples was partially covered in some sort of dirt when they were measured at the synchrotron, that was not present when the samples were shipped. Reportedly, the dirt was visible by naked eye, it could be partially removed by very careful blotting and rinsing and different samples carried different amounts of dirt.

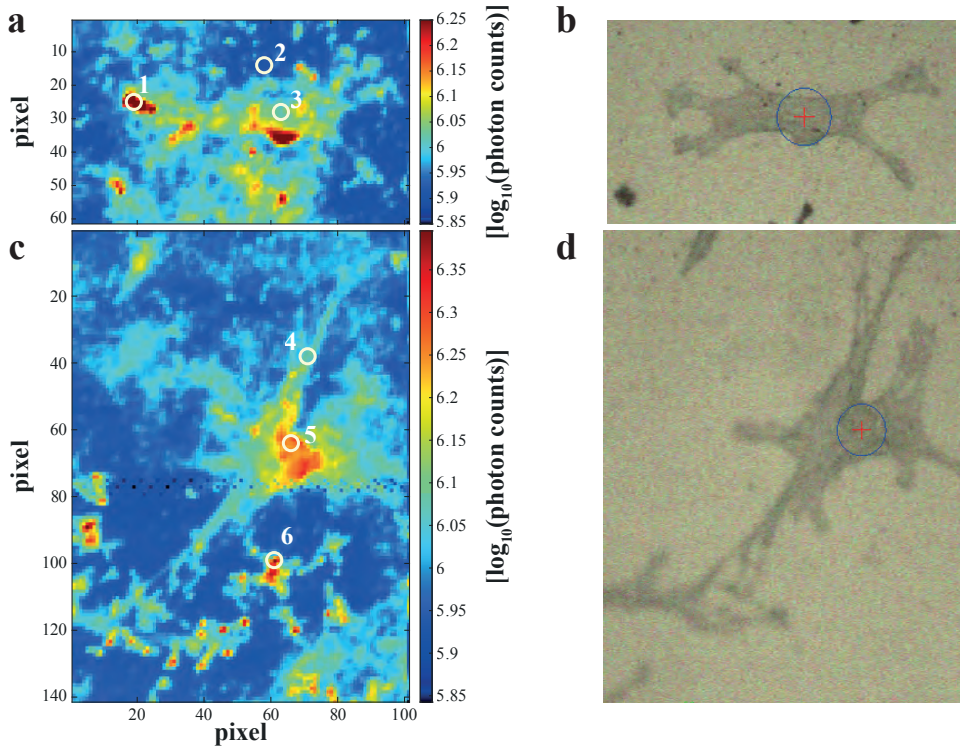

Figure 3.26: Examples of hydrated cells measured in September 2020. a) Dark field contrast image of a fixed-hydrated vim -/- cell on a silicon nitride membrane. Pixel size: 1 µm × 1 µm. The white circles are centered on positions whose scattering patterns are shown in Figure 3.27. b) Optical microscopy image of the cell shown in a. c) Dark field contrast image of two fixed-hydrated vim -/- cells on a silicon nitride membrane. Pixel size: 1 µm × 1 µm. The white circles are centered on positions whose scattering patterns are shown in Figure 3.27. d) Optical microscopy image of the cells shown in c.

Two examples of dark field contrast images from scanning SAXS of the cleanest sample we could measure (containing vim -/- cells) are shown in Figure 3.26, along with optical microscopy images taken with the inline microscope prior to scanning the sample. The step size of the scans is 1 µm in both directions and the exposure time is 50 ms, corresponding to a radiation dose of 6.6×10^7 Gy. The dirt is visible in the optical micrographs (Figure 3.26b, d) as dark spots. The dark field contrast images (Figure 3.26a, b) show cellular signal disturbed by many bright spots of various shapes. It is difficult to tell if the dark spots in the optical micrographs correlate with the bright spots in the dark field contrast image, so the unwanted signal might come from the external dirt, from something happening inside of the chamber, or from a combination of

the two.

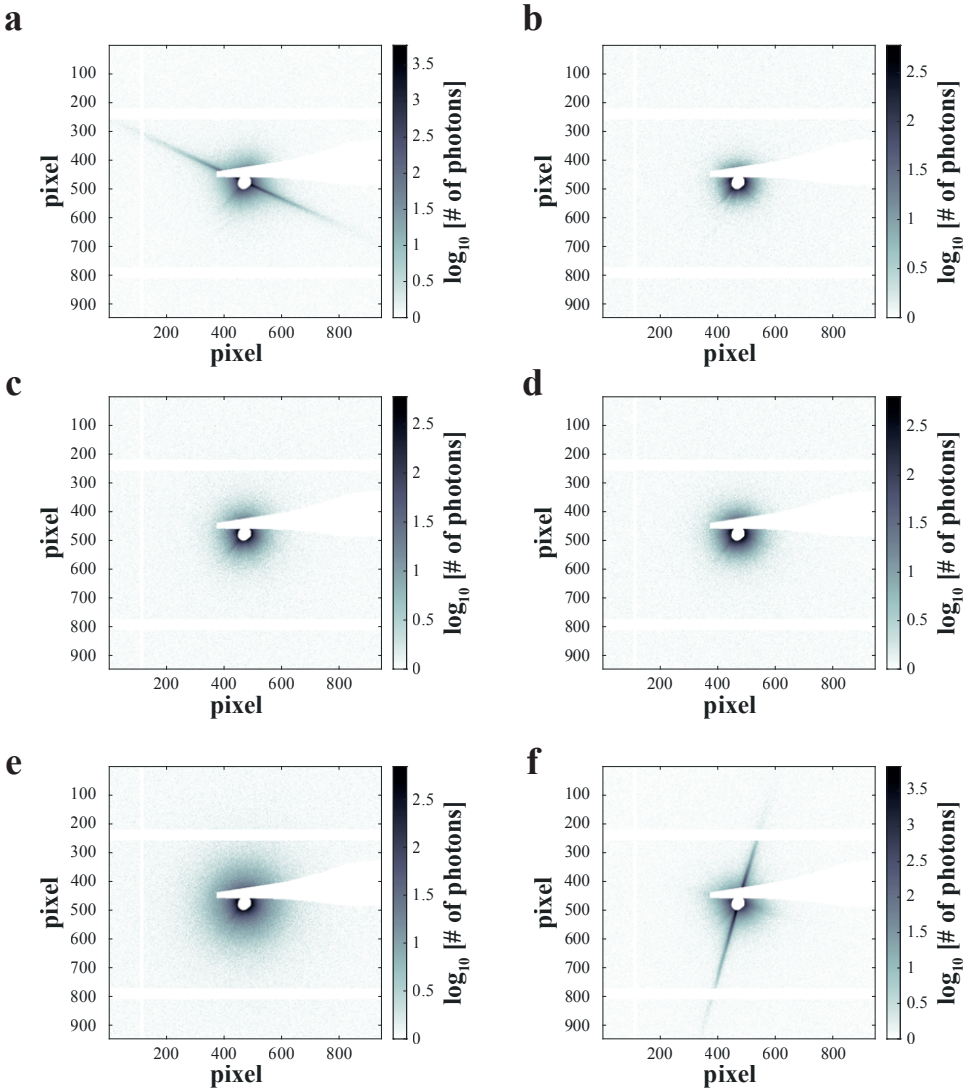

Figure 3.27: Examples of scattering pattern from SAXS scans of hydrated cells. a) Scattering pattern for position 1 in Figure 3.26a (dirt). b) Scattering pattern for position 2 in Figure 3.26a (background). c) Scattering pattern for position 3 in Figure 3.26a (cytoplasm). d) Scattering pattern for position 4 in Figure 3.26c (cytoplasm). e) Scattering pattern for position 5 in Figure 3.26c (nucleus). f) Scattering pattern for position 6 in Figure 3.26c (dirt).

The scattering patterns corresponding to the positions marked in the dark field contrast images of Figure 3.26 are shown in Figure 3.27. As reasonably expectable, the background (Figure 3.27b) and cell (Figure 3.27c, d and e) scattering patterns are fairly isotropic, with the nucleus (Figure 3.27e) scattering more than the cytoplasm (Figure 3.27c, d) and the cytoplasm more than the background. In contrast to this finding, the bright spots correspond to scattering patterns (Figure 3.27a, f) presenting one or more well-defined streaks, suggesting the presence of a preferred orientation in the scatterers that originated them.

3.3.3 Discussion and outlook

From the results obtained for the freeze-dried cells, it is evident that a better way than the median background intensity-based normalization is needed to account for differences in the

experimental setup and particularly in the incident X-ray beam intensity, in order to satisfactorily compare different scans. An examination of the radial intensity decays reveals that, regardless of the absolute value of the intensity, the two scans are different, both in the quality of the curves, that appear less noisy for the scan performed before the EBS upgrade, and in the steepness of their decay, that is found to be faster for the scan performed after the upgrade. It should be noted that the apparent lower quality of the later scan does not necessarily imply a lower quality of the X-ray beam. Our measurements were among the first performed after the upgrade, so the setup was not necessarily optimized to fully take advantage of the new X-ray features. The experiment was carried out remotely, meaning that one person alone had to materially set up the beam, handle the samples and launch the scans, thus the time devoted to each operation was inevitably reduced. Additionally, the beamline control software had just migrated from SPEC [153] to BLISS [154] and not all functionalities were running smoothly. Moreover, the samples were shipped from Göttingen to Grenoble, increasing the chance of a diminished sample quality. The problems with the hydrated samples are most likely related to the shipment, or rather from the necessity to have the samples already mounted in the wet sample chamber for several days before measuring them. The dirt observed on the samples might come to the aluminum frames of the chamber, or from the silicone glue used to seal the PDMS spacers, or even from the boxes that contained the chambers in water during transportation. Further experiments are necessary to determine and eliminate the cause of this inconvenience. Nevertheless, the shape of the scanned cells can be distinguished in the dark field contrast images. An orientation analysis similar to that presented in Section 3.2.4 could be used in the future to find the unwanted strongly scattering positions of hydrated cells, so that they can be excluded from further analysis. The remaining scattering patterns might be already good enough to learn something about the scattering signal from fixed cells in an aqueous environment.

Chapter 4

Summary, outlook and conclusion

The results presented in this work prove that high-throughput in scanning SAXS of adherent mammalian cells can be achieved. In a single experiment, we manage to image an unprecedented number of cells, in the order of hundreds instead of tens. This auspicious outcome has been attained thanks to the continuous movement of the sample stage during data acquisition combined with short exposure times. The choice of short exposure times presents a double advantage: not only does it reduce the overall acquisition time, contributing to the realization of fast scanning SAXS, but it also decreases the radiation dose applied to the sample. As a high radiation dose causes severe radiation damage [55, 155–157], low-dose techniques are always sought after. Within scattering- or diffraction-based hard X-ray imaging techniques, scanning SAXS is the most dose-demanding, with typical doses for biological samples of few 10^8 Gy, as opposed to the doses necessary for ptychography (about 10^3 Gy – 10^6 Gy) or holography (on the order of 10^3 Gy only) [158]. In our experiments, we bring the radiation dose of scanning SAXS down to 10^6 Gy – 10^7 Gy, thus being comparable with high-dose ptychography. The downside of low radiation doses is the loss in contrast: a minimum dose is required to be able to distinguish the signal from the background [27]. A way to improve the contrast is freeze-drying the samples: the electron density of cellular material is similar to that of water, so eliminating the aqueous content from the sample increases the difference between the electron density of the sample (lyophilized cellular material) and its environment (air). Nevertheless, the radial intensity profiles of unaveraged scattering patterns collected with low exposure times are very noisy, as shown in Figure 3.4. A solution to this problem is the analysis of averaged radial intensity profiles, as discussed in Section 3.1.1, Section 3.2.3 and Section 3.3.1. The high-throughput of fast scanning SAXS allows for averages over large pools of data, resulting in smooth curves and ensuring that all of the cell population is represented.

In order to average scattering patterns or radial intensity profiles belonging to the same cell, or to the same region of interest (e. g. the peripheral cytoplasm or the nucleus), the dark field contrast images of SAXS scans are segmented. Thanks to the negligible scattering of silicon nitride in the energy range and q-range employed, the cells are clearly distinguishable from the empty membrane in membrane-wide dark field contrast images (Figure 3.2, Figure 3.6), as intense objects on a dark background. Our segmentation strategy is therefore based on a local intensity threshold. The size of the neighbourhood used to compute the local threshold is similar to the size of the cells or smaller and we find that the local average intensity works best to detect the cells. Once the cells have been detected, the intensity distribution of each single cell can be divided into three intensity levels using Otsu's method [77] extended to multiple thresholds. The highest intensity level works strikingly well to detect the nucleus of the cell, as it almost always coincides with the nucleus (Figure 3.10). Problems with the segmentation arise when the incident beam intensity substantially varies in time, which is not unlikely during long scans (Figure 3.6). A normalization of the dark field contrast image intensity based on

the median background intensity of each horizontal line of the scan corrects for the temporal variations of the incoming beam intensity (Figure 3.7). Also thanks to a manual refinement, the final result of the segmentation reflects very well the real-life position and shape of the cells in the sample. In the future, the segmentation could be fully automated with the use of neural networks, with the segmentations obtained with our method as training data.

If we interpret the median background intensity value as an estimate for the incident beam intensity, it seems appropriate to use the same kind of correction on the scattering patterns and radial intensity curves, so that they can be compared even when they belong to different scans. With this in mind, we compare three different cell lines, one lacking cytoplasmic intermediate filament proteins (vim -/- cells), one expressing a wild-type desmin network (vim -/- + hDes WT) and one expressing a mutant kind of desmin that tends to form abnormal aggregates instead of networks (vim -/- + hDes R406W). A comparison of the distributions of the dark field intensity scattered by the cells of the different cell lines (Figure 3.14) reveals that the thickness of the cells determines the amount of scattering. Therefore, it would be interesting to combine future scanning SAXS measurements with a mapping of the cell thickness at various points, for example by fluorescence microscopy [159] or by atomic force microscopy [157]. The distributions of the intensity globally scattered by each cell are wider in the case of vim -/- and vim -/- + hDes R406W, suggesting that the presence of a wild-type desmin network reduces cell to cell variability within the same cell line. As cytoplasmic intermediate filament networks are believed to play an important role in the determination of cellular architecture [112], it is conceivable that cells lacking them have more variable structure, resulting in more variable scattering. The averaged intensity profiles of the desmin-expressing cell lines show similar intensity decays, while the radial intensity curve of vim -/- cells decreases more rapidly (Figure 3.16). However, the vim -/- curve presents an anomalous drop at small q values, most likely due to a lack of contrast between this curve and the background. All of the curves are averages over the lowest intensity level region of interest, representing the peripheral cytoplasm: this is the thinner part of the cells, so it scatters the least, particularly in the case of the vim -/- cells, that have the largest incidence of large cells (Figure 3.14), which likely correlates with smaller thicknesses. The larger K values observed for the mutant-expressing cells might be interpreted as a result of the large surface area exposed by the mutant desmin aggregates, although this interpretation would be a consequence of Porod's law, that is not strictly valid in this case (the exponent of the power-law fit is close, but not equal to -4). Additionally, doubts arise on the validity of our intensity normalization, as the intensity distributions and radial intensity profiles of two different samples containing the same cell line (vim -/- + hDes WT cells) do not coincide. These doubts are confirmed by comparing the vim -/- + hDes R406W scan with a scan of a different vim -/- + hDes R406W sample obtained during a different experiment (Figure 3.24, Figure 3.25). While the cell area distributions are compatible with each other, the scattered intensity is not. Therefore, it will be important to monitor the incident X-ray beam intensity at each scan position, if we want to achieve a truly quantitative comparison of scattered intensity for different scans. In the meanwhile, the datasets lacking this information should be only compared using intensity-independent parameters. It is worth noting that the exponents of the power law fits of radial intensity profiles are indicative of the shape, and not the intensity, of the profiles, thus they can be safely compared.

The orientation and anisotropy of scattering patterns are also intensity-independent parameters. We show that a radial integration of the scattering patterns, followed by a computation of the circular mean and variance of the resulting azimuthal intensity curve, works best for the orientation analysis of our low-intensity scattering data. For the most part, our samples turn out to be at least as isotropic as the empty silicon nitride membrane (Figure 3.21), and longer exposure times do not reveal relevant anisotropies. Thus, we conclude that the samples are very isotropic within the irradiated volume of about $1\,\mu m^3$, which justifies our intensive

use of azimuthal integration. Local anisotropies might be present within volumes smaller than $1\,\mu m^3$, thus scanning SAXS of the same kind of sample with a nanofocused beam would be very interesting. The orientation and anisotropy analysis will probably also help in the examination of data from fixed-hydrated samples. As shown in Section 3.3.2 the cell signal is disturbed by some dirt that scatters strongly. The scattering patterns from the dirt are characterized by evident streaks, so a good way to exclude them is a selection on anisotropy values: positions associated with large anisotropy values should be disregarded. Despite this issue, the sample chamber for wet samples is effective in keeping the cells hydrated during X-ray measurements, that can last for as long as six hours. Further development of the chamber design, including a better understanding of the nature of the dirt observed at the synchrotron and its prevention, as well as experimenting with even thinner spacers, could result in the future in a standardized environment for X-ray imaging of hydrated, adherent cells.

On the whole, while low-dose, high-throughput scanning SAXS of adherent cells can be achieved, quantitative characterization of cell populations remains elusive. Nevertheless, our results demonstrate that a quantitative, statistically sound description of cell lines by means of scanning SAXS is within reach and point out the strategies that should be adopted in future developments to take advantage of the full potential of this technique.

Appendix A

Measurements of cell thickness

A confocal microscope (Olympus IX81, equipped with a 40x objective, UPLSAPO40X2, numerical aperture 0.95) is used to measure the average cell thickness of all of the cell lines examined in this work. The cells are grown on glass-bottom Petri dishes (81158; Ibidi GmbH, Gräfelfing, Germany) and fixed with 3.7 % formaldehyde as described in Chapter 2. A negative staining approach is used, meaning that the aqueous environment of the cell, rather than the cell itself, is fluorescent. In particular, we use 20 nm diameter fluorescent beads (FluoSpheres F8888; Invitrogen), diluted 1 : 10 (v/v) in PBS. For the measurements, we scan the sample with a vertical (*i. e.* the direction of the cell thickness) step size of 0.5 µm and an axial resolution of 1.009 µm. The thickness of a cell is defined as the distance between the surface of the cell culture dish (Figure A.1a), where the cell adheres, and the last plane where at least a portion of the nuclear surface is still in focus (Figure A.1d). Thus, it is actually a measurement of maximum thickness.

While the use of fluorescent beads is not optimal (for instance, fluorescent aggregates forming bright spots can be seen in Figure A.1), the mean nucleus thickness of NIH-3T3 fibroblasts, *i. e.* 5.7 ± 0.4 µm, is of the same order of magnitude as the maximum height of a NIH-3T3 fibroblast measured by atomic force microscopy and by a fluorescence displacement technique in Reference [160], that is, about 3.5 µm. Considering our axial resolution of 1.009 µm, the maximum thicknesses of the examined cell lines (Table 2.1) do not display significant differences.

Table A.1: Results of maximum cell thickness measurements.

Cell line	Number of cells	Mean thickness [µm]	Error of the mean [µm]
NIH-3T3	15	5.7	0.4
vim -/-	26	4.8	0.2
vim -/- + hDes WT	41	4.0	0.2
vim -/- + hDes R406W	45	3.76	0.11

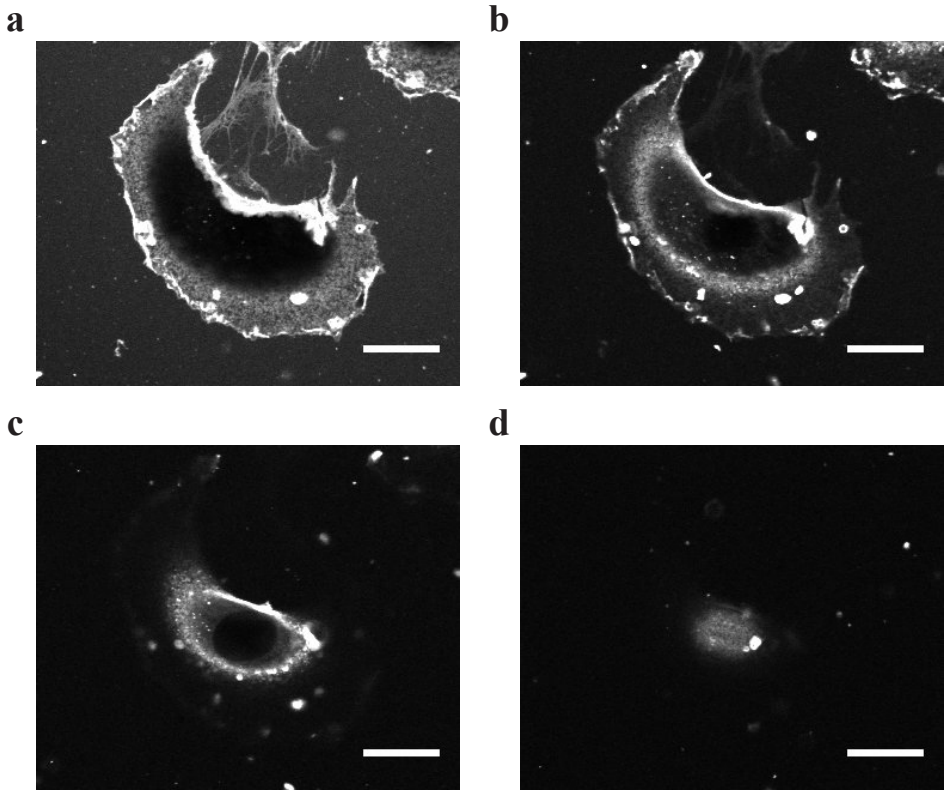

Figure A.1: Example of confocal stack for the determination of the maximum thickness of a NIH-3T3 cell. a) Surface of the cell culture dish. b) 1 µm over the surface of the cell culture dish. c) 3 µm over the surface of the cell culture dish. d) 7 µm over the surface of the cell culture dish. Scale bars: 20 µm

Bibliography

[1] Yoram Louzoun et al. "Modeling complexity in biology". In: *Phys. A* 297.1-2 (2001), pp. 242–252. DOI: 10.1016/s0378-4371(01)00201-1.

[2] Marc H V Van Regenmortel. "Reductionism and complexity in molecular biology". In: *EMBO rep.* 5.11 (2004), pp. 1016–1020. DOI: 10.1038/sj.embor.7400284.

[3] Fulvio Mazzocchi. "Complexity in biology". In: *EMBO rep.* 9.1 (2008), pp. 10–14. DOI: 10.1038/sj.embor.7401147.

[4] L. Pelkmans. "Using Cell-to-Cell Variability–A New Era in Molecular Biology". In: *Science* 336.6080 (2012), pp. 425–426. DOI: 10.1126/science.1222161.

[5] Steven J. Altschuler and Lani F. Wu. "Cellular Heterogeneity: Do Differences Make a Difference?" In: *Cell* 141.4 (2010), pp. 559–563. DOI: 10.1016/j.cell.2010.04.033.

[6] Wendy Weijia Soon, Manoj Hariharan, and Michael P Snyder. "High-throughput sequencing for biology and medicine". In: *Mol. Syst. Biol.* 9.1 (2013), p. 640. DOI: 10.1038/msb.2012.61.

[7] Chen Xu and Zhengchang Su. "Identification of cell types from single-cell transcriptomes using a novel clustering method". In: *Bioinformatics* 31.12 (2015), pp. 1974–1980. DOI: 10.1093/bioinformatics/btv088.

[8] Feng Guo et al. "Single-Cell Virology: On-Chip Investigation of Viral Infection Dynamics". In: *Cell Rep.* 21.6 (2017), pp. 1692–1704. DOI: 10.1016/j.celrep.2017.10.051.

[9] Anne Beghin et al. "Localization-Based Super-Resolution Imaging Meets High-Content Screening". In: *Nat. Methods* 14.12 (2017), pp. 1184–1190. DOI: 10.1038/nmeth.4486.

[10] Csilla Brasko et al. "Intelligent image-based in situ single-cell isolation". In: *Nat. Commun.* 9.1 (2018). DOI: 10.1038/s41467-017-02628-4.

[11] Kyle M. Douglass et al. "Super-Resolution Imaging of Multiple Cells by Optimized Flat-Field Epi-Illumination". In: *Nat. Photonics* 10.11 (2016), pp. 705–708. DOI: 10.1038/nphoton.2016.200.

[12] Robin Diekmann et al. "Chip-Based Wide Field-of-View Nanoscopy". In: *Nat. Photonics* 11.5 (2017), pp. 322–328. DOI: 10.1038/nphoton.2017.55.

[13] A.L. Eberle et al. "High-Resolution, High-Throughput Imaging with a Multibeam Scanning Electron Microscope". In: *J. Microsc.* 259.2 (2015), pp. 114–120. DOI: 10.1111/jmi.12224.

[14] Wenjing Yin et al. "A petascale automated imaging pipeline for mapping neuronal circuits with high-throughput transmission electron microscopy". In: *Nat. Commun.* 11.1 (2020). DOI: 10.1038/s41467-020-18659-3.

[15] Jan-David Nicolas et al. "Scanning X-ray diffraction on cardiac tissue: automatized data analysis and processing". In: *J. Synchrotron Radiat.* 24.6 (2017), pp. 1163–1172. DOI: 10.1107/s1600577517011936.

[16] David Attwood and Anne Sakdinawat. *X-Rays and Extreme Ultraviolet Radiation*. Cambridge University Press, 2016. DOI: 10.1017/cbo9781107477629.

[17] Neville Smith. "Science with Soft X Rays". In: *Phys. Today* 54.1 (2001), pp. 29–34. DOI: 10.1063/1.1349609.

[18] Jinghua Guo. "Synchrotron radiation, soft-X-ray spectroscopy and nanomaterials". In: *Int. J. Nanotechnol.* 1.1/2 (2004), p. 193. DOI: 10.1504/ijnt.2004.003729.

[19] Janos Kirz, Chris Jacobsen, and Malcolm Howells. "Soft X-Ray Microscopes and Their Biological Applications". In: *Q. Rev. Biophys.* 28.01 (1995), p. 33. DOI: 10.1017/s0033583500003139.

[20] Carolyn A Larabell and Keith A Nugent. "Imaging cellular architecture with X-rays". In: *Curr. Opin. Struct. Biol.* 20.5 (2010), pp. 623–631. DOI: 10.1016/j.sbi.2010.08.008.

[21] X M Cheng and D J Keavney. "Studies of nanomagnetism using synchrotron-based x-ray photoemission electron microscopy (X-PEEM)". In: *Rep. Prog. Phys.* 75.2 (2012), p. 026501. DOI: 10.1088/0034-4885/75/2/026501.

[22] Jens Als-Nielsen and Des McMorrow. *Elements of Modern X-ray Physics*. Wiley, 2011. DOI: 10.1002/9781119998365.

[23] Martin D de Jonge and Stefan Vogt. "Hard X-ray fluorescence tomography—an emerging tool for structural visualization". In: *Curr. Opin. Struct. Biol.* 20.5 (2010), pp. 606–614. DOI: 10.1016/j.sbi.2010.09.002.

[24] Yasumasa Takagi et al. "Ambient pressure hard X-ray photoelectron spectroscopy for functional material systems as fuel cells under working conditions". In: *Acc. Chem. Res.* 51.3 (2018), pp. 719–727. DOI: 10.1021/acs.accounts.7b00563.

[25] Anna Regoutz et al. "A novel laboratory-based hard X-ray photoelectron spectroscopy system". In: *Rev. Sci. Instrum.* 89.7 (2018), p. 073105. DOI: 10.1063/1.5039829.

[26] Yijin Liu et al. "Recent advances in synchrotron-based hard x-ray phase contrast imaging". In: *J. Phys. D: Appl. Phys* 46.49 (2013), p. 494001. DOI: 10.1088/0022-3727/46/49/494001.

[27] M.R. Howells et al. "An assessment of the resolution limitation due to radiation-damage in X-ray diffraction microscopy". In: *J. Electron Spectrosc. Relat. Phenom.* 170.1-3 (2009), pp. 4–12. DOI: 10.1016/j.elspec.2008.10.008.

[28] MJ Berger et al. "XCOM: Photon Cross Sections Database, NIST Standard Reference Database 8 (XGAM)". In: *URL http://physics. nist. gov/PhysRefData/Xcom/Text/XCOM.html* (2010).

[29] J H Hubbell. "Review and history of photon cross section calculations". In: *Phys. Med. Biol.* 51.13 (2006), R245–R262. DOI: 10.1088/0031-9155/51/13/r15.

[30] André Guinier and Gérard Fournet. *Small-Angle Scattering of X-Rays*. John Wiley & Sons, 1955.

[31] Otto Glatter and Otto Kratky, eds. *Small-Angle X-Ray Scattering*. Academic Press, 1982.

[32] W. Ruland. "Small-angle scattering of two-phase systems: determination and significance of systematic deviations from Porod's law". In: *J. Appl. Crystallogr.* 4.1 (1971), pp. 70–73. DOI: 10.1107/S0021889871006265.

[33] Aurélien Gourrier et al. “Scanning Small-Angle X-Ray Scattering Analysis of the Size and Organization of the Mineral Nanoparticles in Fluorotic Bone Using a Stack of Cards Model”. In: *J. Appl. Crystallogr.* 43.6 (2010), pp. 1385–1392. DOI: 10.1107/s0021889810035090.

[34] P. Debye and A. M. Bueche. “Scattering by an Inhomogeneous Solid”. In: *J. Appl. Phys.* 20.6 (1949), pp. 518–525. DOI: 10.1063/1.1698419.

[35] G. Porod. “Die Röntgenkleinwinkelstreuung von dichtgepackten kolloiden Systemen”. In: *Kolloid-Z.* 124.2 (1951), pp. 83–114. DOI: 10.1007/bf01512792.

[36] P. Debye, H. R. Anderson, and H. Brumberger. “Scattering by an Inhomogeneous Solid. II. The Correlation Function and Its Application”. In: *J. Appl. Phys.* 28.6 (1957), pp. 679–683. DOI: 10.1063/1.1722830.

[37] P. Fratzl et al. “Position-Resolved Small-Angle X-Ray Scattering of Complex Biological Materials”. In: *J. Appl. Crystallogr.* 30.5 (1997), pp. 765–769. DOI: 10.1107/s0021889897001775.

[38] S. Rinnerthaler et al. “Scanning Small Angle X-ray Scattering Analysis of Human Bone Sections”. In: *Calcif. Tissue Int.* 64.5 (1999), pp. 422–429. DOI: 10.1007/pl00005824.

[39] N.P Camacho et al. “Complementary information on bone ultrastructure from scanning small angle X-ray scattering and Fourier-transform infrared microspectroscopy”. In: *Bone* 25.3 (1999), pp. 287–293. DOI: 10.1016/s8756-3282(99)00165-9.

[40] I. Žižak et al. “Investigation of bone and cartilage by synchrotron scanning-SAXS and -WAXD with micrometer spatial resolution”. In: *J. Appl. Crystallogr.* 33.3 (2000), pp. 820–823. DOI: 10.1107/s0021889800001321.

[41] Mathias Hauge Bünger et al. “Nanostructure of the neurocentral growth plate: Insight from scanning small angle X-ray scattering, atomic force microscopy and scanning electron microscopy”. In: *Bone* 39.3 (2006), pp. 530–541. DOI: 10.1016/j.bone.2006.03.013.

[42] Aurelien Gourrier et al. “Scanning X-ray imaging with small-angle scattering contrast”. In: *J. Appl. Crystallogr.* 40.s1 (2007), s78–s82. DOI: 10.1107/s0021889807006693.

[43] C. Giannini et al. “Scanning SAXS–WAXS microscopy on osteoarthritis-affected bone – an age-related study”. In: *J. Appl. Crystallogr.* 47.1 (2013), pp. 110–117. DOI: 10.1107/s1600576713030215.

[44] Mikael J. Turunen et al. “Evaluation of composition and mineral structure of callus tissue in rat femoral fracture”. In: *J. Biomed. Opt.* 19.2 (2014), p. 025003. DOI: 10.1117/1.jbo.19.2.025003.

[45] W. Tesch et al. “Graded Microstructure and Mechanical Properties of Human Crown Dentin”. In: *Calcif. Tissue Int.* 69.3 (2001), pp. 147–157. DOI: 10.1007/s00223-001-2012-z.

[46] J.H. Kinney et al. “Collagen Orientation and Crystallite Size in Human Dentin: A Small Angle X-ray Scattering Study”. In: *Calcif. Tissue Int.* 69.1 (2001), pp. 31–37. DOI: 10.1007/s00223-001-0006-5.

[47] Sebastian Gaiser et al. “Understanding Nano-Anatomy of Healthy and Carious Human Teeth: a Prerequisite for Nanodentistry”. In: *Biointerphases* 7.1 (2012), p. 4. DOI: 10.1007/s13758-011-0004-8.

[48] Hans Deyhle et al. “Nanostructure of carious tooth enamel lesion”. In: *Acta Biomater.* 10.1 (2014), pp. 355–364. DOI: 10.1016/j.actbio.2013.08.024.

[49] H. S. Gupta et al. "Mineralized Microstructure of Calcified Avian Tendons: A Scanning Small Angle X-ray Scattering Study". In: *Calcif. Tissue Int.* 72.5 (2003), pp. 567–576. DOI: 10.1007/s00223-002-1031-8.

[50] O Bunk et al. "Multimodal x-ray scatter imaging". In: *New J. Phys.* 11.12 (2009), p. 123016. DOI: 10.1088/1367-2630/11/12/123016.

[51] Günther A. Maier et al. "Structural Changes during Plastic Deformation at Crack Tips in PVDF Films: A Scanning X-ray Scattering Study". In: *Macromolecules* 38.14 (2005), pp. 6099–6105. DOI: 10.1021/ma050390f.

[52] L. Leu et al. "Multiscale Description of Shale Pore Systems by Scanning SAXS and WAXS Microscopy". In: *Energy Fuels* 30.12 (2016), pp. 10282–10297. DOI: 10.1021/acs.energyfuels.6b02256.

[53] Viviane Lutz-Bueno et al. "Scanning-SAXS of microfluidic flows: nanostructural mapping of soft matter". In: *Lab Chip* 16.20 (2016), pp. 4028–4035. DOI: 10.1039/c6lc00690f.

[54] T. Sibillano et al. "Interfibrillar packing of bovine cornea by table-top and synchrotron scanning SAXS microscopy". In: *J. Appl. Crystallogr.* 49.4 (2016), pp. 1231–1239. DOI: 10.1107/s1600576716010396.

[55] Jan-David Nicolas, Sebastian Aeffner, and Tim Salditt. "Radiation damage studies in cardiac muscle cells and tissue using microfocused X-ray beams: experiment and simulation". In: *J. Synchrotron Radiat.* 26.4 (2019), pp. 980–990. DOI: 10.1107/s1600577519006817.

[56] Jan-David Nicolas et al. "X-ray diffraction imaging of cardiac cells and tissue". In: *Prog. Biophys. Mol. Biol.* 144 (2019), pp. 151–165. DOI: 10.1016/j.pbiomolbio.2018.05.012.

[57] Jan-David Nicolas et al. "X-ray diffraction and second harmonic imaging reveal new insights into structural alterations caused by pressure-overload in murine hearts". In: *Sci. Rep.* 10.1 (2020). DOI: 10.1038/s41598-020-76163-6.

[58] C Arboleda et al. "Assessing lesion malignancy by scanning small-angle x-ray scattering of breast tissue with microcalcifications". In: *Phy. Med. Biol.* 64.15 (2019), p. 155010. DOI: 10.1088/1361-6560/ab2c36.

[59] C. Giannini et al. "X-ray scanning microscopies of microcalcifications in abdominal aortic and popliteal artery aneurysms". In: *IUCrJ* 6.2 (2019), pp. 267–276. DOI: 10.1107/s2052252519001544.

[60] Cinzia Giannini et al. "Scanning X-ray microdiffraction of decellularized pericardium tissue at increasing glucose concentration". In: *J. Biophotonics* 12.10 (2019). DOI: 10.1002/jbio.201900106.

[61] Francesco Scattarella et al. "Table-top combined scanning X-ray small angle scattering and transmission microscopies of lipid vesicles dispersed in free-standing gel". In: *RSC Advances* 11.1 (2021), pp. 484–492. DOI: 10.1039/d0ra08581b.

[62] Britta Weinhausen et al. "X-ray nano-diffraction on cytoskeletal networks". In: *New J. Phys.* 14.8 (2012), p. 085013. DOI: 10.1088/1367-2630/14/8/085013.

[63] Clément Y. J. Hémonnot et al. "X-rays Reveal the Internal Structure of Keratin Bundles in Whole Cells". In: *ACS Nano* 10.3 (2016), pp. 3553–3561. DOI: 10.1021/acsnano.5b07871.

[64] Marten Bernhardt et al. "X-Ray Micro- and Nanodiffraction Imaging on Human Mesenchymal Stem Cells and Differentiated Cells". In: *Biophys. J.* 110.3 (2016), pp. 680–690. DOI: 10.1016/j.bpj.2015.12.017.

[65] Clément Y. J. Hémonnot et al. "Following DNA Compaction During the Cell Cycle by X-ray Nanodiffraction". In: *ACS Nano* 10.12 (2016), pp. 10661–10670. DOI: 10.1021/acsnano.6b05034.

[66] M Bernhardt et al. "Anisotropic x-ray scattering and orientation fields in cardiac tissue cells". In: *New J. Phys.* 19.1 (2017), p. 013012. DOI: 10.1088/1367-2630/19/1/013012.

[67] Jan-David Nicolas et al. "Combined scanning X-ray diffraction and holographic imaging of cardiomyocytes". In: *J. Appl. Crystallogr.* 50.2 (2017), pp. 612–620. DOI: 10.1107/s1600576717003351.

[68] M. Bernhardt et al. "Correlative microscopy approach for biology using X-ray holography, X-ray scanning diffraction and STED microscopy". In: *Nat. Commun.* 9.1 (2018). DOI: 10.1038/s41467-018-05885-z.

[69] Andrew Wittmeier et al. "Combined scanning small-angle X-ray scattering and holography probes multiple length scales in cell nuclei". In: *J. Synchrotron Radiat.* 28.2 (2021). DOI: 10.1107/s1600577520016276.

[70] Britta Weinhausen and Sarah Köster. "Microfluidic Devices for X-Ray Studies on Hydrated Cells". In: *Lab Chip* 13.2 (2013), pp. 212–215. DOI: 10.1039/c2lc41014a.

[71] Britta Weinhausen et al. "Scanning X-Ray Nanodiffraction on Living Eukaryotic Cells in Microfluidic Environments". In: *Phys. Rev. Lett.* 112.8 (2014), p. 088102. DOI: 10.1103/physrevlett.112.088102.

[72] S. Williams et al. "Measurements of wet metaphase chromosomes in the scanning transmission X-ray microscope". In: *J. Microsc.* 170.2 (1993), pp. 155–165. DOI: 10.1111/j.1365-2818.1993.tb03335.x.

[73] Marius Priebe et al. "Scanning X-Ray Nanodiffraction on Dictyostelium discoideum". In: *Biophys. J.* 107.11 (2014), pp. 2662–2673. DOI: 10.1016/j.bpj.2014.10.027.

[74] Nikhil R Pal and Sankar K Pal. "A review on image segmentation techniques". In: *Pattern Recognition* 26.9 (1993), pp. 1277–1294. DOI: 10.1016/0031-3203(93)90135-j.

[75] Nima Tajbakhsh et al. "Embracing imperfect datasets: A review of deep learning solutions for medical image segmentation". In: *Med. Image Anal.* 63 (2020), p. 101693. DOI: 10.1016/j.media.2020.101693.

[76] Mehmet Sezgin and Bülent Sankur. "Survey over image thresholding techniques and quantitative performance evaluation". In: *J. Electron. Imaging* 13.1 (2004), p. 146. DOI: 10.1117/1.1631315.

[77] Nobuyuki Otsu. "A Threshold Selection Method from Gray-Level Histograms". In: *IEEE Trans. Syst., Man Cybern.* 9.1 (1979), pp. 62–66. DOI: 10.1109/tsmc.1979.4310076.

[78] H. Lee and R.-H. Park. "Comments on "An optimal multiple threshold scheme for image segmentation". In: *IEEE Trans. Sys. Man Cybern.* 20.3 (1990), pp. 741–742. DOI: 10.1109/21.57290.

[79] Derek Bradley and Gerhard Roth. "Adaptive Thresholding Using the Integral Image". In: *J. Graph. Tools* 12.2 (2007), pp. 13–21. DOI: 10.1080/2151237x.2007.10129236.

[80] Robert M. Haralick, Stanley R. Sternberg, and Xinhua Zhuang. "Image Analysis Using Mathematical Morphology". In: *IEEE Trans. Pattern Anal. Machine Intell.* PAMI-9.4 (1987), pp. 532–550. DOI: 10.1109/tpami.1987.4767941.

[81] John C. Russ. *The Image Processing Handbook*. Third Edition. CRC Press, 1999.

[82] Yuta Yamamoto, Yasutoshi Iriyama, and Shunsuke Muto. "Union operation image processing of data cubes separately processed by different objective filters and its application to void analysis in an all-solid-state lithium-ion battery". In: *Microscopy* 65.2 (2015), pp. 191–198. DOI: 10.1093/jmicro/dfv373.

[83] George J. Todaro and Howard Green. "Quantitative studies of the growth of mouse embryo cells in culture and their development into established lines". In: *J. Cell Biol.* 17.2 (1963), pp. 299–313. DOI: 10.1083/jcb.17.2.299.

[84] William A. Wells. "A cell line that is under control". In: *J. Cell Biol.* 168.7 (2005), pp. 988–989. DOI: 10.1083/jcb1687fta1.

[85] Stuart A. Aaronson and George J. Todaro. "Development of 3T3-like lines from Balb/c mouse embryo cultures: Transformation susceptibility to SV40". In: *J. Cell. Physiol.* 72.2 (1968), pp. 141–148. DOI: 10.1002/jcp.1040720208.

[86] John L. Jainchill, Stuart A. Aaronson, and George J. Todaro. "Murine sarcoma and leukemia viruses: assay using clonal lines of contact-inhibited mouse cells". In: *J. Virol.* 4.5 (1969), pp. 549–553. DOI: 10.1128/jvi.4.5.549-553.1969.

[87] Neal G. Copeland and Geoffrey M. Cooper. "Transfection by exogenous and endogenous murine retrovirus DNAs". In: *Cell* 16.2 (1979), pp. 347–356. DOI: 10.1016/0092-8674(79)90011-4.

[88] Emma Colucci-Guyon et al. "Mice lacking vimentin develop and reproduce without an obvious phenotype". In: *Cell* 79.4 (1994), pp. 679–694. DOI: 10.1016/0092-8674(94)90553-3.

[89] Beate Eckes et al. "Impaired mechanical stability, migration and contractile capacity in vimentin-deficient fibroblasts". In: *J. Cell Sci.* 111.13 (1998), pp. 1897–1907.

[90] Beate Eckes et al. "Impaired wound healing in embryonic and adult mice lacking vimentin". In: *J. Cell Sci.* 113.13 (2000), pp. 2455–2462.

[91] Christoph S. Clemen et al. "Desminopathies: pathology and mechanisms". In: *Acta Neuropathol.* 125.1 (2012), pp. 47–75. DOI: 10.1007/s00401-012-1057-6.

[92] Harald Bär et al. "Mutations in Desmin's Carboxy-Terminal "Tail" Domain Severely Modify Filament and Network Mechanics". In: *J. Mol. Biol.* 397.5 (2010), pp. 1188–1198. DOI: https://doi.org/10.1016/j.jmb.2010.02.024.

[93] Harald Herrmann et al. "Dual Functional States of R406W-Desmin Assembly Complexes Cause Cardiomyopathy With Severe Intercalated Disc Derangement in Humans and in Knock-In Mice". In: *Circulation* 142.22 (2020), pp. 2155–2171. DOI: 10.1161/circulationaha.120.050218.

[94] D. Hopwood. "Fixatives and fixation: a review". In: *Histochem. J.* 1.4 (1969), pp. 323–360. DOI: 10.1007/bf01003278.

[95] William J. Howat and Beverley A. Wilson. "Tissue fixation and the effect of molecular fixatives on downstream staining procedures". In: *Methods* 70.1 (2014), pp. 12–19. DOI: 10.1016/j.ymeth.2014.01.022.

[96] E. Wulf et al. "Fluorescent phallotoxin, a tool for the visualization of cellular actin." In: *PNAS* 76.9 (1979), pp. 4498–4502. DOI: 10.1073/pnas.76.9.4498.

[97] Soon-Ok Cho and Susan M. Wick. "Actin in the developing stomatal complex of winter rye: A comparison of actin antibodies and Rh-phalloidin labeling of control and CB-treated tissues". In: *Cell Motil. Cytoskeleton* 19.1 (1991), pp. 25–36. DOI: 10.1002/cm.970190105.

[98] Brian M. Burkel, George von Dassow, and William M. Bement. "Versatile fluorescent probes for actin filaments based on the actin-binding domain of utrophin". In: *Cell Motil. Cytoskeleton* 64.11 (2007), pp. 822–832. DOI: 10.1002/cm.20226.

[99] Kiet Hua and Russell J. Ferland. "Fixation methods can differentially affect ciliary protein immunolabeling". In: *Cilia* 6.1 (2017). DOI: 10.1186/s13630-017-0045-9.

[100] Vera DesMarais et al. "Optimizing leading edge F-actin labeling using multiple actin probes, fixation methods and imaging modalities". In: *BioTechniques* 66.3 (2019), pp. 113–119. DOI: 10.2144/btn-2018-0112.

[101] W.F. Wolkers. "From anhydrobiosis to freeze-drying of mammalian cells". In: *Comp. Biochem. Physiol., Part A: Mol. Integr. Physiol.* 126 (2000), p. 159. DOI: 10.1016/s1095-6433(00)80315-3.

[102] Valeria Piazza et al. "Revealing the Structure of Stereociliary Actin by X-ray Nanoimaging". In: *ACS Nano* 8.12 (2014), pp. 12228–12237. DOI: 10.1021/nn5041526.

[103] H. B. Stuhrmann and A. Miller. "Small-angle scattering of biological structures". In: *J. Appl. Crystallogr.* 11.5 (1978), pp. 325–345. DOI: 10.1107/s0021889878013473.

[104] Keith P. Ryan. "Cryofixation of tissues for electron microscopy: a review of plunge cooling methods". In: *Scanning Microsc.* 6.3 (1992), pp. 715–743.

[105] L. A. Guildner, D. P. Johnson, and F. E. Jones. "Vapor Pressure of Water at Its Triple Point: Highly Accurate Value". In: *Science* 191.4233 (1976), pp. 1261–1261. DOI: 10.1126/science.191.4233.1261.

[106] Julia Sedlmair et al. "Imaging of Vascular Smooth Muscle Cells with Soft X-Ray Spectromicroscopy". In: *Microsc. Microanal.* 17.6 (2011), pp. 991–1001. DOI: 10.1017/s1431927611012165.

[107] Michael W. Toepke and David J. Beebe. "PDMS absorption of small molecules and consequences in microfluidic applications". In: *Lab Chip* 6.12 (2006), p. 1484. DOI: 10.1039/b612140c.

[108] Yun Seok Heo et al. "Characterization and Resolution of Evaporation-Mediated Osmolality Shifts That Constrain Microfluidic Cell Culture in Poly(dimethylsiloxane) Devices". In: *Anal. Chem.* 79.3 (2007), pp. 1126–1134. DOI: 10.1021/ac061990v.

[109] Rajendrani Mukhopadhyay. "When PDMS isn't the best". In: *Anal. Chem.* 79.9 (2007), pp. 3248–3253. DOI: 10.1021/ac071903e.

[110] Giulia Pacchioni. "An upgrade to a bright future". In: *Nat. Rev. Phys.* 1.2 (2019), pp. 100–101. DOI: 10.1038/s42254-019-0019-5.

[111] Chiara Cassini et al. "Large field-of-view scanning small-angle X-ray scattering of mammalian cells". In: *J. Synchrotron Radiat.* 27.4 (2020), pp. 1059–1068. DOI: 10.1107/s1600577520006864.

[112] E Fuchs and K Weber. "Intermediate Filaments: Structure, Dynamics, Function and Disease". In: *Annu. Rev. Biochem.* 63.1 (1994), pp. 345–382. DOI: 10.1146/annurev.bi.63.070194.002021.

[113] Zhenlin Li et al. "Cardiovascular Lesions and Skeletal Myopathy in Mice Lacking Desmin". In: *Dev. Biol.* 175.2 (1996), pp. 362–366. DOI: 10.1006/dbio.1996.0122.

[114] D J Milner et al. "Disruption of muscle architecture and myocardial degeneration in mice lacking desmin." In: *J. Cell Biol.* 134.5 (1996), pp. 1255–1270. DOI: 10.1083/jcb.134.5.1255.

[115] Maria Galou et al. “The importance of intermediate filaments in the adaptation of tissues to mechanical stress: Evidence from gene knockout studies”. In: *Biol. Cell* 89.2 (1997), pp. 85–97. DOI: 10.1111/j.1768-322x.1997.tb00997.x.

[116] Marinos C. Dalakas et al. “Desmin Myopathy, a Skeletal Myopathy with Cardiomyopathy Caused by Mutations in the Desmin Gene”. In: *N. Engl. J. Med.* 342.11 (2000), pp. 770–780. DOI: 10.1056/nejm200003163421104.

[117] D. Paulin and Z. Li. “Desmin: a major intermediate filament protein essential for the structural integrity and function of muscle”. In: *Exp. Cell Res.* 301.1 (2004), pp. 1–7. DOI: 10.1016/j.yexcr.2004.08.004.

[118] Harald Herrmann and Ueli Aebi. “Intermediate Filaments: Molecular Structure, Assembly Mechanism, and Integration Into Functionally Distinct Intracellular Scaffolds”. In: *Annu. Rev. Biochem.* 73.1 (2004), pp. 749–789. DOI: 10.1146/annurev.biochem.73.011303.073823.

[119] Harald Bär et al. “The biology of desmin filaments: how do mutations affect their structure, assembly, and organisation?” In: *J. Struct. Biol.* 148.2 (2004), pp. 137–152. DOI: 10.1016/j.jsb.2004.04.003.

[120] S. Kim and P. A. Coulombe. “Intermediate filament scaffolds fulfill mechanical, organizational, and signaling functions in the cytoplasm”. In: *Genes Dev.* 21.13 (2007), pp. 1581–1597. DOI: 10.1101/gad.1552107.

[121] John E. Eriksson et al. “Introducing intermediate filaments: from discovery to disease”. In: *J. Clin. Invest.* 119.7 (2009), pp. 1763–1771. DOI: 10.1172/jci38339.

[122] E. Fuchs. “A Structural Scaffolding of Intermediate Filaments in Health and Disease”. In: *Science* 279.5350 (1998), pp. 514–519. DOI: 10.1126/science.279.5350.514.

[123] Y Capetanaki. “Desmin Cytoskeleton A Potential Regulator of Muscle Mitochondrial Behavior and Function”. In: *Trends Cardiovasc. Med.* 12.8 (2002), pp. 339–348. DOI: 10.1016/s1050-1738(02)00184-6.

[124] Diana M. Toivola et al. “Cellular integrity plus: organelle-related and protein-targeting functions of intermediate filaments”. In: *Trends Cell Biol.* 15.11 (2005), pp. 608–617. DOI: 10.1016/j.tcb.2005.09.004.

[125] Christoph S. Clemen et al. “Desminopathies: pathology and mechanisms”. In: *Acta Neuropathol.* 125.1 (2013), pp. 47–75. DOI: 10.1007/s00401-012-1057-6.

[126] Elisabeth E. Charrier et al. “The desmin network is a determinant of the cytoplasmic stiffness of myoblasts”. In: *Biol. Cell* 110.4 (2018), pp. 77–90. DOI: 10.1111/boc.201700040.

[127] Kye-Yoon Park et al. “Sporadic cardiac and skeletal myopathy caused by a de novo desmin mutation”. In: *Clin. Genet.* 57.6 (2000), pp. 423–429. DOI: 10.1034/j.1399-0004.2000.570604.x.

[128] Ayush Dagvadorj et al. “A series of West European patients with severe cardiac and skeletal myopathy associated with a de novo R406W mutation in desmin”. In: *J. Neurol.* 251.2 (2004), pp. 143–149. DOI: 10.1007/s00415-004-0289-3.

[129] Harald Bär et al. “Pathogenic effects of a novel heterozygous R350P desmin mutation on the assembly of desmin intermediate filaments in vivo and in vitro”. In: *Hum. Mol. Genet.* 14.10 (2005), pp. 1251–1260. DOI: 10.1093/hmg/ddi136.

[130] Harald Bär et al. "Forced expression of desmin and desmin mutants in cultured cells: Impact of myopathic missense mutations in the central coiled-coil domain on network formation". In: *Exp. Cell Res.* 312.9 (2006), pp. 1554–1565. DOI: 10.1016/j.yexcr.2006.01.021.

[131] Piotr Pruszczyk et al. "Restrictive cardiomyopathy with atrioventricular conduction block resulting from a desmin mutation". In: *Int. J. Cardiol.* 117.2 (2007), pp. 244–253. DOI: 10.1016/j.ijcard.2006.05.019.

[132] KY van Spaendonck-Zwarts et al. "Desmin-related myopathy". In: *Clin. Genet.* 80.4 (2011), pp. 354–366. DOI: 10.1111/j.1399-0004.2010.01512.x.

[133] Pierre Joanne et al. "Viral-mediated expression of desmin mutants to create mouse models of myofibrillar myopathy". In: *Skeletal Muscle* 3.1 (2013), p. 4. DOI: 10.1186/2044-5040-3-4.

[134] Christoph S. Clemen et al. "The toxic effect of R350P mutant desmin in striated muscle of man and mouse". In: *Acta Neuropathol.* 129.2 (2015), pp. 297–315. DOI: 10.1007/s00401-014-1363-2.

[135] Bastian Bechtold. "Violin Plots for Matlab". In: *GitHub repository. URL https://github.com/bastibe/Matlab* (2016).

[136] Jerry L. Hintze and Ray D. Nelson. "Violin Plots: A Box Plot-Density Trace Synergism". In: *Am. Stat.* 52.2 (1998), p. 181. DOI: 10.2307/2685478.

[137] John W Tukey et al. *Exploratory data analysis*. Vol. 2. Reading, Mass., 1977.

[138] D. A. Darling. "The Kolmogorov-Smirnov, Cramer-von Mises Tests". In: *Ann. Math. Stat.* 28.4 (1957), pp. 823–838. DOI: 10.1214/aoms/1177706788.

[139] E.C. Anderson, D.F. Petersen, and R.A. Tobey. "Density Invariance of Cultured Chinese Hamster Cells with Stage of the Mitotic Cycle". In: *Biophys. J.* 10.7 (1970), pp. 630–645. DOI: 10.1016/s0006-3495(70)86325-1.

[140] Robert F. Brooks and Robert Shields. "Cell growth, cell division and cell size homeostasis in Swiss 3T3 cells". In: *Exp. Cell Res.* 156.1 (1985), pp. 1–6. DOI: 10.1016/0014-4827(85)90255-1.

[141] Paul Jorgensen and Mike Tyers. "How Cells Coordinate Growth and Division". In: *Curr. Biol.* 14.23 (2004), R1014–R1027. DOI: 10.1016/j.cub.2004.11.027.

[142] Berend Snijder and Lucas Pelkmans. "Origins of regulated cell-to-cell variability". In: *Nat. Rev. Mol. Cell Biol.* 12.2 (2011), pp. 119–125. DOI: 10.1038/nrm3044.

[143] Y. Sung et al. "Size homeostasis in adherent cells studied by synthetic phase microscopy". In: *PNAS* 110.41 (2013), pp. 16687–16692. DOI: 10.1073/pnas.1315290110.

[144] Peter Fratzl et al. "Nucleation and growth of mineral crystals in bone studied by small-angle X-ray scattering". In: *Calcif. Tissue Int.* 48.6 (1991), pp. 407–413. DOI: 10.1007/bf02556454.

[145] Christian Burger et al. "Lateral Packing of Mineral Crystals in Bone Collagen Fibrils". In: *Biophys. J.* 95.4 (2008), pp. 1985–1992. DOI: 10.1529/biophysj.107.128355.

[146] Saswati Pujari et al. "X-ray scattering measurements of particle orientation in a sheared polymer/clay dispersion". In: *Rheol. Acta* 50.1 (2011), pp. 3–16. DOI: 10.1007/s00397-010-0492-3.

[147] B. J Lemaire et al. "The measurement by SAXS of the nematic order parameter of laponite gels". In: *Europhys. Lett. (EPL)* 59.1 (2002), pp. 55–61. DOI: 10.1209/epl/i2002-00159-8.

[148] F. Camerel et al. “Combined SAXS-Rheological Studies of Liquid-Crystalline Colloidal Dispersions of Mineral Particles”. In: *Langmuir* 19.24 (2003), pp. 10028–10035. DOI: 10.1021/la034626p.

[149] Karl Pearson. “LIII. On lines and planes of closest fit to systems of points in space”. In: *Philos. Mag.* 2.11 (1901), pp. 559–572. DOI: 10.1080/14786440109462720.

[150] Philipp Berens. “CircStat: AMATLABToolbox for Circular Statistics”. In: *J. Stat. Softw.* 31.10 (2009). DOI: 10.18637/jss.v031.i10.

[151] J. T. Koberstein, B. Morra, and R. S. Stein. “The Determination of Diffuse-Boundary Thicknesses of Polymers by Small-Angle X-Ray Scattering”. In: *J. Appl. Crystallogr.* 13.1 (1980), pp. 34–45. DOI: 10.1107/s0021889880011478.

[152] European Synchrotron Radiation Facility (ESRF). *EBS – Extremely Brilliant Source*. 2019. URL: https://www.esrf.eu/home/UsersAndScience/Accelerators/ebs---extremely-brilliant-source.html (visited on 02/18/2021).

[153] *SPEC – Software for Diffraction*. URL: https://certif.com/spec.html (visited on 02/18/2021).

[154] *BLISS*. URL: https://bliss.gitlab-pages.esrf.fr/bliss/master/ (visited on 02/18/2021).

[155] Emilie Leccia et al. “Hard Alpha-Keratin Degradation Inside a Tissue Under High Flux X-Ray Synchrotron Micro-Beam: A Multi-Scale Time-Resolved Study”. In: *J. Struct. Biol.* 170.1 (2010), pp. 69–75. DOI: 10.1016/j.jsb.2009.11.006.

[156] Ewelina Kosior et al. “Study of Radiation Effects on the Cell Structure and Evaluation of the Dose Delivered by X-Ray and α-Particles Microscopy”. In: *Appl. Phys. Lett.* 101.26 (2012), p. 263102. DOI: 10.1063/1.4773181.

[157] A. Gianoncelli et al. “Soft X-Ray Microscopy Radiation Damage on Fixed Cells Investigated With Synchrotron Radiation FTIR Microscopy”. In: *Sci. Rep.* 5.1 (2015). DOI: 10.1038/srep10250.

[158] Clément Y. J. Hémonnot and Sarah Köster. “Imaging of Biological Materials and Cells by X-Ray Scattering and Diffraction”. In: *ACS Nano* 11.9 (2017), pp. 8542–8559. DOI: 10.1021/acsnano.7b03447.

[159] Jennifer L. Gregg et al. “Measurement of the thickness and volume of adherent cells using transmission-through-dye microscopy”. In: *Pfluegers Arch.* 460.6 (2010), pp. 1097–1104. DOI: 10.1007/s00424-010-0869-2.

[160] Céline Bottier et al. “Dynamic measurement of the height and volume of migrating cells by a novel fluorescence microscopy technique”. In: *Lab Chip* 11.22 (2011), p. 3855. DOI: 10.1039/c1lc20807a.

Acknowledgements

The list of people who helped me during my time as a Ph. D. student is so long (and the hour at which I am writing is so late), that I am bound to forget someone, and for that I am very sorry. However, it would be impossible for me to forget to thank Prof. Dr. Sarah Köster, who supervised this work and helped me grow as a researcher. Moreover, she gave me the opportunity to work on a very interesting project and to meet the wonderful people in the group. Thank you, Sarah. I would also like to thank the other two members of my thesis committee, Prof. Dr. Alexander Egner and Prof. Dr. Tim Salditt, for the stimulating scientific discussions and invariable kindness during meetings. Double thanks go to Tim for also reviewing this thesis. My gratitude also goes to Prof. Dr. Jochen Hub, for being a member of my thesis committee at the beginning of my Ph. D. Many thanks to Prof. Dr. Timo Betz, Prof. Dr. Stefan Klumpp and Prof. Dr. Simone Techert for joining the examination board. I am extremely thankful to Manfred Burghammer for the excellent support and fruitful discussions during beamtimes and for the ever-interesting conversation during breaks. The vast majority of this work wouldn't have been possible without the samples provided by Prof. Dr. Harald Herrmann and his collaborators Dr. Dorothea Schultheis and Lisa Kamm, to whom I am also grateful for all of the useful information on cell culture and immunostaining. I cannot mention cell culture without thanking Dr. Ulrike Rölleke, Susanne Bauch and Susanne Hengst for all of their help in the lab, and Susanne B. in particular for putting up with the Italian office and for all the great walks. I would also like to thank Jochen Herbst, Peter Luley and Peter Nieschalk for their technical help with sample preparation and wet sample chamber design. Thanks to Jan Goeman for the IT support and to Dr. Markus Osterhoff for the invaluable help with data analysis, and to both for everything data-related during beamtimes, especially in these COVID-19 plagued days. A big thank you to Christine Wilke-Feist, Eva Hetzel, Kerstin Pluschke, Michaela Ständer and Sabine Balder for making my life way easier with their administrative help. Many thanks to Dr. Jan-David Nicolas for the useful discussions about data analysis in general and the Nanodiffraction toolbox in particular, and to all of the fantastic people of the Salditt group. Thanks for being the highlight of DESY users' meetings and for enduring my (allegedly drunken) broken German.

There are no words, or rather, there would be too many words to thank the members of the Köster group, present and past. You have been family more than colleagues to me. Thanks to Viktor, because that's where I started; thanks to Jana for the chocolate making and to Johanna for her assistance with German. Thanks to Aishwaryia for the frienship and cheerfulness and to Charlotte for the beamtime company and tea-brewing (the thanks for scientific support go without saying). Thanks to Manuela for her daily motivational messages and for all of the time together and apart. Thanks to Gerrit for the useful information in every field and for the limitless will to help. Thanks to Magdalena for the help in the cleanroom, to Kim for the help with AutoCAD, to Ruth for the help with the spin coater and to all for the fun free time. Thanks to Jan-Philipp for the coding, the whiteboard cleaning and the occasional, unexpected song outbursts. Thanks to Baby Titz for the Czech phrases, the Czech food and wisdom, for all of the shopping and for not resenting her nicknames. Thanks to Mama Julia for all of the food, Harry Potter and Sing Star. Thanks to Lotta for her literally uplifting hugs. Thanks

to Anna B. for the walks and the chats, and to Anna S. for the chats and the walks and for being my cartoonist of choice. Thanks to Heidi for the sweetness and the crazy and that time at the Sportzentrum destroying our self-esteem with artistic gymnastics. And for all of the crunchy leaves. Thanks to Andrew for all of the scientific and not-scientific help. Without you, I wouldn't have a published paper. Or a wardrobe. A thousand grazie to my Italian partner in crime Eleonora. Whatever would I have done without you keeping my home-sickness down?

Special thanks to my siblings from different parents, Sofia and Nicola: I live for your songs and panda gifs. Loving thanks to my blood sister Lisa, who speaks for four during our family Skype calls, and to Brunella and Fabio, who have to limit their news to the short time before Lisa joins the call. A huge huge thank you to Stefano, who kept me on track and kept me company from afar. For once, saying that I could never have made it without you isn't too much of a figure of speech.

List of publications

- Andrew Wittmeier, Chiara Cassini, Mareike Töpperwien, Manuela Denz, Johanned Hagemann, Markus Osterhoff, Tim Salditt and Sarah Köster, "Combined scanning small-angle X-ray scattering and holography probes multiple length scales in cell nuclei". In: *J. Synchrotron Radiat.* 28.2 (2021). DOI: 10.1107/S1600577520016276.

- Anna Zelená, Sebastian Isbaner, Daja Ruhlandt, Anna Chizhik, Chiara Cassini, Andrey S. Klymchenko, Jörg Enderlein, Alexey Chizhik and Sarah Köster, "Time-resolved MIET measurements of blood platelet spreading and adhesion". In: *Nanoscale* 12.41 (2020), pp. 21306–21315. DOI: 10.1039/D0NR05611A.

- Chiara Cassini, Andrew Wittmeier, Gerrit Brehm, Manuela Denz, Manfred Burghammer and Sarah Köster, "Large field-of-view scanning small-angle X-ray scattering of mammalian cells". In: *J. Synchrotron Ratiat.* 27.4 (2020). DOI: 10.1107/S1600577520006864.

- Manuela Denz, Gerrit Brehm, Clément Y. J. Hémonnot, Heidi Spears, Andrew Wittmeier, Chiara Cassini, Oliva Saldanha, Eleonora Perego, Ana Diaz, Manfred Burghammer and Sarah Köster, "Cyclic olefin copolymer as an X-ray compatible material for microfluidic devices". In: *Lab Chip* 18.1 (2018), pp. 171–178. DOI: 10.1039/C7LC00824D.

- Francesco Zonta, Damiano Buratto, Chiara Cassini, Mario Bortolozzi and Fabio Mammano, "Molecular dynamics simulations highlight structural and functional alterations in deafness-related M34T mutation of connexin 26". In: *Front. Physiol.* 5 (2014), p. 85. DOI: 10.3389/fphys.2014.00085.